ABSTRACT

Title of dissertation: Integrated Propulsion and Power Modeling for Bimodal Nuclear Thermal Rockets

Joshua Clough
Doctor of Philosophy, 2007

Dissertation directed by: Professor Mark Lewis
Department of Aerospace Engineering

Bimodal nuclear thermal rocket (BNTR) engines have been shown to reduce the weight of space vehicles to the Moon, Mars, and beyond by utilizing a common reactor for propulsion and power generation. These savings lead to reduced launch vehicle costs and/or increased mission safety and capability. Experimental work of the Rover/NERVA program demonstrated the feasibility of NTR systems for trajectories to Mars. Numerous recent studies have demonstrated the economic and performance benefits of BNTR operation.

Relatively little, however, is known about the reactor-level operation of a BNTR engine. The objective of this dissertation is to develop a numerical BNTR engine model in order to study the feasibility and component-level impact of utilizing a NERVA-derived reactor as a heat source for both propulsion and power.

The primary contribution is to provide the first-of-its-kind model and analysis of a NERVA-derived BNTR engine.

Numerical component models have been modified and created for the NERVA reactor fuel elements and tie tubes, including 1-D coolant thermodynamics and radial thermal conduction with heat generation. A BNTR engine system model has been created in order to design and analyze an engine employing an expander-cycle nuclear rocket and Brayton cycle power generator using the same reactor.

Design point results show that a 316 MWt reactor produces a thrust and specific impulse of 66.6 kN and 917 s, respectively. The same reactor can be run at 73.8 kWt to produce the necessary 16.7 kW electric power with a Brayton cycle generator. This demonstrates the feasibility of BNTR operation with a NERVA-derived reactor but also indicates that the reactor control system must be able to operate with precision across a wide power range, and that the transient analysis of reactor decay heat merits future investigation.

Results also identify a significant reactor pressure-drop limitation during propulsion and power-generation operation that is caused by poor tie tube thermal conductivity. This leads to the conclusion that, while BNTR operation is possible with a NERVA-derived reactor, doing so requires careful consideration of the Brayton cycle design point and fuel element survivability.

INTEGRATED PROPULSION AND POWER MODELING FOR BIMODAL NUCLEAR THERMAL ROCKETS

by

Joshua Clough

Dissertation submitted to the Faculty of the Graduate School of the
University of Maryland, College Park in partial fulfillment
of the requirements for the degree of
Doctor of Philosophy
2007

Advisory Committee:
Professor Mark Lewis, Chair/Advisor
Professor David Akin
Professor Christopher Cadou
Professor Gary Pertmer
Professor Kenneth Yu

DEDICATION

To my wife, Ann.

ACKNOWLEDGEMENTS

This work is supported by the Space Vehicles Technology Institute, one of the NASA Constellation University Institute Programs, under grant NCC3-989, with joint sponsorship from the Department of Defense. Appreciation is expressed to Claudia Meyer of NASA Glenn Research Center, program manager of the University Institute activity, and to Drs. John Schmisseur and Walter Jones of the Air Force Office of Scientific Research.

I was fortunate enough to be able to collaborate with many people from NASA Glenn Research Center and would like to thank them for their contributions — Stan Borowski, Bruce Schnitzler, and Mark Stewart for vehicle and reactor references, data, and general feedback. Paul Johnson for assistance with CCSS and cycle convergence. Jim Fittje for the original NTR model. Most importantly, thank you to Tom Lavelle for NPSS support and his total dedication to this project.

Thank you to everyone at the University of Maryland who made this project possible. My advisor, Mark Lewis, for his guidance and support over the last five years. Ryan Starkey, for his advice, immense help with editing, and just letting me pester him with questions. The entire dissertation committee for their recommendations and support. And finally thank you to my officemates for their support and friendship.

Finally, on a more personal note, I would like to thank my wife Ann, who has been my sounding board, editor, cook, therapist, and has kept grounded for the past several years. I couldn't have reached this point without her.

TABLE OF CONTENTS

LIST OF TABLES

LIST OF FIGURES

LIST OF SYMBOLS

A	area, m^2
AR	area ratio
a	speed of sound, m/s
C_f	coefficient of friction
C_p	specific heat at constant pressure, J/kg-K
D	diameter, m
D_h	hydraulic diameter, m
dx	axial segment spacing, m
e_R	recuperator effectiveness
f	coefficient of friction
g	gravitational constant, 9.81 m/s^2
$\dot{g}$	volumetric heat generation, W/m^3
h	enthalpy, J/kg
h_p	pump head, m
I_{sp}	specific impulse, s
k	thermal conductivity, W/m-K
L	length, m
M	mach number
MW	molecular mass, g/mol
m	mass, kg
$\dot{m}$	mass flow rate, kg/s
N_{shaft}	shaft speed, rpm
Nu	Nusselt number
P	electric or nuclear power, W
Pr	Prandtl number
p	pressure, Pa
$\dot{Q}$	heat transfer rate, W
R_u	universal ideal gas constant, 8.314 J/mol-K
Re	Reynolds number
r	radius, m
S	fuel element pitch, m
T	thrust, N
T_x	temperature at location 'x', K
u	velocity, m/s
V	volume, m^3
$\dot{V}$	volumetric flow rate, m^3/s
w	weight, N
$\dot{W}$	work or shaft power, W

β	bypass ratio
γ	specific heat ratio
ΔV	orbital velocity change, m/s
ϵ	emissivity
η	efficiency
π	compression ratio
ρ	density, kg/m^3
σ	Stefan-Boltzmann constant, 5.67e-8 Js^{-1}m^{-2}K^{-4}
τ	torque, N-m
τ_w	wall shear stress, Pa
Ω	maximum-to-average power factor

Subscripts

a	atmospheric
b	burner
c	compressor, reactor channel
cav	cavity
e	nozzle exit
f	fuel
o	chamber
p	pump
pri	primary
s	isentropic
sec	secondary
sys	system
t	turbine
th	nozzle throat
w	wall
x	Brayton cycle recuperator cold leg exit
1	Brayton cycle compressor inlet
2	Brayton cycle compressor exit
3	Brayton cycle turbine inlet
4	Brayton cycle turbine exit
5	Brayton cycle recuperator hot leg exit

Chapter 1

Introduction

In early 2004, NASA announced its Vision for Space Exploration (VSE), which pledged to return Humans to the Moon by 2020 and then proceed with manned exploration of "Mars and other destinations." The development of power and propulsion systems is cited as a key aspect of the Mars exploration portion of the Vision. Specifically, the VSE lists nuclear propulsion and power research as "key to enabling other advanced robotic missions and human missions beyond Earth's orbit" [1]. In June 2004, the Aldridge Commission similarly identified nuclear propulsion and power as an enabling technology for space exploration [2].

Nuclear thermal propulsion is ideal for manned Mars missions because it can provide twice the fuel efficiency of chemical propulsion [3], which leads to lighter, less expensive vehicles, and faster, safer missions. A spacecraft power system that utilizes the same nuclear reactor as the propulsion system would be able to provide consistent electric power regardless of distance from the Sun, and could weigh less than a separate, independent power system. It is for these reasons that a bimodal nuclear thermal rocket (BNTR) system, one which uses a common reactor for propulsion and power generation, is the current reference engine for the manned exploration of Mars [4]–[7].

1.1 Nuclear Thermal Propulsion

1.1.1 Motivation

Currently proposed Mars missions based on chemical propulsion suffer from two major limitations: 1) the vehicles are heavy, requiring a high mass in low Earth orbit (LEO), and correspondingly high launch costs; 2) the crew must face health risks from prolonged exposure to zero-gravity and ambient radiation. The initial mass in LEO (IMLEO) for a fleet consisting of two or three cargo vehicles and one manned vehicle for a chemically propelled Mars mission ranges from about 600 to over 3000 metric tons, depending on the launch date, trajectory, and mission profile [8]–[11]. Donahue and Cupples calculate an IMLEO of 668 mt, which would require eight Earth-to-orbit launches on an 80 mt launch vehicle [10]. Most recent manned Mars missions assume opposition class (short-stay) trajectories that require one-way flight times of six to ten months [12], and the health effects of such a trip are not fully understood.

The risk of exposure can be reduced through a combination of selecting more aggressive trajectories with shorter travel times, adding artificial gravity capability, and adding more robust shielding. From the rocket equation, all of these improvements can be facilitated by increasing the specific impulse (I_{sp}) of the propulsion system. Equation 1.1 shows the well-known rocket equations, which states that orbital velocity change (ΔV) is proportional to the specific impulse of the propulsion

system and the natural log of the mass ratio of the vehicle.

$$\Delta V = g I_{sp} \ln \left(\frac{m_{initial}}{m_{final}} \right) \tag{1.1}$$

Specific impulse is defined as thrust divided by weight flow rate of propellant, and essentially represents the fuel efficiency of the system.

$$I_{sp} = \frac{T}{g\dot{m}_e} \tag{1.2}$$

Mass ratio, in turn, is defined as the ratio of the vehicle mass at the beginning to end of a launch or maneuver. For a single stage vehicle, the mass ratio simply accounts for the propellant expenditure.

Faster trajectories require a higher orbital velocity (ΔV), which Eq. 1.1 shows is a function of specific impulse and the vehicle mass ratio. So, for a given mass ratio, (ΔV) can only be increased by using a propulsion system with a higher specific impulse. Adding shielding or artificial gravity systems would increase the vehicle mass, which (for a given trajectory) would also require a higher specific impulse. Finally, a vehicle with approximately the same dry mass (m_{final}) and trajectory, but higher specific impulse would have a lower initial mass, thus reducing total launch costs to LEO. Thus, the rocket equation shows that improvements in I_{sp} can benefit all aspects of vehicle and mission design.

There are many energy sources in nature that can be used to provide propulsion with a higher specific impulse than chemical rockets. Solid, molten, or gaseous-core nuclear reactors can heat a propellant as it passes through. Atomic fission, fusion, or antimatter annihilation could even be harnessed directly for high-energy exhaust. With the increasing energy content of each of these systems, the propellant exit

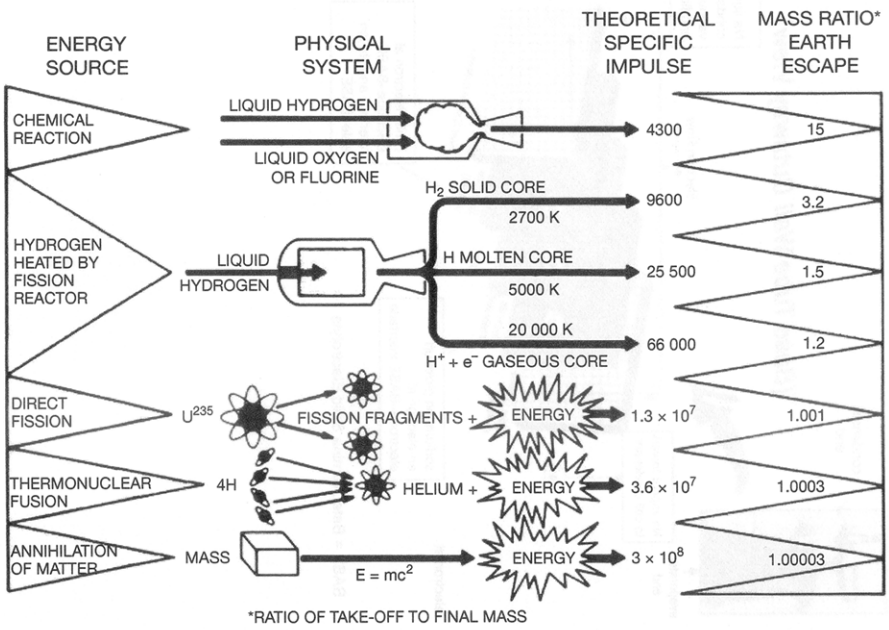

Figure 1.1: A summary of several propulsion energy sources and corresponding performance [3]. Specific impulse is given here in m/s ($I_{sp}(m/s) = 9.8I_{sp}(s)$).

velocity, and thus specific impulse, increases. Figure 1.1 shows a comparison of these systems.

Although solid-core nuclear thermal rocket (NTR) propulsion is not the most efficient system possible, it provides an excellent combination of high specific impulse and technical maturity. There has been an extensive amount of NTR research and development, dating back to the Rover/NERVA ("Nuclear Engine for Rocket Vehicle Applications") program, which operated from 1955-1973 and brought about major advancements in composite fuel technology, solid-core reactor design, and demonstrated the feasibility of NTR engines for Mars missions. In fact, this program ended just short of the development of a flight-ready engine, and NERVA reactors and engines remain the basis of the modern NTR vehicle design [13].

Another important different between NTR and chemical rockets is that the

NTR engines discussed in this dissertation are intended solely for in-space propulsion. Chemical propulsion will still be required to launch the NTR-propelled transfer vehicle (or portions thereof) into orbit. While some may debate the benefits and consequences of using NTR engines in the atmosphere, that is a predominantly sociopolitical discussion, and far beyond the scope of the work presented here.

Returning to Eq. 1.1, an NTR following the same trajectory as chemical rocket will have a lower mass ratio, requiring less fuel. For the same mission as the chemical data cite previously, Donahue and Cupples concluded that a NTR-powered mission would require a total IMLEO of 419 mt and only 6 Earth-to-orbit launches [10]. These mass savings can be used to reduce launch costs, add more robust vehicle systems, or some combination of the two. Recent NTR concepts have proposed following the same Earth-to-Mars trajectory as chemical rockets, but include larger crew habitats with additional radiation shielding, extra propellant for artificial gravity operation, and still require fewer launches to LEO [4]–[7].

1.1.2 Operation

Nuclear thermal rockets use a stationary reactor containing solid, radioactive fuel elements to heat a non-reacting propellant that flows through it. This propellant also acts as a coolant for the hot reactor core and other engine components. This process is in contrast to a chemical rocket, in which reacting fuel and oxidizer serve as both heat source and propellant. As the NTR propellant is non-reacting, any gas may be chosen. The low molecular weight and good cooling properties of hydrogen

Table 1.1: Theoretical Rocket Performance

System	Energy Source	I_{sp}, max. (s)	I_{sp}, $\eta = 80\%$ (s)
HC-fueled chemical	46 MJ/kg chemical energy	463	414
H2-fueled chemical	117 MJ/kg chemical energy	520	465
NTR	2560 K chamber temperature	975	872

make it the propellant of choice for NTR engines.

The molecular weight benefit of hydrogen propellant is best illustrated by examining specific impulse of an ideal rocket, written in terms of the chamber temperature (T_o) and exhaust gas properties.

$$I_{sp} = \frac{1}{g}\sqrt{\frac{2\gamma R_u T_o}{(\gamma - 1)MW}} \tag{1.3}$$

Equation (1.3) is derived from the conservation of energy across an ideal nozzle, where the propellant expands isentropically to atmospheric pressure. For given chamber temperature, specific impulse is inversely proportional to the square root of molecular weight of the engine exhaust. For a hydrogen-oxygen fueled engine, this is water vapor (MW=18 amu). For a NTR, the exhaust is pure hydrogen gas (MW=2 amu). Theoretically, NTR engines can provide a factor of three improvement in specific impulse over chemical rockets. In practice, the benefit is closer to a factor of two, as shown in Table 1.1, which compares the ideal theoretical performance of chemical and NTR engines based on 100% and 80% conversion efficiency. For the chemical rockets, this is calculated assuming direct conversion of combustion energy to kinetic, while the NTR calculation assumes direct conversion of thermal energy to kinetic, as shown in Eq. 1.3.

The reason that NTR engines can only realistically produce a twofold benefit in specific impulse is largely due to the material temperature limit of the reactor fuel, which is lower than the combustion temperature of a chemical rocket. The chamber of a NTR is immediately downstream of the reactor exit, so the aft end of the solid reactor fuel elements will be exposed to the high chamber temperatures. In order to prevent melting, deforming, or otherwise limiting the lifespan of the fuel elements, the chamber temperature of a solid-fuel NTR will be constrained by the material limits of the fuel.

The use of hydrogen propellant with a stationary reactor also enables novel configurations that add to the utility of an NTR engine. One concept, generally called "oxygen-afterburning" or "LOX-augmented" NTR (LANTR) blends nuclear and chemical rocket technology by injecting and burning oxygen in the reactor exhaust, trading some specific impulse for an increase in thrust by increasing the temperature and mass flow of the exhaust. Another novel concept of recent interest uses the nuclear reactor to produce thrust and electric power for the spacecraft. Both concepts have been studied extensively; the former has been developed extensively by the Aerojet Corporation [14]– [18], but due the weight penalty and combustion losses incurred in such a system, it is not examined here. The latter, known as "bimodal" operation, is currently of great interest to NASA and is the focus of the remainder of this dissertation.

1.2 Bimodal Nuclear Thermal Rockets

During the course of a typical NTR-powered mission to Mars, thrust is only generated for approximately one hour. For the remainder of the mission, the reactor is idle, continually producing radioactive decay heat that must be exhausted from the system. Bimodal nuclear thermal rocket (BNTR) systems take advantage of the nuclear reactor throughout the entire mission by operating it in two separate modes: a high-power propulsion mode and a secondary, low-power, power generation mode. Such a system can reduce vehicle weight by removing the need for multiple reactors, radioisotope power generation (RPG) units, or solar arrays.

A BNTR power system uses the propulsion reactor as a heat source, and connects it to a separate closed-loop power cycle. This closed loop will generally use an inert gas working fluid in stead of hydrogen, in order to prevent corrosion of the reactor. Many past and present studies base the BNTR reactor on the material and geometry of the NERVA program in order to leverage the extensive research and development that has already been completed [19]– [22]. In such a system, the power cycle coolant only passes through reactor support elements called "tie tubes." The remaining reactor fuel elements are cooled by thermal conduction to adjacent tie tubes. This process and configuration will be described in detail in Chapter 3.

The primary objective of a BNTR power system is to provide electric power at the highest conversion efficiency possible, while also providing sufficient reactor cooling. This leads to a trade-off between pressure loss and heat transfer within the tie tube elements. The efficiency of a closed loop power cycle will, in general,

decrease with increasing pressure loss. The available input heat and reactor cooling increase with the rate of heat transfer. The goals of high heat transfer and low pressure drop must be examined together because optimizing for one tends to minimize the other. For example, heat transfer can be improved by increasing flow rate. Doing so, however, also increases the pressure loss. As such, the trade-off between heat transfer and pressure loss will drive the power system design and analysis.

1.3 Project Overview

1.3.1 Motivation

Many studies have cited the theoretical benefits of BNTR operation in vehicle and mission design [4]–[27], but have done so assuming two levels of reactor performance without any examination of the trade-off between heat transfer and pressure loss, or verification of whether bimodal operation is possible. Despite the wealth of information available on BNTR missions, vehicles, and engines, little information is available regarding the reactor- and component-level operation of a BNTR engine. Many questions remain unanswered regarding the feasibility of BNTR operation. Can a reactor designed for high power and high mass flow during propulsion mode operate at multiple orders-of-magnitude less power with an acceptable pressure loss? Can the power cycle provide sufficient cooling of the reactor fuel elements when the coolant/propellant is no longer flowing? Are there any special design or operation considerations for using a large reactor with a relatively small power system? What

happens during transition from propulsion to power-generation modes?

The above questions must be answered before BNTR vehicles can be developed. An inexpensive means to address these questions is through computational modeling. Computer models can help verify the feasibility of such designs without investing large amounts of money into hardware development. This, however, requires more sophisticated reactor and engine models than those currently available.

1.3.2 Objective

The objective of this project is to develop a numerical BNTR engine model in order to study the feasibility and component-level impact of utilizing a NERVA-derived reactor as a heat source for both power and propulsion in a single integrated engine system. This model is used analyze the steady-state performance during both propulsion and power-generation modes, ultimately addressing the first three questions posed above. While other materials and geometries exist, this model and research specifically focuses on a NERVA reactor because it is the most technically mature and there is a wealth of supporting data and studies available. The transient analysis of a BNTR is also a concern, but is of secondary importance until the steady-state operation of a BNTR can be proved. As such, the analysis of mode transition is beyond of the scope of this research.

In addition to producing a BNTR system model, this project will also use the model to explore the BNTR engine design space. Multiple NTR and BNTR design points will be examined and trade studies into the sensitivity of engine performance

to material technology, reactor size, and design point selection will be performed.

1.3.3 Approach

The basic approach of this dissertation research is to create a multi-mode BNTR system model through the synthesis of pre-existing codes and models that provide some of the required capability. One-dimensional reactor flow models have been created as needed to accurately calculate the pressure loss and heat transfer during propulsion and power generation operation.

The modeling is being performed with NASA's Numerical Propulsion System Simulation (NPSS) code. NPSS is an industry-standard modular propulsion modeling program with a built-in solver and thermodynamic library, allowing great flexibility in creating balanced models of advanced propulsion systems. The modular nature of NPSS also means that the models created here can be run on any computer already running NPSS, allowing NASA (or any other interested party) to run the BNTR model with no additional installation or modification required.

The pre-existing models that are being used are NASA's Nuclear Engine System Simulation (NESS) and Closed Cycle System Simulation (CCSS). NESS is the standard NTR modeling code at NASA Glenn, contains 1-D fuel element coolant flow calculations, but lacks the flexibility to perform the tie tube flow analysis required for BNTR operation. CCSS is a NPSS-based simulation of a closed Brayton cycle power generation system. It is intended to model a reactor-heated space power system, but does not contain a reactor component model.

The final BNTR model has been created by adding a tie tube component model with 1-D coolant flow and radial thermal conduction calculations to a pre-existing, NESS-based NTR model in NPSS. The same tie tube model is also substituted into CCSS as the new reactor component model. A high-level BNTR driver routine has also been created in NPSS, automating the process of mode switching and propulsion and power system design.

1.3.4 Primary Contribution

The primary contribution of this dissertation is a first-of-its-kind model and analysis of a NERVA-derived tie tube component, reactor system, and BNTR engine. This study is the first to actually model the component-level operation of a NERVA-derived reactor operating in both propulsion and power-generation modes. The NPSS-based BNTR model is also being provided to NASA in order to add capability and fidelity to their spacecraft architecture studies.

The use of this model also contributes a first-of-its-kind examination of a NERVA-derived BNTR system. Several design point studies, including baseline values corresponding to current reference designs, highlight important consequences of BNTR operation that lead to recommendations for the development of future BNTR propulsion systems.

Chapter 2

Previous Work

Research into nuclear propulsion and power for space began over 60 years ago, leading to the experimental development of nuclear reactors and power systems concurrent with the Apollo program. Development has continued through the Space Exploration Initiative of the early 1990's to today's Vision for Space Exploration. There is a wealth of research that has been performed over the past five decades, and it would be impractical to present it all here. This chapter will instead provide a summary of the history as well as key studies and findings that apply to the research at hand. Although much of this work overlaps chronologically and programmatically, for the sake of simplicity this chapter is divided into the following sections: 1) nuclear propulsion, 2) bimodal nuclear propulsion and power, and 3) nuclear power for space, specifically focusing on nuclear-heated Brayton cycle power systems.

2.1 Nuclear Propulsion

Nuclear thermal rockets have been studied extensively over the past 60 years. Experimental programs, such as Rover/NERVA (Nuclear Engine for Rocket Vehicle Applications) have demonstrated the feasibility of these systems for use in missions

to Mars [13]. Research surrounding the Space Exploration Initiative reiterated these benefits and lead to more advanced research into NERVA-based vehicles. Modern concepts, such as oxygen afterburning and bimodal operation, build on these fundamentals with technological improvements that enable lighter, less expensive vehicles and missions.

2.1.1 Early Development: 1945-1955

The use of nuclear energy for spacecraft propulsion was proposed as early as 1945 by von Karmon, who suggested the idea to the USAF Scientific Advisory Board (SAB). Having no direct need for the engines, and citing a lack of available materials, the SAB did not follow through with von Karmon's suggestion [13]. The following year, at the end of the Manhattan Project, several fundamental investigations into NTR propulsion began simultaneously around the country. A literature review by Bussard [28] contains the only publicly available discussion of these projects.

Beginning in 1946, many groups and individuals from Douglas Aircraft, the Johns Hopkins University Applied Physics Lab. (APL), Northrop Aircraft (through the Nuclear Energy for the Propulsion of Aircraft (NEPA) program), and North American Aviation all examined the possibility of building a ballistic missile powered by nuclear energy. The majority of these studies came to the conclusion that a cylindrical, graphite and uranium-based, solid fuel reactor heating hydrogen propellant would be the most practical NTR design. They also concluded that a lack of understanding of the reactor fuel, specifically its strength and durability, was the

greatest limiting factor on the construction of the engines [28].

The result of the preliminary studies was the formation of a SAB Nuclear Missiles Subcommittee. Subcommittee meetings with both industry and government laboratory representatives in October 1954 and March 1955 eventually lead the creation of Project Rover in late 1955 [13, 28].

2.1.2 Rover/NERVA-era: 1955-1973

Large scale, government sponsored NTR research and development began with the Rover/NERVA program. This program operated from 1955-1973 and remains the basis of modern NTR reactor design. There are many references in the open literature that cover the history and details of this program. Koenig has written the foremost technical review of the Rover/NERVA program [13]. Dewar recently published the definitive political and programmatic history [29]. Excellent overviews of the program history and individual tests have also available in Refs. [30] and [31].

2.1.2.1 Program Overview

"Project Rover" began at Los Alamos National Laboratory (then called "Los Alamos Science Laboratory") as a research program tasked with the goal of harnessing nuclear energy for the propulsion of ballistic missiles. Rover advanced the state-of-the-art in the design and fabrication of lightweight, solid-core, gas-cooled nuclear reactors and fuel elements. In 1961, after NASA took over joint control of Rover, industry contractors Westinghouse and Aerojet Gencorp were tasked with

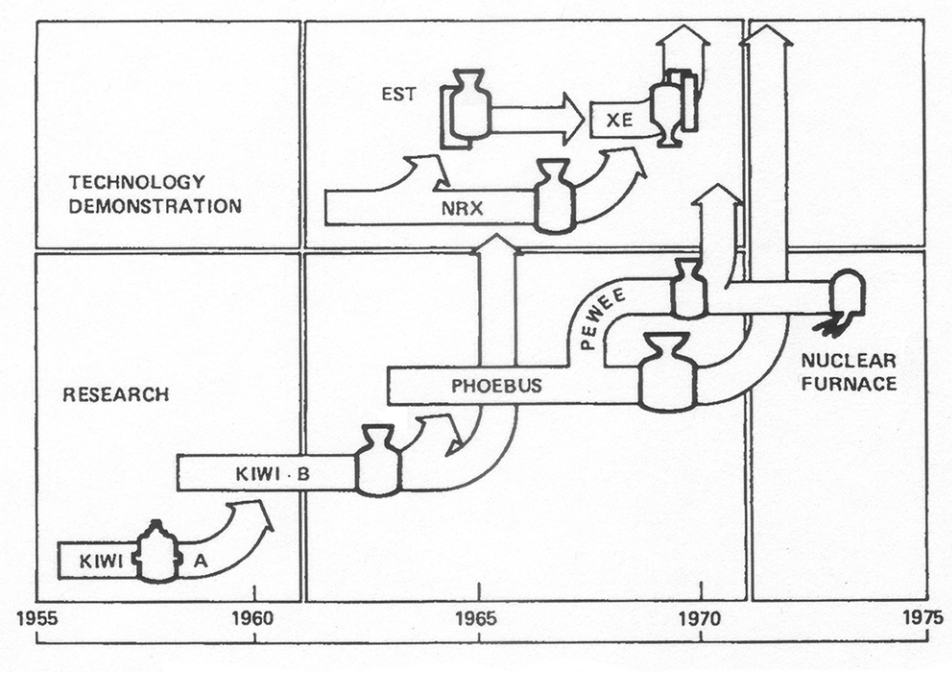

Figure 2.1: Timeline of Rover/NERVA reactor development [13].

developing a flight-ready engine based on the Rover reactors. This engine was called the "Nuclear Engine for Rocket Vehicle Applications" (NERVA), a name which is now more commonly associated with the program itself [32, 13]. Figure 2.1 shows a timeline of various reactor families developed during this time. The lower half of the figure, marked "Research," lists the families of test reactors and engines developed at LANL through Rover. The upper half, marked as "Technology Demonstration," lists the NERVA engines.

Rover produced two main lines of engines: KIWI and Phoebus. The KIWI line was named after the Kiwi, a large flightless bird native to New Zealand, because system weight and flight-worthiness was judged less important than advancing reactor design in this family. The original KIWI-A reactor produced 100 MW power did not include a nozzle so a corresponding thrust is unknown. The KIWI-B family

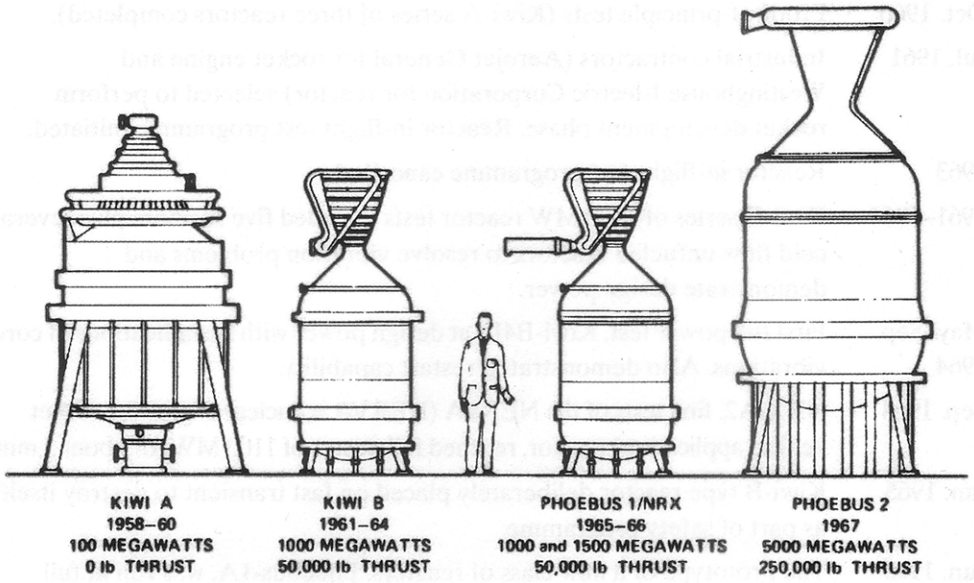

Figure 2.2: Rover/NERVA reactor size comparison [3].

redesigned the reactor and added a nozzle, increasing the performance to 1000 MW power and 222 kN thrust. The Phoebus 1 reactor followed, adding reactor support elements called "tie tubes," providing up to 1500 MW of power, 222 kN thrust, and (most importantly) improved survivability. The Phoebus 1 reactor design was the basis of the NERVA engines. The Phoebus 2 tested the upper limits of engine size, producing 5000 MW of thermal power and 1112 kN thrust [13]. Figure 2.2 shows a comparison of the size of these engines families.

2.1.2.2 Detailed Studies

During the NERVA program, some early studies were published on the analysis of NTR reactors, engines, and vehicles. In 1962, Bogart and Lantz examined the effects of heat generation and reactor control on a NTR. They analyzed the effect of

neutron reflectors and power profile tailoring on the core temperature distributions, showing that tailored axial power profiles reduce the axial temperature gradients in the fuel and thus the stress on the material [33].

Ellerbrock, *et al.* presented the analysis of thermal stress, flow stability, and two-phase flow in a nuclear thermal rocket core. They showed that the sizing of coolant channels has a strong impact on the temperature gradient, and thus thermal stress and ultimately, survivability of a fuel element. They also provided analytical representations for the convective properties of two-phase hydrogen, for use in modeling NTR engine startup, when the nozzle coolant ducts and reactor coolant channels are not hot enough to immediately gasify the liquid hydrogen coolant [34].

In 1964, Beckwith and Johnson compared the performance of nuclear thermal and chemical rockets for several missions, thrust levels, and trajectories. They examined the impact of propulsion system type on orbital velocity, vehicle staging, engine duration, launch weight, *etc.* and concluded that substituting a nuclear-powered 3rd-stage into a Saturn V configuration could provide 30% greater payload capacity to the Moon than a traditional chemical stage [35].

Altseimer *et al.* examined the operating modes and proposed trajectory of a NERVA-powered Earth-to-Moon shuttle vehicle. They concluded that reactor performance is predominantly limited by the survivability of the fuel at high temperatures. Other limitations of the proposed NERVA system were decay-heat cooling, which required excess propellant and prevented a separate power-generation mode [36].

2.1.2.3 Small Nuclear Rocket Engine

The engines originally developed for the NERVA program were large, high thrust engines intended to propel ICBM's and manned rockets to Earth orbit. However, as these large NTR engines and reactors were being developed, liquid-fueled chemical rocket technology also advanced greatly. By the end of the NERVA program, it was clear that the more appropriate use of nuclear engines would be in space propulsion, either as the upper stage of a Saturn V, or transported to LEO in the Shuttle cargo bay. As such, near the end of the NERVA program, a "Nuclear Engine Definition Study" was performed at LANL in order to recommended the next generation of NTR engine to be developed. This study designed what is now known as the "Small Nuclear Rocket Engine," a compact, lower thrust NTR engine, intended for in space missions. Extensive details for the SNRE design may be found in Refs. [37]–[39]. A brief summary of the engine will be presented here.

The SNRE was designed with two operating points in mind: one reusable design intended to act as a shuttle from low Earth orbit (LEO) to geosynchronous orbit (GEO), and another higher performance design intended as a one-way engine to launch scientific payloads to the outer planets. As shown in Table 2.1, the designs vary only slightly. The primary differences between the two designs are the reactor power and chamber temperature. By decreasing the peak reactor temperature by only 2% and reactor power by 5%, the multi-mission engine decreases the loss of fuel element mass, thereby increasing its reusability.

Although a significant departure from the large NERVA engines of the time,

Table 2.1: SNRE design points [37].

Parameter	Reusable	Single
Duration, h	2	1
Cycles	20	3
Specific impulse, s	860	875
Thrust, kN	71.72	72.98
Flow rate, kg/s	8.5	8.5
Chamber temperature, K	2633	2696
Chamber pressure, Pa	306.6	310.3
Reactor power, MW	354	367

the smaller thrust and power levels of the SNRE have carried over to nearly all of the NERVA-derived engines assumed for modern BNTR vehicles.

2.1.2.4 Summary

NERVA was terminated in 1973 because NASA no longer had an exploration mission that required nuclear propulsion. The program, however, was considered a technical success, having brought about the development of hot-bleed and expander-cycle NTR engines, major advancements in composite fuel technology, and successfully demonstrated the feasibility of NTR engines for real missions.

2.1.3 Space Exploration Initiative: 1989-1991

Without government support, NTR research lay dormant for nearly two decades, until revived by the Space Exploration Initiative (SEI), which officially ran from 1989-1991. SEI was an ambitious program that sought to extend American explo-

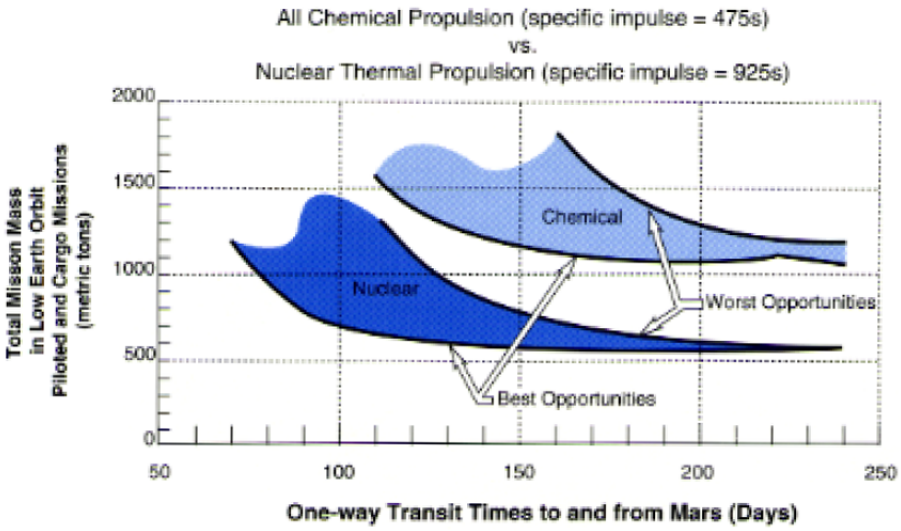

Figure 2.3: Required launch mass vs. transit times for Mars long-stay missions [41].

ration of space by developing Space Station Freedom, sending humans back to the Moon, and eventually on to Mars. The SEI "90 Day Study" specifically identified NTR propulsion as a major enabling technology for manned exploration of Mars. This study showed that NTR propulsion could reduce one-way travel times from 18 months to 7 months for a fixed mass in low earth orbit, or could reduce launch mass (and thus costs) by 50% for a fixed mission duration [40].

In May 1991, the "Synthesis Group on America's Space Exploration Initiative" published their examination of SEI, which further quantified the benefits of NTR propulsion for Mars. They examined all possible launch dates from 2008–2022 and plotted IMLEO against transit time for long-stay missions and mission duration for short-stay missions [41]. These results are shown here as Figs. 2.3 and 2.4, respectively.

Figure 2.3 shows that, for a given launch opportunity, NTR propulsion can

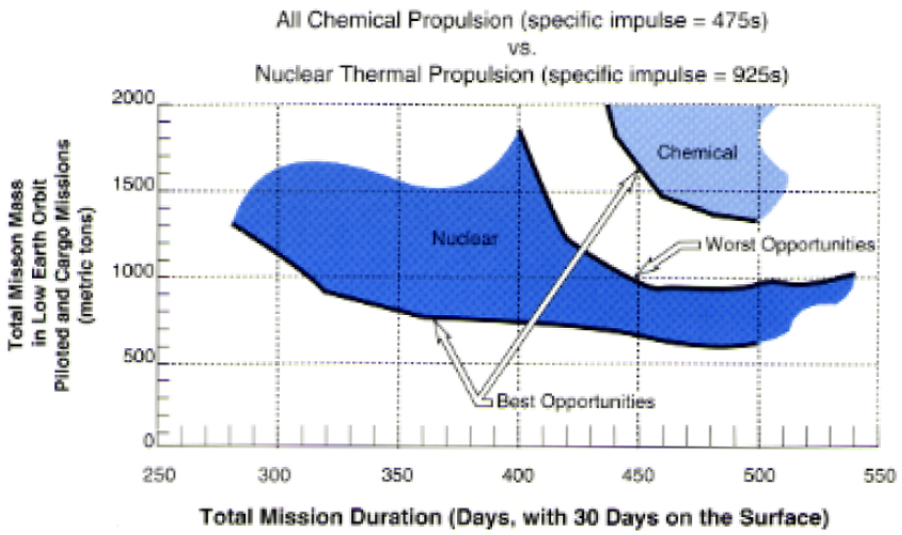

Figure 2.4: Required launch mass vs. mission duration for Mars short-stay missions [41].

consistently provide mass savings of more than 500 metric tons over chemical propulsion and requires a shorter transit time. Or, as concluded in the 90 Day Study, the mission mass can be cut in half for a given transit time, or *vice versa*. The benefits of nuclear propulsion are even more evident for short-stay missions, where mass savings of approximately 1000 metric tons and durations 100 days shorter are possible, as shown in Fig.e 2.4. Primarily due to exorbitant program costs (˜$500 Billion over 20-30 years), SEI was not funded past 1990. Despite this programmatic failure, SEI did succeed in renewing interest in Mars and NTR propulsion.

2.1.4 Modern NTR Developments

Interest and research in NTR propulsion has continued to increase since the early 1990's. Modern concepts seek to add to the capability demonstrated during the NERVA program by modifying the reactor configuration, changing the reactor

fuels, or adding chemical combustion stages to augment the vehicle thrust. Three specific technologies that have received a great deal of interest are NERVA-derived reactors and engines, CERMET fuel reactors, and oxygen afterburning. Bimodal operation is another modern technology that has been covered to such an extent that it is presented in its own section.

2.1.4.1 NERVA-Derived

Some recent concepts intend to build on the extensive development that took place during the NERVA program. These so-called "NERVA-derived" engines are based on the same carbon composite fuel elements from the original NERVA program, but vary other aspects of the engine design to increase the specific impulse or thrust-to-weight of the engine.

The ENABLER is a NERVA-derived engine developed by Rocketdyne for SEI, and uses the same NERVA composite fuel elements with a redesigned propellant delivery system for a higher chamber pressure and temperature. The benefit of this design is a higher specific impulse and thrust-to-weight than a traditional NERVA engine, with the perceived risk reduction of using the proven NERVA fuel [30].

The ENABLER was of such interest to NASA during SEI that they used it as the basis of their new NTR modeling tool. This tool, called the "Nuclear Engine System Simulation" (NESS), was developed in 1991 to support the NTR modeling studies under SEI. NESS was developed by modifying Aerojet's ELES ("Expanded Liquid Engine Simulation") for use with the Westinghouse ENABLER

engine design [42]. NESS continued to evolve by adding the ENABLER-II reactor design and the capability to scale fuel elements to represent advanced technology levels [42, 43]. As of early 2007, NESS remains a standard NTR modeling tool at NASA Glenn.

Petrosky derived the thermodynamic impact of scaling the fuel element geometry in a NERVA-derived reactor. He found that proportionately scaling a NERVA fuel element to a smaller size increased the power density and operating pressure for the same thermal stresses, thus increasing the thrust-to-weight of the engine. He calculated that a 30% reduction in element size (length, width, channel diameter) would more than double the engine's thrust-to-weight [44].

Fittje and Buehrle used the NESS code to examine the sensitivity of NTR performance to the propellant feed system. They compared single- and dual-turbopump assemblies and studied a "pump out" scenario. They found that NESS was able to closely mimic the SNRE engine design and produce state point data throughout the engine, but also expressed a desire for a higher-fidelity NTR model [45].

2.1.4.2 Ceramic-Metallic (CERMET) Fuels

Ceramic-metallic (CERMET) fuel materials are of interest for their high resistance to hydrogen corrosion, relatively high temperature limits, and low weight. Significant research into CERMET NTR engines has been performed by many at Pratt & Whitney (PW). In 1992, Parsley presented the Pratt & Whitney design for the XNR2000 engine. As shown in Fig. 2.5, the CERMET fuel allows higher

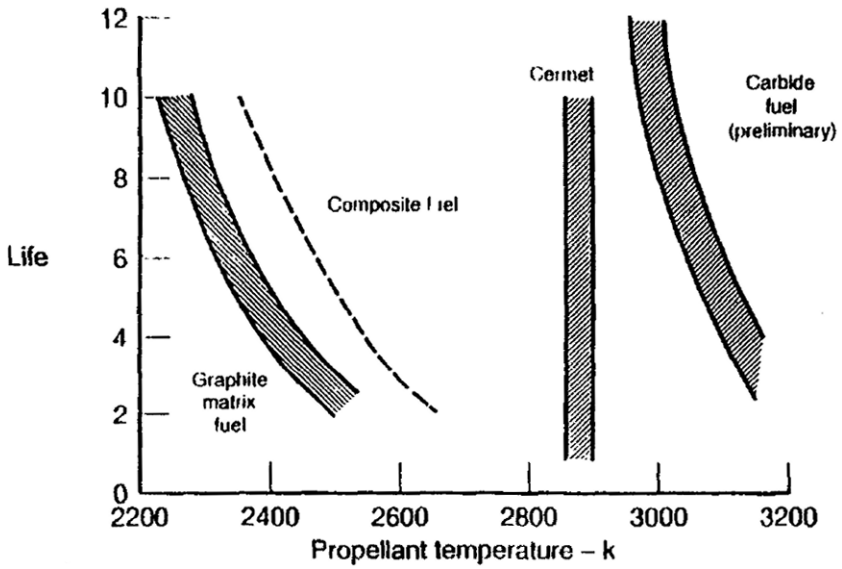

Figure 2.5: Reactor fuel material temperature limits [46].

propellant temperatures than NERVA-based graphite and composite fuel, and thus higher thrust and specific impulse [46].

The XNR2000 evolved into the ESCORT reactor, which Feller and Joyner have studied for Manned Mars vehicles [23, 47] and Mars surface power [48]. Joyner, *et al.* have also adapted the ESCORT for deep space nuclear electric propulsion [49] and oxygen-afterburning [50]. Many recent comparisons between CERMET, graphite, graphite-composite, and carbide reactor fuels for manned Mars missions concluded that CERMET shows the most promise based on better hydrogen corrosion resistance, higher resistance to thermal stress, lower weight, and lower development costs than carbide fuel [51]–[54].

2.1.4.3 Oxygen Afterburning

As indicated above, the chamber temperature of NTR engines is generally limited by the fuel element materials. The addition of an oxygen afterburner to a hydrogen-propelled NTR has been studied in order to increase the nozzle chamber temperature and thrust, with a small penalty in specific impulse. The concept of a liquid oxygen-augmented NTR (LANTR) was first proposed in 1994 and has been discussed thoroughly Bulman, *et al.* at Aerojet and Borowski, *et al.* at NASA Glenn Research Center [55]. In 1996, Borowski and Dudzinski discussed the use of lunar oxygen production ("in situ" propellants) to enhance the thrust of a traditional NTR for Earth-Moon transportation [56]. The following year, Borowski and Dudzinski presented the design for a LANTR-powered, 24-hour Earth-Moon commuter mission loosely based on the movie "2001: A Space Odyssey." They found that the engine, pictured in Fig. 2.6, could be performance-optimized for the trajectory by changing the oxygen/hydrogen mixing ratio in the nozzle [57]. Stancati, *et al.* examined the use of in-situ oxygen production for LANTR missions to the Moon and Mars. They concluded that in-situ propellants are only beneficial when produced at the immediate spacecraft destination [58, 59]. In 2003, Bulman and Borowski presented an integrated propulsion-vehicle-trajectory analysis for deep space missions. They found that missions optimization must balance low IMLEO and fast transit time, and that LANTR engines can do so by throttling between high thrust, low I_{sp} and low thrust, high I_{sp} modes by varying the oxygen mixing ratio [17].

Through the late 1990's and early 2000's, Aerojet refined the development of

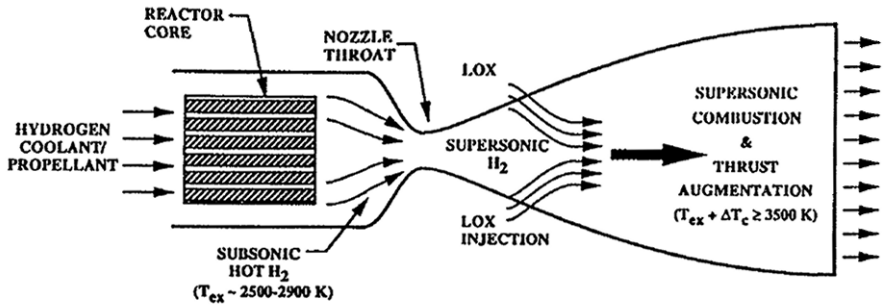

Figure 2.6: LANTR Conceptual Sketch [57].

the LANTR with CFD analysis and experimental validation. In 1999, Glenn and Bulman presented the CFD analysis of the oxygen injection in the LANTR nozzle. Their results showed that supersonic combustion can be maintained and that a multi-zone injection scheme allows high combustion efficiency producing nearly triple the thrust of a standard NTR. [60]. In 2000, Bulman and Neill demonstrated the feasibility of the LANTR concept experimentally, by simulating the NTR exhaust with that of a chemical rocket. A comparison of inert and reacting flows showed that the addition of supersonic combustion does augment the thrust more than mass addition alone. These experiments found a 40% increase in thrust due to the oxygen afterburning, with significant combustion occurring beyond the nozzle exit [14]. Follow-on experiments found similar results for larger nozzles with higher expansion ratios [15, 16]. Finally, in 2004, Bulman, *et al.* presented the design for a LANTR system integrated into Pratt & Whitney's ESCORT engine. They found that the oxygen-afterburning hardware could be added to a traditional NTR with little impact on the weight and volume of the engine [18].

2.2 Bimodal Operation

2.2.1 Historical Development

Near the end of the Rover/NERVA program, the concept of using a common nuclear reactor for providing propulsion and electric power became prevalent. Such a design was originally called "dual-mode" operation, but is now more commonly known as "bimodal." In 1971, Beveridge first proposed using the core support "tie tube" elements in a NERVA reactor as the heat source of a closed-loop power system. He found that a reactor designed for 75000 lb (334 kN) of thrust could run at a low-power mode and produce 25 kW of electric power from a Rankine cycle power system. Furthermore, the power cycle could be used directly to remove the propulsion mode decay heat, reducing the required mass of excess hydrogen by 50% and the reactor cool down time by 90%. This coolant mass reduction was found to be sufficient enough to make up for the added weight of the power system hardware [19]. Several other studies applied Beveridge's system to the SNRE, demonstrating that it could produce power levels of 10-25 kWe [13].

2.2.2 Post-SEI Studies

As with nuclear propulsion, the interest in BNTR resumed immediately following SEI. In 1994, Gunn, Hedstrom, and Hundal presented an analysis of the tie tube elements in a BNTR system based on the SNRE, as described above. They determined that the ZrC insulation sleeves in the SNRE design prohibit effective heat transfer to the tie tube coolant, and that modifications of the material and

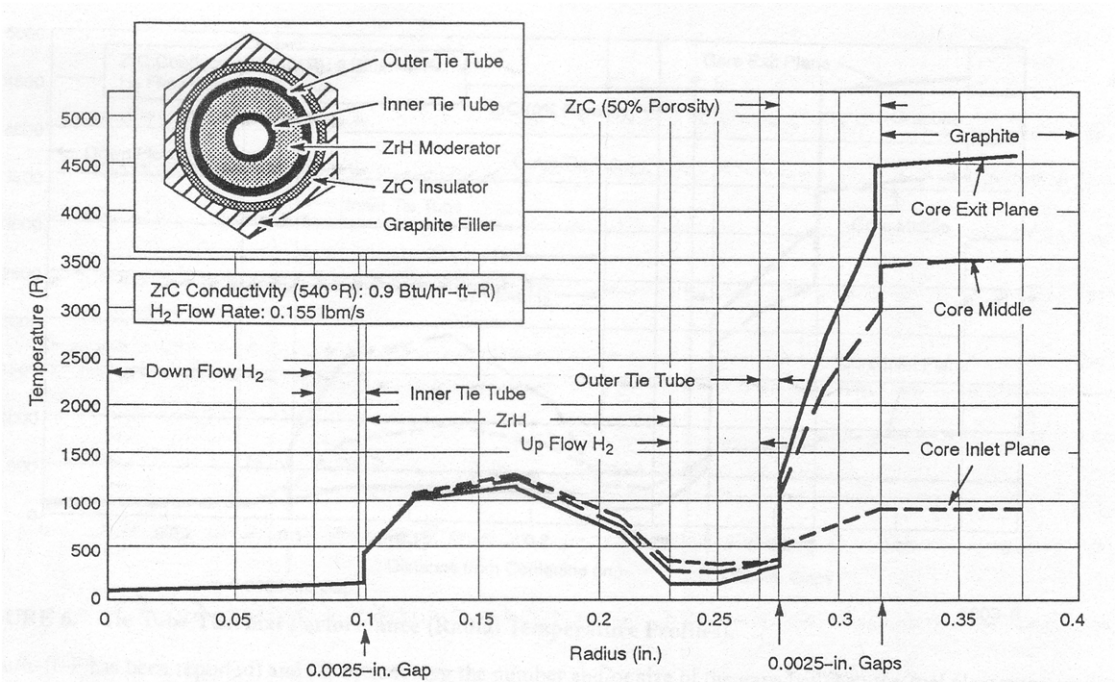

Figure 2.7: Tie tube thermal performance [20].

geometry of the tie tubes could enable a 245–570% increase in the thermal performance of the elements [20]. Figure 2.7 illustrates how the ZrC insulator layer of a NERVA tie tube allows very little heat to reach the coolant channels.

Zweig and Hundal also examined the tie tube component design as well as the choice of power conversion cycle for a BNTR system. They chose a Stirling cycle for its low system mass and required radiator area. They found that reducing the reactor length from 1.32m (the NERVA standard) to 0.89m (the current SNRE-based standard), the reactor thrust-to-weight increased from 3.6 to 4.4 [21].

Kirk, *et al.* assessed the feasibility of using large 75000 lb. (334 kN), 1500 MWt NERVA reactors to produce electrical power on the order of 10 MW for large electric propulsion engines. They concluded that the thermal degradation and fuel burn-up effects of extended operation at such high power levels limit the use of

BNTR systems to power generation levels below about 50 kWe [61]. No other study has examined power generation levels that high.

During the mid-1990's, several studies examined the use of BNTR technology for satellite positioning and power generation. Buden, *et al.* compared several BNTR fuel systems with the goal of producing 10-20 kWe power with a system mass below 1000-2000 kg. They concluded that such a system is feasible but the development costs at that time would make it unattractive [62]. Buksa, et al. compared low-thrust propulsion systems for the purpose of boosting satellites from LEO to GEO. They found that a BNTR could to provide an 80% increase in payload capacity over a chemical rocket, and order-of-magnitude shorter transfer time than electric propulsion. [63]. In 1995, Culver and Bulman presented a common BNTR architecture that could be profitable by launching and powering several high power communication satellites into high Earth orbit [64]. Finally, Polansky, *et al.* [65] and Weitzberg and Warren [66] presented designs for low-power BNTR engines using CERMET fuel for reduced reactor size and weight.

2.2.3 Design Reference Mission 4.0

Over the years, the NASA Mars Exploration Study Team has published an evolving "Design Reference Mission" (DRM) for the manned exploration of Mars. The most recent officially published DRM is version 3.0, June 1998. DRM 3.0 assumes a baseline design with a "split/sprint" mission profile, where the bulk of the cargo is pre-deployed on an efficient, low energy trajectory, followed three years later

by a manned spacecraft at a higher energy trajectory. This scenario, as illustrated in Fig. 2.8 reduces the travel time and corresponding health risks for the crew while providing for optimal payload in the cargo missions. The two cargo vehicles contain a surface cargo lander (which in turn contains surface payload and the Mars ascent stage) and the Earth Return Vehicle (ERV). The manned vehicle consists of the Mars descent stage and the surface habitat. In DRM 3.0, all vehicles use NTR propulsion for the trans-Martian injection (TMI) maneuver, solar electric power throughout the mission, and aerobraking for Mars capture and entry. The aerobraked payload of each vehicle separates from the spent NTR stage after TMI, at which point the NTR stage places itself into a disposal trajectory. The ERV uses chemical propulsion for the return trip [67].

DRM 3.0 has some limitations that have been addressed with more recent concepts. One major limitation of DRM 3.0 is abort capability. After TMI, the only abort scenarios available are to Mars surface or to the ERV in Mars orbit. For a 2014 manned mission opportunity, the Mars orbit abort scenario would leave the crew in zero-gravity for 914 consecutive days before reaching Earth, which is a considerable health risk [67]. Furthermore, as examined by Dissel, this mission lacks departure abort capability because the Earth re-entry capsule is pre-deployed with the ERV [68]. Another limitation of DRM 3.0 is that the ERV, because of being pre-deployed, will remain in space unused for over four years before having to safely return the crew to Earth [67]. This protracted period of time increases the probability of damage and/or degradation due to ambient radiation or other environmental hazards.

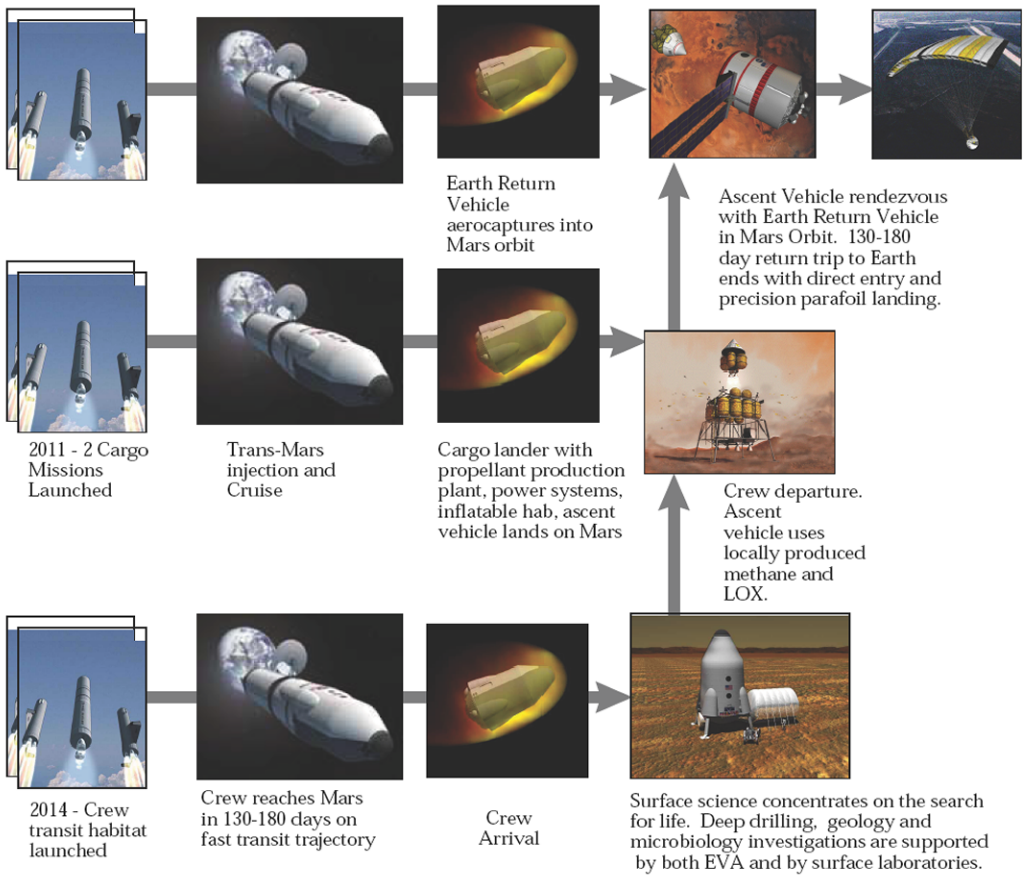

Figure 2.8: Mission overview for DRM 3.0 [67].

Shortly after the release of DRM 3.0, Borowski, *et al.* of NASA Glenn Research Center published a modified mission that uses BNTR technology to enhance the capability and reduce the risk of a manned Mars mission. BNTR engines enable fully propulsive missions, where nuclear propulsion is used for TMI as well as Mars capture and Earth Return maneuvers. The power mode capability allows for high data-rate communication and an active hydrogen cooling system to prevent boil-off. This removes the need for advanced aerobraking shells and photovoltaic power systems, reducing the IMLEO and launch and development costs of the mission. By using the BNTR system throughout the mission, a common Mars Transfer Vehicle (MTV) can be used for the outbound and return trips, addressing the concerns of abort capability and vehicle reliability discussed above [4]. Figure 2.9 illustrates the basic timeline for this mission.

These modifications to DRM 3.0 have been widely adopted and, through a series of annual papers describing mission and vehicle details, are now known collectively as "DRM 4.0." These publications vary somewhat in their mission and some of the design details, but all rely on BNTR engine to provide propulsion and power to a vehicle based on the MTV pictured in Fig. 2.10.

In 1999, Borowski, Dudzinski, and McGuire proposed the addition of artificial gravity (AG) capability to the vehicle presented in Ref. [4]. They found that the reduced mass of the BNTR MTV allowed for the addition of excess reaction control system (RCS) propellant. The excess propellant can then be used to provide AG through controlled end-over-end rotation of the spacecraft. The system is able to simulate Mars gravity for the outbound mission and 0.8 times Earth gravity for

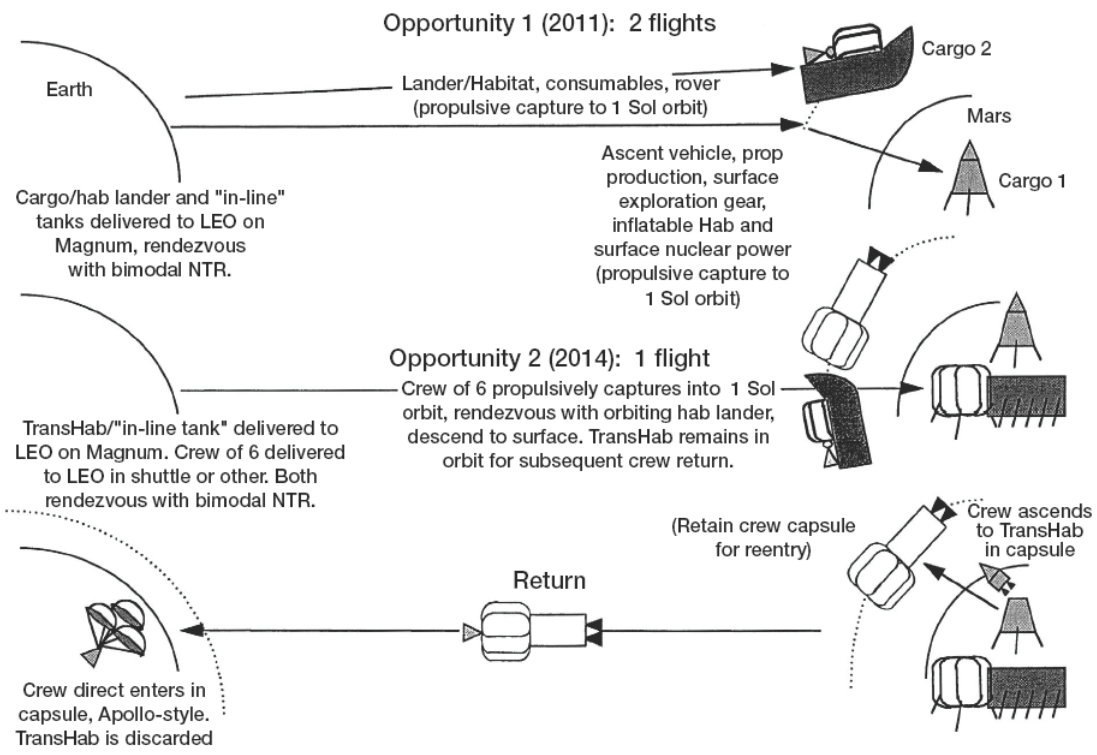

Figure 2.9: Mission overview for DRM 4.0 [67].

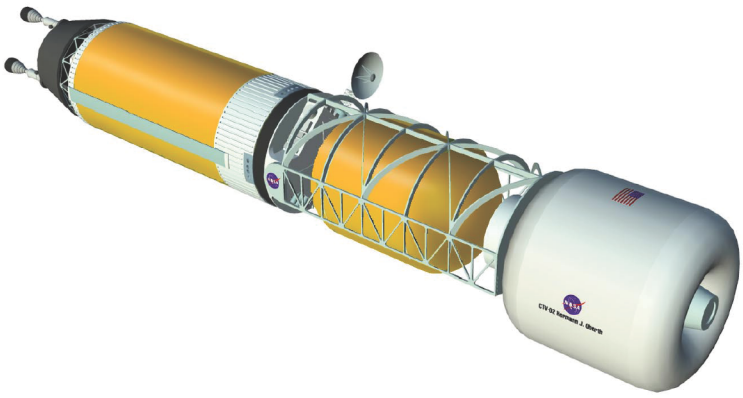

Figure 2.10: BNTR-powered Mars Transfer Vehicle [4].

the return, allowing the crew to train and prevent atrophy. The AG system can also provide on-orbit gravity for the Mars orbit abort scenario, addressing another limitation of DRM 3.0 [5]. In 2000, Borowski, Dudzinski, and McGuire applied the AG-enabled BNTR design to an exploration vehicle for "near Earth asteroids" as well as Mars [6]. The next year, a revised mission plan for the AG BNTR was presented for a later Mars opportunity [7]. At the same time, Marcus, *et al.* evaluated an integrated vehicle-trajectory design for the BNTR-powered MTV. They found that the ability of the power generation mode to remove reactor decay heat was a larger driver for its design than simply providing the required vehicle power [69].

2.2.4 Other Recent BNTR Studies

Several recent studies have examined various subsystems of the DRM 4.0 vehicles. Fusselman, *et al.* compared several tie tube configurations for a SNRE-based BNTR engine. The most attractive option used separate passages in the same tie tube for the hydrogen in propulsion mode and a mixture of inert gases in both modes [22]. Christie and Plachta evaluated the heat transfer requirements and design of a cooling system to eliminate hydrogen propellant boil-off for the BNTR-powered MTV. Active cooling devices in the form of a cryo-cooler and structural heat shields were employed in addition to traditional passive cooling devices, such as multi-layer tank insulation and solar-reflective coatings. These systems required 9.3 kW of power, which is significantly lower than the 15 kW allocated by DRM

4.0 [70]. Finally, McCurdy, et al. performed vehicle sizing trade studies on the DRM 4.0 architecture for three different missions. A vehicle employing several smaller (lower thrust) engines would allow for less expensive ground testing by not requiring as extensive exhaust decontamination. Higher reactor exhaust pressures lead to a higher thrust-to-weight and more compact engines, but also required heavier turbomachinery and piping. Similarly, a higher reactor temperature would improve specific impulse, but also increase thermal stresses on the fuel elements [71].

2.3 Reactor-Driven Brayton Cycle Power Systems

2.3.1 History

Closed-Brayton-cycle (CBC) power systems are a common choice for dynamic power conversion for power levels from tens to hundreds of kilowatts (the range of power typically required for manned spacecraft). Despite this fact, no nuclear-heated Brayton cycle power system has ever been in space. Although nuclear space power research began with the "Systems for Nuclear Auxiliary Power" (SNAP) program at the same time as Rover/NERVA, only one US reactor-driven power system has been in space. This system is the SNAP 10-A, illustrated in Fig. 2.11, a 0.58 kWe thermoelectric generator that was launched in 1965 in order to drive a 10 N ion engine [3].

The SNAP-10A was later followed by SP-100, a joint NASA / DOE venture that ran from 1983–1993 and focused on developing reactor technology for space.

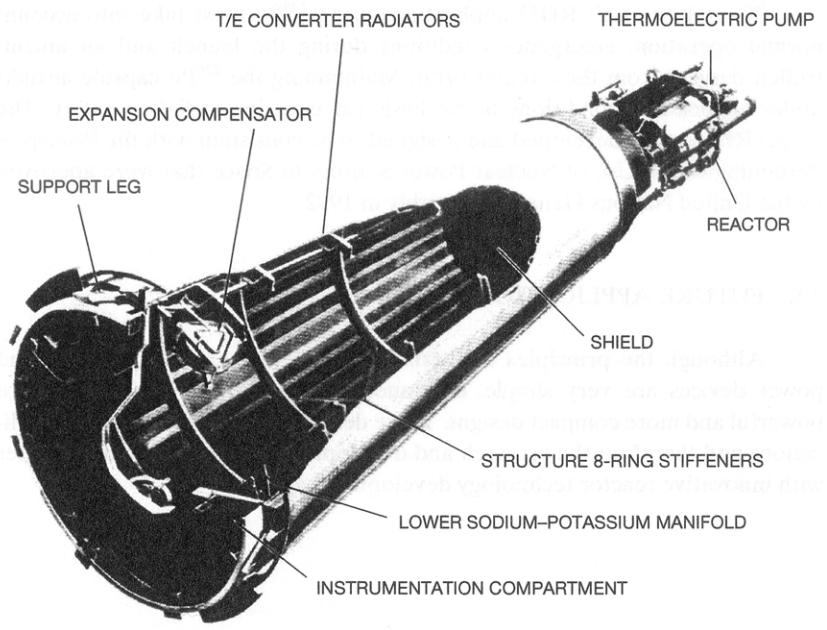

Figure 2.11: SNAP-10A, the only US reactor-based power system in space [3].

The SP-100 power system was similar to SNAP-10A, also using thermoelectric conversion with a small reactor. The Soviet/Russian space program also used reactors extensively, but their TOPAZ system also used passive thermionic power conversion at relatively low power levels [3].

The first discussion of a nuclear-powered Brayton cycle was near the end of the Rover/NERVA program, when Boman and Gallagher discussed the application of NERVA reactor technology to a Brayton cycle power systems, by using NERVA-derived fuel elements for the heat source of a CBC power system [72]. Since that time, there has been extensive interest in nuclear-powered Brayton cycle power systems, but no systems have actually gone into use.

2.3.2 Prometheus Project: Recent Nuclear Brayton Cycle Development

Project Prometheus is NASA's most recent program for the development of nuclear propulsion and power systems. Its original goal was to advance reactor design for electric propulsion systems for deep space exploration as well as NTR for manned missions closer to Earth [73]. The main focus of Prometheus was the Jupiter Icy Moons Orbiter (JIMO), a deep space vehicle that would use reactor-driven CBC to drive a nuclear electric propulsion system and explore the Jovian moons Callisto, Ganymede, and Europa [74]. As of early 2007, NASA has redirected the focus of Project Prometheus entirely towards fission surface power for the Moon [74, 75], but this effort has lead to an extensive amount of work on nuclear-heated CBC systems that will be briefly discussed below.

2.3.2.1 CBC Work at Sandia

In recent years, Wright, *et al.* at Sandia National Laboratories have presented analytical and experimental work as part of the development of a closed-loop test cell used to analyze the experimental performance of a reactor-powered Brayton cycle. In 2003, Wright developed a model of steady-state and transient operation of a reactor-coupled Brayton cycle power generation system. The model showed that the system is naturally stable and "load following" for step changes in power load, and results helped identify the unique reactor control requirements for such a system [76]. In 2005, Wright and Sanchez modeled the transient response of

a reactor-heated closed Brayton cycle generator system in SIMULINK. An eight-stage start-up scenario is presented, along with the thermal response of the system. The simulation verified that the Brayton cycle system could be controlled by the combination of a turbo-alternator controller and reactor controller [77].

Also in 2005, Wright, *et al.* presented the experimental setup used to model a nuclear-heated Brayton cycle generator. The turbo-alternator subsystem is based on pre-existing hardware, while the reactor and radiator components are currently approximated with an electric heater and water chiller, respectively, with future plans to add in nuclear components [78]. Lipinski, *et al.* also proposed an experimental setup used to test the Brayton cycle generator of Ref. [78] attached to a nuclear reactor[79].

2.3.2.2 CBC Work at NASA Glenn

At the same time period as the work above, NASA Glenn Research Center has been performing similar analysis of nuclear-heated CBC power systems, while developing an intermediate-fidelity computer model such systems. In 2004, Mason presented the design and analysis of a nuclear-powered Brayton-cycle generator. He found that an optimum compressor inlet temperature exists which results in the minimum possible engine system mass, where lower compressor temperatures lead to larger radiator areas while higher temperatures require larger recuperators and gas coolers [80].

Later that year, Barrett and Reid used NASA's "Closed Cycle Engine Pro-

gram" (CCEP) CBC model to evaluate the system mass and entropy impacts of changes in peak operating pressure, compressor pressure ratio, and working fluid composition of a Brayton cycle generator. They acknowledge that the reactor has the lowest-fidelity of all subsystem models and found an optimum compressor pressure ratio that minimizes system mass [81]. In 2005, Johnson and Mason used CCEP to examine design trade studies and off-design performance for a Brayton cycle power generation system. Peak design points were chosen as they concluded that reducing shaft speed and turbine-inlet-temperature in tandem would provide the most effective means of reducing the required heat input while preventing the liquid metal in the radiator from freezing [82].

In 2006, Lavelle presented a summary of the "Closed Cycle System Simulation" (CCSS), a nuclear-heated CBC model based on CCEP, but built into NASA's Numerical Propulsion System Simulation (NPSS) modeling framework [83]. That year, Johnson and Hervol validated CCSS against experimental CBC data for steady-state and transient operation. The steady-state data is within 1% and the transient looks very good as well, verifying the accuracy of CCSS for modeling Brayton cycle generators [84]. Finally, Johnson and Mason used CCSS to examine a power-generation system with two Brayton-cycle generators sharing a common reactor and gas inventory. They examined several off-design conditions which included a speed imbalance, one generator idling, and startup scenarios. They concluded that the thermodynamic response of the shared gas inventory caused several negative consequences that would not be expected with independent generation systems [85].

Chapter 3

BNTR Engine System

A BNTR engine consists of two separate thermodynamic cycles that share a common reactor heat source. In propulsion mode, hydrogen gas is heated by passing through the reactor fuel elements and then expands through the nozzle, producing thrust. Engine cooling flow through the nozzle, reactor periphery, and special support elements called "tie tubes" is used to drive the turbopump(s). In power generation mode, the hydrogen flow ceases and an inert gas mixture, typically helium and xenon (He-Xe), is pumped through the tie tubes, heating a closed loop Brayton cycle. This chapter will provide further detail into the operation of each of these modes, specifically the flowpath architecture and cycle analysis.

3.1 Propulsion

3.1.1 Architecture

In propulsion mode, the configuration of a BNTR is similar to that of a chemical rocket. The primary difference is that the reactants of a chemical rocket act as both heat source and propellant while a NTR uses a stationary reactor to add heat to the non-reacting hydrogen propellant that passes through it. A common NTR

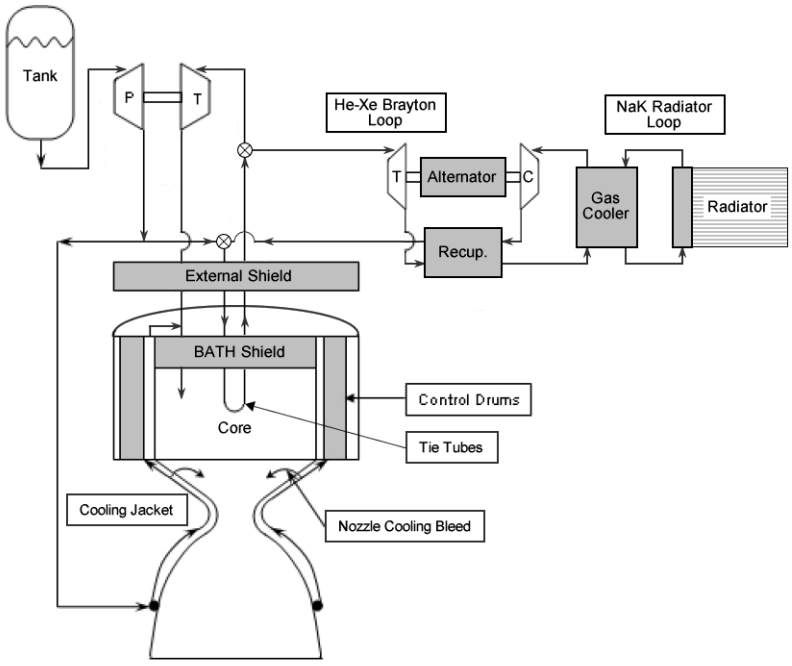

Figure 3.1: Schematic of a BNTR engine system, modified from Ref. [45].

configuration is the expander cycle, as shown in the left of Fig. 3.1. An expander cycle NTR pre-heats the fuel by using it to cool the nozzle as well as several reactor subsystems. A portion of this pre-heated cooling flow drives the turbopump(s), which exhaust along with the remainder of the coolant/propellant into the reactor and nozzle. In this flowpath, liquid hydrogen is pumped to two parallel cooling paths. The first path, shown at the far left of Fig. 3.1, goes to the nozzle cooling jacket, which cools the hottest portion of the nozzle. The majority of the exit flow from the cooling jacket continues on to the control drums and reflector at the periphery of the reactor core, while a small portion is reserved for bleed cooling of the nozzle wall. The control drum exit flow then enters the forward end of the reactor core.

The second path (shown turning to the right after leaving the pump in Fig. 3.1) leads to the tie tubes within the reactor core. Tie tubes are U-shaped elements that act as dual-pass heat exchangers, removing as much heat as possible from the reactor core in order to drive the turbine(s). The turbine exhaust then joins the control drum exhaust at the reactor core.

In addition to tie tubes, the core contains many fuel elements, which are heated by the sustained fission of uranium fuel and contain small longitudinal holes, often called "channels." By passing through the hot channels, the propellant heats up while also cooling the fuel elements. The reactor exhausts directly to the nozzle, where the thermal energy gained in the reactor is converted kinetic energy, producing thrust.

3.1.2 Theoretical Performance

The performance of a rocket engine is generally characterized by its thrust and specific impulse. The thrust of a generic engine, as shown in Eq. 3.1, is created by the change in momentum of the propellant and by the pressure difference across the engine. For a rocket engine, the propellant mass flowrate is constant throughout and the inlet velocity is zero, so the thrust equation is simplified to the form of Eq. 3.2.

$$T = \dot{m}_e u_e - \dot{m}_o u_o + (p_e - p_a) A_e \tag{3.1}$$

$$T = \dot{m} u_e + (p_e - p_a) A_e \tag{3.2}$$

Typically, it is assumed that the nozzle will be designed such that the exit pressure is equal to ambient, and thrust is a function of the exit flow rate and velocity alone. For an in-space engine like an NTR, the ambient pressure is zero, which would require an infinitely long nozzle to reach. As such, the thrust of these engines will depend on both the momentum and pressure.

Specific impulse is defined as thrust divided by the weight flow-rate of fuel, as shown in Eq. 3.3. By assuming that the nozzle is ideal and expands to ambient pressure, specific impulse is simply equal to the exit velocity divided by the gravitational constant. As discussed above, this assumption is not necessary valid for a real BNTR, but is still used here for the sake of simplicity.

$$I_{sp} = \frac{T}{\dot{m}g} = \frac{\dot{m}u_e}{\dot{m}g} = \frac{u_e}{g} \tag{3.3}$$

Specific impulse can be written in terms of the chamber conditions and exit pressure by examining the isentropic expansion of an ideal nozzle. For isentropic flow, the ratio of total temperature to static is a function of Mach number alone, as shown in Eq. 3.4. This equation also uses the fact that the total temperature at any location in the nozzle, by definition, is equal to the chamber temperature.

$$\frac{T_o}{T_e} = 1 + \frac{\gamma - 1}{2} M_e^2 \tag{3.4}$$

Equation 3.4 can then be rearranged to solve for the exit Mach number, which can also be written in terms of exit velocity and sonic velocity.

$$\frac{u_e^2}{a_e^2} = \frac{2}{\gamma - 1}\left(\frac{T_o}{T_e} - 1\right) \tag{3.5}$$

Both sides of Eq. 3.5 can then be multiplied by the exit sonic velocity squared, which

can then be written in terms of the exit temperature.

$$u_e^2 = \frac{2\gamma R T_e}{\gamma - 1}\left(\frac{T_o}{T_e} - 1\right) \tag{3.6}$$

Finally, the term T_o/T_e can be factored out of the fraction, T_e/T_o can be written in terms of the exit and chamber pressures, and the new expression can be combined with Eq. 3.3 to form a new expression for specific impulse.

$$I_{sp} = \frac{1}{g}\sqrt{\frac{2\gamma R T_o}{\gamma - 1}\left(1 - \left(\frac{p_e}{p_o}\right)^{\frac{\gamma-1}{\gamma}}\right)} \tag{3.7}$$

Equation 3.7 shows that, theoretically, specific impulse is a function of the propellant gas constant, chamber pressure, chamber temperature, and exit pressure. For an ideal nozzle, P_e is zero, and specific impulse is a function of chamber temperature alone, as shown in Eq. 1.3.

A brief examination of Eqs. 3.2 and 3.7 shows that thrust and specific impulse have opposite responses to increases in exit pressure, but both will benefit directly from higher exit velocity. From Eq. 3.6, exit velocity can be increased by increasing chamber temperature. As such, the thrust and specific impulse of a NTR will be maximized by designing the engine to operate at the highest chamber temperature possible. For a NTR, the chamber temperature is essentially the same as the reactor exit temperature, so the primary constraint for these engines is the temperature limit of the reactor, which is defined by the chosen fuel element material.

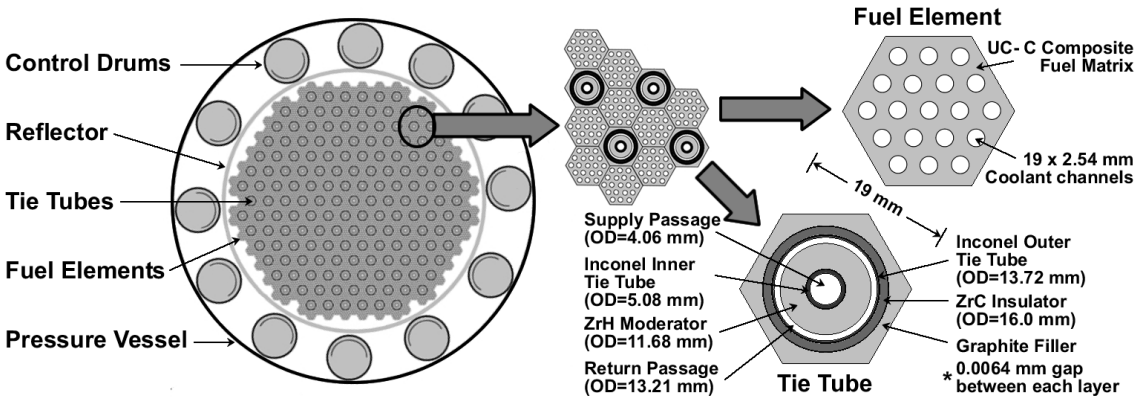

Figure 3.2: NERVA-derived reactor cross-section, modified from Ref. [45].

3.1.3 NERVA-Derived Reactor Design

3.1.3.1 Overview

As discussed previously, this project focuses specifically on the performance of a BNTR engine based on a NERVA reactor design. Such a system is generally referred to as "NERVA-derived." Several reactor designs were generated, however, over the course of the Rover/NERVA program. The work here is based on the Small Nuclear Rocket Engine (SNRE) design that was produced by the Nuclear Engine Definition Study at the end of the NERVA program, in 1972 [37]. The SNRE reactor contains several subcomponents, as illustrated in Fig. 3.2, and the full details of their operation can be found in Refs. [13], [37]–[38], and [31]. The beryllium reflector and control drums retain and control the flow of neutrons in the reactor core. The core consists of a bundle of hexagonal (or "prismatic") fuel elements and tie tubes. The reactor inlet hydrogen passes through small channels that run longitudinally through

the fuel elements, gaining thermal energy as it cools the core. NERVA-derived fuel elements are fabricated from a uranium carbide (UC)-graphite composite and all fuel element surfaces are coated with zirconium carbide (ZrC) to resist corrosion from the hot hydrogen propellant.

3.1.3.2 Pressure Vessel

The outermost subcomponent in Fig. 3.2 is the pressure vessel, which serves a relatively mundane purpose. As indicated by its name, the pressure vessel retains the coolant and propellant gases passing through the reactor and its periphery. This allows the engine to sustain high pressures and direct all of the propellant through the nozzle.

3.1.3.3 Reflector

The reflector is a multipart element several inches thick that fills the space between the pressure vessel and core, surrounding the control drums. The dark layer labeled as the reflector in Fig. 3.2 is actually the innermost "barrel" layer of the reflector. The reflector is made of beryllium and is designed to reduce the number of neutrons leaving the core (neutron leakage). Beryllium has a very low neutron absorption cross-section, which means that nearly all of the neutrons that strike it will bounce off, being reflected back into the core. The thickness of the reflector further reduces the neutron leakage by increasing the likelihood of neutron interactions. These interactions, however, produce some heat within the reflector,

so it is designed with many longitudinal coolant channels. By reducing leakage, the reflector increases the net neutron flux for a given fuel loading, allowing for a more compact, efficient engine [37].

3.1.3.4 Control Drums

The controls drums are located within the reflector and are the primary means of actively controlling the power level of the reactor. The SNRE design uses twelve control drums in total, which are independently actuated in diametrically opposed pairs. This is done to prevent uneven reactor heating in the event of control motor failure. One third of the surface of each drum is made of boron-copper, a neutron absorber. At idle, the boron control surfaces all fully face the reactor core, absorbing enough neutrons to prohibit a sustained fission chain-reaction. To increase the reactor power, the drums are gradually rotated so that less of the boron control surface is visible, and thus fewer neutrons are absorbed. The resulting increase in neutron flux causes more fission reactions, which are the source of the reactor power [37].

3.1.3.5 Fuel Elements

The reactor heat comes from the fission of U-235, which is contained in solid fuel elements made from a composite of UC-ZrC and graphite. The uranium enrichment and relative UC fuel loading is varied along each element and between elements across the reactor. This produces a controlled neutron/power distribution that is

designed to produce a relatively flat heating profile across the reactor diameter, and to focus the peak reactor heating within the middle of the reactor longitudinally, in order to reduce neutron leakage from the fore and aft ends of the reactor [37].

The cross-section of a NERVA-derived fuel element is illustrated in the upper-right corner of Fig. 3.2. Each element is hexagonal in shape and 19 mm wide, across the flats. The SNRE elements are 0.89 m long, but some of the larger NERVA engines reached lengths of approximately 1.3 m [13]. Each element contains 19 longitudinal coolant/propellant channels that are 2.54 mm wide. A typical reactor contains over 500 fuel elements, which corresponds to approximately 10,000 channels. This provides a high surface area for effective heat transfer to the propellant [37].

3.1.3.6 Tie Tubes

The tie tubes, which are packed along with the fuel elements into the reactor core (shown in Fig. 3.2), serve several purposes in the reactor. Tie tubes are the primary structural members in the reactor core, holding the brittle fuel elements in compression so that they do not break. Tie tubes also contain a neutron moderator, which aids in the fission chain-reaction process and helps maintain criticality in the reactor. As mentioned previously, tie tubes also act as dual-pass heat exchangers, where coolant is pumped into the central supply passage at the top of the tie tube, passes down to the closed end at the bottom, and then reverses, returning to the top of the tie tube in the annular return passage [37].

Figure 3.3 shows a cutaway view of a typical fuel element / tie tube assembly.

The ratio of tie tubes to fuel elements can vary as a design parameter for different engine sizes, but on average is equal to a little more than two fuel elements to one tie tube for a 70 kN engine. This corresponds to the basic pattern of each tie tube contacting a fuel element at each of its six faces, and each fuel element contacting three tie tubes and three other fuel elements. For larger engines, fewer tie tubes are needed to provide the necessary amount of moderator and the ratio of fuel elements to tie tubes can reach 3:1 or 6:1 [37]. As shown in Figs. 3.2 and 3.3, each tie tube is constructed of several concentric layers of material. At the center of the tie tube is a cylindrical supply channel into which the coolant (hydrogen for the propulsion-mode) enters the tie tube structure. The surface of this channel consists of an Inconel tube that is called the "inner tie tube." Moving out radially from the inner tie tube is a thick layer of zirconium hydride (ZrH) that acts as neutron moderator, slowing the neutrons generated by fission to a velocity where they are more readily absorbed by the fuel. Further out from the moderator is an annular opening for the coolant return channel. The outer wall of the return channel is another layer of Inconel - the "outer tie tube." The two Inconel tubes are the components that provide the structural support to the tie tube element. Further out from the outer tie tube is a layer of zirconium carbide (ZrC), which acts an insulator to protect the tie tubes and prevent heat loss from the fuel elements. Finally, a graphite filler layer builds the tie tube up to the hexagonal shape in order to fit properly into the reactor core.

For a BNTR, the thermal energy imparted to the tie tube coolant is used to drive the turbines of the fuel pumps in propulsion-mode and the Brayton cycle in

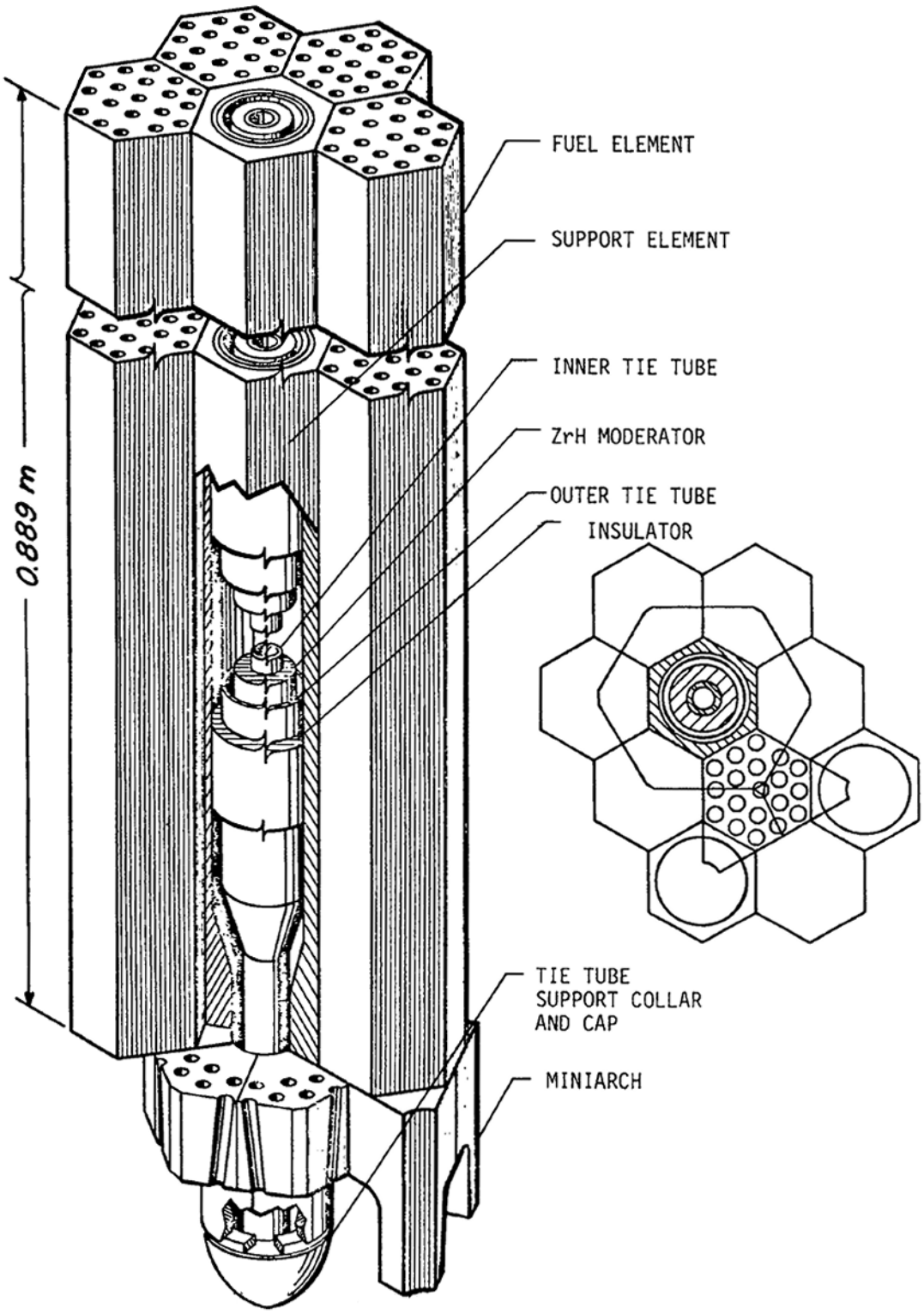

Figure 3.3: Cut-away view of a NERVA-derived fuel element / tie-tube assembly [37].

power-generation mode. The tie tube heat comes from two separate mechanisms: 1) heat conducted from the adjacent fuel elements through the outer layer of the tie tube and 2) heat generated inside of the tie tube by the neutron interaction. During propulsion-mode, the neutron flux and fuel element heat will be very high. As such, the effects of both types of heating will be significant. During power-generation mode, the neutron flux will be much lower, but the tie tubes must remove all heat generated within the reactor. As such, the heat transfer then will be dominated by conduction from the fuel elements.

3.2 Power Generation

In power generation mode, the reactor power decreases significantly from the propulsion-mode levels and the tie tubes act as the heat source for a closed-loop, recuperated Brayton cycle generator. An inert gas (He-Xe) mixture is chosen to reduce the tie tube corrosion that would occur with hydrogen. The hydrogen flow through the fuel elements is shut off completely and the He-Xe flowing through the tie tubes provides the only source of active fuel element cooling. As illustrated in Fig. 3.1, the Brayton cycle connects to the propulsion-mode only through the tie tubes. Although this connection is drawn with valves here, other types of connections may be more practical.

The power generation portion of the BNTR consists of two closed loops, as shown in the upper-right-hand portion of Fig. 3.1. The Brayton cycle operates on He-Xe working fluid and consists of the tie tubes, turbine, "gas cooler" heat

exchanger, and compressor. The turbine powers the compressor and alternator (which produces the electrical power) and a recuperator has been added to improve the cycle efficiency by pre-heating the reactor inlet flow with the turbine exhaust. The gas cooler forms the cold leg of the Brayton cycle and the hot leg of the radiator loop. The radiator loop uses a NaK liquid metal working fluid to exhaust the excess heat from the Brayton cycle to space. All waste heat from the power conversion process must be rejected through the radiator, so its size will be a primary constraint on the engine cooling capability during power generation mode.

3.2.1 Ideal Brayton Cycle Analysis

Although there are many non-ideal aspects to the recuperated Brayton cycle of a BNTR system, the analysis of an ideal Brayton cycle is the most logical point of entry to understanding these systems. An ideal non-recuperated Brayton cycle (illustrated in Fig 3.4(a)), contains of four basic processes, which have been plotted on the temperature-entropy diagram of Fig 3.4(b): 1) isentropic compression from state 1 to 2, 2) isobaric heat addition from state 2 to 3, 3) isentropic expansion from state 3 to 4, and (for a closed-loop system) 4) isobaric heat rejection from state 4 back to 1. For the Brayton cycle modeled here, these four processes occur in the compressor, tie tubes, turbine, and gas cooler, respectively. In the following section, a simple expression for the Brayton cycle efficiency will be derived, based on Ref. [86].

The performance of a Brayton cycle engine is typically characterized by the

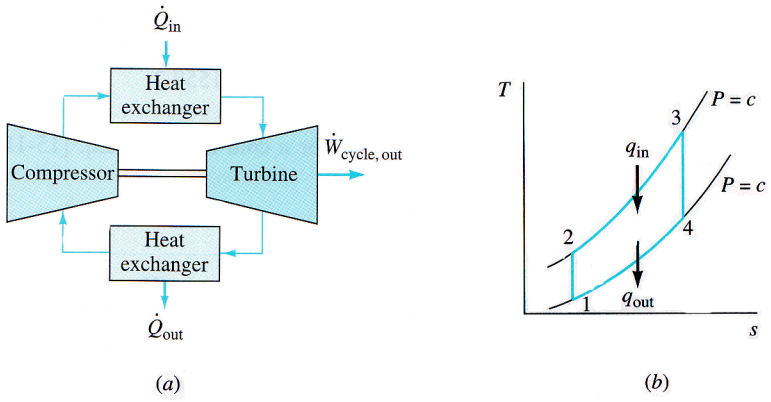

Figure 3.4: Flowpath (a) and T-s plot (b) of an ideal Brayton cycle [86].

compressor pressure ratio, which is defined as the relative pressure increase across the compressor.

$$\pi_c = \frac{p_2}{p_1} \tag{3.8}$$

The Brayton cycle thermodynamic efficiency is defined as the ratio of the excess power produced by the turbine to the heat added to the cycle from steps 2-3. By using conservation of energy to write the excess power in terms of the heat added and removed from the cycle, and then assuming a calorically perfect gas, the thermodynamic efficiency can be written in terms of the temperatures at states 1–4 in the cycle.

$$\eta_{th} = \frac{\dot{W_{out}}}{\dot{Q_{in}}} = 1 - \frac{T_4 - T_1}{T_3 - T_2} \tag{3.9}$$

The expression in Eq. 3.9 can then be simplified by first dividing the numerator by the temperature at state 1 and the denominator by the temperature at state 2.

$$\eta_{th} = 1 - \frac{T_1\,(T_4/T_1 - 1)}{T_2\,(T_3/T_2 - 1)} \tag{3.10}$$

Equation 3.10 can then be simplified by noting that the compression from 1-2 and expansion from 3-4 are isentropic processes. Thus, the temperature ratio across the compressor can be expressed in terms of the pressure ratio. Furthermore, the heat addition from 2-3 and heat removal from 4-1 occur at constant pressure, ultimately relating the turbine temperature ratio to the compressor temperature ratio, as shown in Eq. 3.11.

$$\frac{T_2}{T_1} = \frac{p_2}{p_1}^{(\gamma-1)/\gamma} = \frac{p_3}{p_4}^{(\gamma-1)/\gamma} = \frac{T_3}{T_4} \tag{3.11}$$

From Eq. 3.11, it can be concluded that $T_4/T_1 = T_3/T_2$, and Eq. 3.10 can be written solely in terms of the compressor temperature ratio, which (for isentropic compression) can then be written in terms of the pressure ratio.

$$\eta_{th} = 1 - \frac{1}{\pi_c^{(\gamma-1)/\gamma}} \tag{3.12}$$

Equation 3.12 shows the well known relation that the thermodynamic efficiency of an ideal Brayton cycle engine will increase continuously with pressure ratio. Thus the efficiency of an ideal Brayton cycle is optimized by running the highest compression ratio possible.

3.2.2 Non-Ideal Brayton Cycle Analysis

The idealized analysis presented above is not sufficient to represent the BNTR power generation because it does not account for the use of a recuperator or inefficiencies in the compressor, reactor, and turbine. This section will present the derivation of a non-ideal recuperated Brayton cycle, originally published by Zucrow in 1958 [87]. This analysis accounts for the non-ideal effects of the recuperator and

losses in the other engine components, but does not account for pressure losses in the cycle, retaining the assumption of constant pressure heat addition and removal.

In a recuperated Brayton cycle (illustrated in Fig. 3.5(a)), a heat exchanger (recuperator) is used to transfer some portion of the cycle exhaust heat to the compressor exit flow. As such, a portion of the heating from states 2-3 actually occurs in the recuperator and the required input heat to the cycle is reduced. In a similar fashion, the amount of waste heat rejected by the cycle is also reduced. If configured correctly, this results in a net increase in the cycle efficiency.

Figure 3.5(b) is a temperature-entropy diagram for the non-ideal, closed Brayton cycle system. The most notable difference between this plot and that of Fig. 3.4 is that the compressor and turbine losses create an entropy increase across the compression and expansion portions of the cycle. The recuperator is illustrated by the addition of points x and *5*, representing the exit conditions of the cold and hot legs, respectively. Note that the temperature change from *2a* to x is equal to that from *4a* to *5*, due to the heat transfer directly from one leg to the other. Figure 3.5(b) also illustrates the important point that, even for a recuperated Brayton cycle, the power extraction comes only from the turbine (between states *3* and *4a*). A much larger temperature change occurs between states *5* and *1*, which is purely waste heat that must be rejected from the radiator.

The recuperator performance is characterized by its "effectiveness", which is defined as the ratio of the actual heat transfer to the maximum possible.

$$e_R = \frac{h_{2R} - h_2}{h_4 - h_2} \tag{3.13}$$

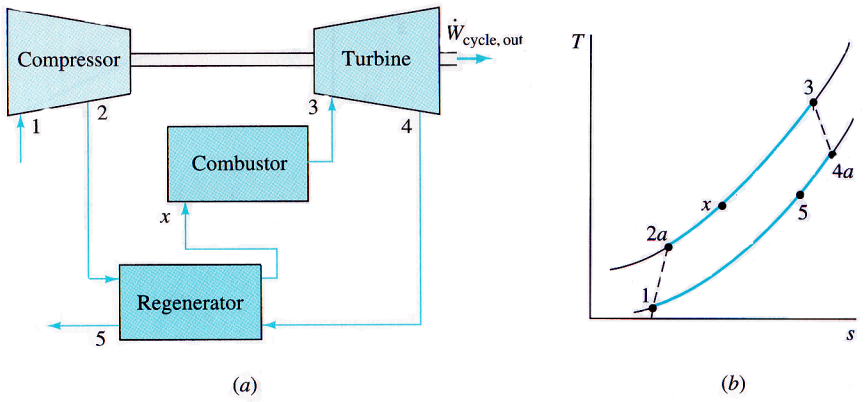

Figure 3.5: Flowpath (a) and T-s plot (b) of a non-ideal recuperated Brayton cycle [86].

The non-ideal performance of the compressor is characterized by the adiabatic efficiency, which is defined as the work required for isentropic compression divided by the actual compressor work input.

$$\eta_c = \frac{h_{2s} - h_1}{h_2 - h_1} \tag{3.14}$$

The relation in Eq. 3.14 can be simplified by assuming a calorically perfect gas to write the numerator and denominator in terms of the state temperatures, and then dividing by the compressor inlet temperature.

$$\eta_c = \frac{T_{2s}/T_1 - 1}{T_2/T_1 - 1} \tag{3.15}$$

Finally, for isentropic compression, the numerator of Eq. 3.15 can be written in terms of the compression ratio.

$$\eta_c = \frac{\pi_c^{(\gamma-1)/\gamma} - 1}{T_2/T_1 - 1} \tag{3.16}$$

A similar analysis can be performed to derive an expression for the adiabatic turbine efficiency, which is defined as the actual turbine work produced divided by

the work produced by isentropic expansion.

$$\eta_t = \frac{h_3 - h_4}{h_3 - h_{4s}} \tag{3.17}$$

For a calorically perfect gas, Eq. 3.17 can then be expressed in terms of temperature ratios in the same manner as the compressor.

$$\eta_t = \frac{1 - T_4/T_3}{1 - T_{4s}/T_3} \tag{3.18}$$

For isentropic expansion, the temperature ratio in the denominator can be related to the compressor pressure ratio in the same manner as Eq. 3.11.

$$\eta_t = \frac{1 - T_4/T_3}{1 - \pi_c^{-(\gamma-1)/\gamma}} \tag{3.19}$$

Finally, the burner (reactor) efficiency is defined as the actual enthalpy change resulting from a given input heat transfer.

$$\eta_b = \frac{\dot{m}\,(h_3 - h_{2R})}{\dot{Q}_{in}} \tag{3.20}$$

The thermodynamic efficiency of the non-ideal, recuperated Brayton cycle is also defined as the excess work out divided by the required heat in. For this cycle the excess work is best expressed as the difference between the power produced by the turbine and that required by the compressor. Using the burner efficiency of Eq. 3.20, the required heat input can be similarly expressed in terms of the enthalpy change from states 2R to 3.

$$\eta_{th} = \frac{(h_3 - h_4) - (h_2 - h_1)}{(h_3 - h_{2R})/\eta_b} \tag{3.21}$$

The definition of recuperator effectiveness in Eq. 3.13 can be used to write h_{2R} in terms of h_2 and h_4, and assuming a calorically perfect gas, all of the enthalpy terms

can be written in terms of temperature.

$$\eta_{th} = \eta_b \frac{T_3 - T_4 - T_2 + T_1}{T_3 - T_2 - e_R\left(T_4 - T_2\right)} \tag{3.22}$$

Revisiting the definitions of compressor and turbine efficiency in Eqs. 3.16 and 3.19, respectively, expressions can be derived for T_2 and T_4 in terms of T_1, T_3, π_c, and the component efficiencies.

$$T_2 = T_1 \left[1 + \frac{\pi_c^{(\gamma-1)/\gamma} - 1}{\eta_c}\right] \tag{3.23}$$

$$T_4 = T_3 \left[1 - \eta_t \left(1 - \frac{1}{\pi_c^{(\gamma-1)/\gamma}}\right)\right] \tag{3.24}$$

Finally, Eqs. 3.23 and 3.24 are simplified further by defining $\Theta = \pi_c^{(\gamma-1)/\gamma}$ and recognizing that both equations contain the ideal Brayton cycle efficiency from Eq. 3.12, which will be called η_a here.

$$T_2 = T_1 \left(1 + \frac{\Theta}{\eta_c}\frac{\Theta - 1}{\Theta}\right) = T_1 \left(1 + \frac{\Theta \eta_a}{\eta_c}\right) \tag{3.25}$$

$$T_4 = T_3 \left[1 - \eta_t \left(1 - \frac{1}{\Theta}\right)\right] = T_3 \left(1 - \eta_t \eta_a\right) \tag{3.26}$$

Equation 3.22 can be written entirely in terms of T_3, T_1, and the component properties by combining it with the results of Eq. 3.25 and 3.26.

$$\eta_{th} = \eta_b \frac{T_3 - T_3\left(1 - \eta_t\eta_a\right) - T_1\left(1 + \frac{\Theta\eta_a}{\eta_c}\right) + T_1}{T_3 - T_1\left(1 + \frac{\Theta\eta_a}{\eta_c}\right) - e_R\left(T_3\left(1 - \eta_t\eta_a\right) - T_1\left(1 + \frac{\Theta\eta_a}{\eta_c}\right)\right)} \tag{3.27}$$

A simpler form can then be derived by dividing the numerator and denominator by T_1 and defining the cycle temperature ratio $\alpha = T_3/T_1$.

$$\eta_{th} = \eta_b \frac{T_1\left(\alpha\eta_t\eta_a - \frac{\Theta\eta_a}{\eta_c}\right)}{T_1\left[\alpha - \left(1 + \frac{\Theta\eta_a}{\eta_c}\right) - e_R\left(\alpha\left(1 - \eta_t\eta_a\right) - \left(1 + \frac{\Theta\eta_a}{\eta_c}\right)\right)\right]} \tag{3.28}$$

A final form of the non-ideal, recuperated Brayton cycle efficiency is derived by rearranging the numerator and denominator, resulting in an equation composed entirely of non-dimensional parameters that characterize the operation of the cycle and its components.

$$\eta_{th} = \eta_a \eta_b \frac{\alpha \eta_t - \frac{\Theta}{\eta_c}}{\alpha \left(1 - e_R \left(1 - \eta_t \eta_a\right)\right) - \left(1 - e_R\right) \left(1 + \frac{\Theta \eta_a}{\eta_c}\right)} \tag{3.29}$$

As shown in Eq. 3.29, the non-ideal, recuperated Brayton cycle efficiency is equal to the ideal Brayton cycle efficiency multiplied times the burner efficiency and a correcting factor of sorts that account for inefficiencies in the turbomachinery and the effects of recuperation. From an examination of the numerator, it is clear that increasing the compressor and turbine efficiency will improve the cycle efficiency. The purpose of recuperation, of course, is to improve cycle efficiency, but its theoretical impact is best understood by plotting Eq. 3.29 for several input cases.

Figure 3.6 illustrates the impact of turbomachinery efficiency, recuperator effectiveness, compressor pressure ratio, and cycle temperature ratio on the Brayton cycle efficiency. The top row of subplots all assume compressor and turbine efficiencies of 80% and 85%, respectively, while the bottom row of subplots assume 100% efficiency. The three columns examine the impact of recuperator effectiveness, with values from left to right of 0.9, 0.5, and 0.0. The burner/reactor is assumed to operate with 100% efficiency. As such, the far right column shows the efficiency of a non-recuperated Brayton cycle, and the lower-right subplot shows the efficiency of an ideal Brayton cycle.

The most striking conclusion from Fig. 3.6 is that maximizing pressure ratio

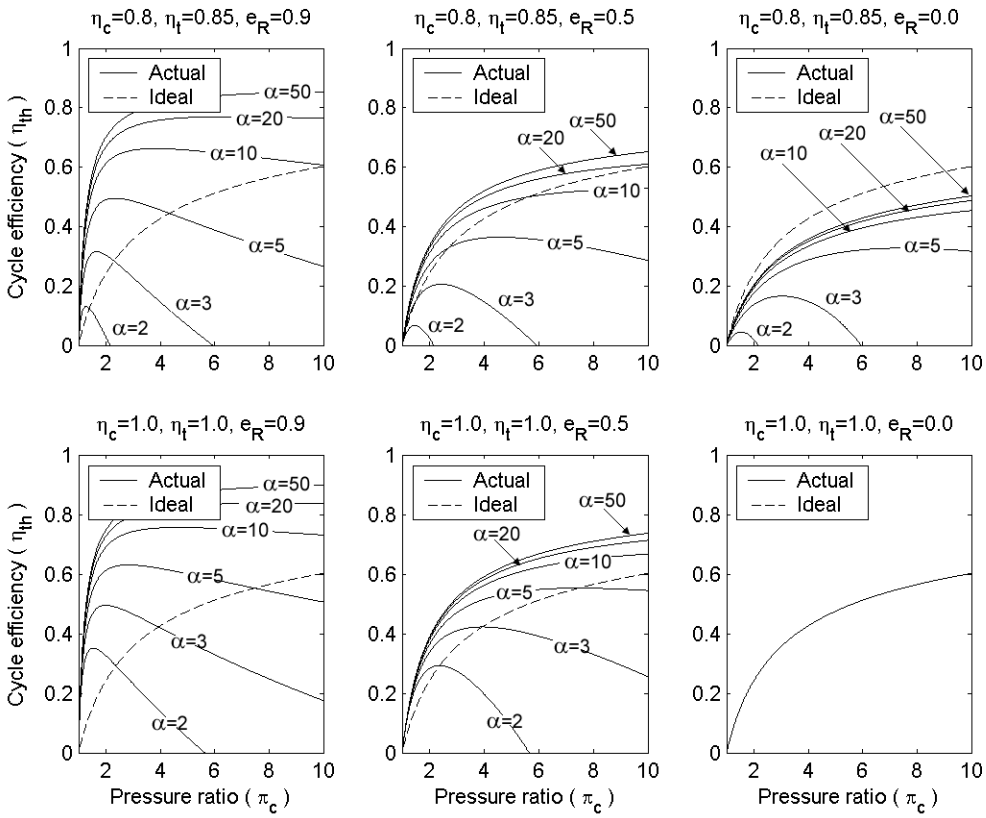

Figure 3.6: Cycle efficiency of a non-ideal Brayton cycle.

does not always maximize the efficiency of a non-ideal Brayton cycle. In fact, for many cases, there is a finite value of pressure ratio that produces maximum specific impulse. This may seem counter-intuitive for those more familiar with Brayton cycle engines as a form of propulsion, but is a common occurrence for Brayton cycle power systems. In general, the combination of a low cycle temperature ratio (α) and non-ideal operation in any other component will create a local optimum pressure ratio. As α increases, however, the optimum pressure increases towards infinity. This trend is only absent for the case of an ideal, non-recuperated Brayton cycle, where Eq. 3.29 collapses to the ideal efficiency of Eq. 3.12.

Figure 3.6 also illustrates the benefit of recuperation in a Brayton cycle. The addition of recuperation allows a non-ideal Brayton cycle to operate at a higher efficiency than an ideal, non-recuperated cycle. Holding all else the same, increasing the recuperator effectiveness increases the cycle efficiency of a particular design and drives the optimum pressure ratio towards a value of 1.0.

Chapter 4

Engine Modeling

The modeling for this project has been completed in several stages, using pre-existing codes when possible and adding detail and capability when needed. This process began with the correction and updating of a pre-existing NTR model from NASA Glenn. In order to add the flexibility required for BNTR operation to that model, an entirely new tie tube component model was created. Lastly, a pre-existing Brayton cycle power generation model was modified and combined with the NTR model in order to produce an integrated BNTR system model. This chapter presents the details of these models, beginning with a brief discussion of the pre-existing codes, followed by a detailed description of the BNTR model in its final form.

4.1 Pre-Existing Codes and Models

As nuclear propulsion and power systems have been studied for many decades, several codes for modeling them already exist. This project has reused older codes whenever possible, building off of the work already completed by others. The following section briefly describes NTR and Brayton cycle power system models that

have already been developed, and their limitations for BNTR use.

4.1.1 Nuclear Engine System Simulation (NESS)

NASA's Nuclear Engine System Simulation (NESS) is a FORTRAN-based NTR model that was developed in the early 1990's for SEI and remains the standard NTR modeling code at NASA Glenn Research Center. Portions of the code, primarily the reactor data and analysis, were originally developed by Westinghouse during the NERVA program. NESS is designed to model a NERVA-era expander-cycle NTR, and includes a 1-D analysis of the propellant thermodynamics and heat transfer inside the fuel elements. NESS also includes detailed weight calculations for the entire engine system to aid in vehicle design and integration [43].

The analysis in NESS relies on several empirical parameters and equations from Westinghouse's original NERVA reactor component fabrication and testing. Some of these fixed parameters include the heat addition per fuel element, heat absorption per tie tube, and tie tube pressure drop. Additionally, the relative coolant mass flow rates through the nozzle cooling jacket and tie tubes are user-specified in NESS. These fixed parameters limit the flexibility of this model, precluding the ability to model BNTR operation [43].

4.1.2 NPSS-Based Expander-Cycle NTR

Shortly before this project began, an expander-cycle NTR model was created at NASA Glenn Research Center. This model was a rough translation of the NESS

dual-turbopump engine into NPSS. A component model had been created based on the NESS 1-D fuel element analysis, but its use in the NTR model caused several problems that prevented convergence. As such, the engine model was being run with a basic 0-D fixed heat addition fuel element component. All non-nuclear components were based on standard NPSS models and did not carry over the analysis from NESS. The NPSS-based reactor analysis retained most of the empirical parameters from NESS and its inability to represent BNTR engines. This model, however, allowed NPSS to solve for the mass flow rates throughout the engine directly, adding some flexibility.

4.1.3 Closed Cycle System Simulation (CCSS)

NASA's Closed-Cycle System Simulation (CCSS) is a mature, NPSS-based model of a nuclear-heated closed Brayton cycle power generation system. CCSS was originally developed in cooperation with the U.S. Navy for the Jupiter Icy Moons Orbiter (JIMO) mission [85]. The Navy retained the nuclear portion of the model, so CCSS contains detailed component models of the turbomachinery and heat exchangers, but a 0-D reactor heat source mode with an assumed pressure drop and exit temperature [85, 83]. As discussed in Chapter 2, CCSS has been validated experimentally for both steady-state and transient operation. The primary limitation of CCSS for BNTR operation is that the 0-D heat source model may not correspond very closely to the operation of a NERVA reactor.

4.2 Numerical Propulsion System Simulation (NPSS)

Although not an engine model itself, NASA's Numerical Propulsion System Simulation (NPSS) is an industry-standard propulsion modeling framework that is used for all modeling in this dissertation. To familiarize the reader with how the BNTR model has been created and executed, a cursory overview of the structure of NPSS models and how they are run is presented in this section. Full details of NPSS operation and usage may be found in the NPSS documentation [88].

NPSS is a modular, object-oriented code, which allows for easy updating and interchanging of component models without having to change the overall engine model. NPSS has a library of stock models for standard components such as pumps, turbines, pipes, and nozzles. User-defined components of varying fidelity may also be created. Several thermodynamic packages have been integrated into NPSS, reducing the amount of programming required for new component and engine models. These packages can range from simple user-defined lookup tables to NASA's Chemical Equilibrium with Applications (CEA) code. Finally, NPSS contains a built in solver that balances the engine model, ultimately producing results that more accurately portray the performance of an actual engine [88]. As such, NPSS is often referred to as a "virtual engine test cell" [89].

NPSS treats each engine component as an individual object with its own component-specific properties and algorithms and allows the user to link these components together to create an engine model. Engine components are connected through objects called "ports." The three types of most commonly used ports are

fluid ports, thermal ports, and shaft ports. Fluid ports communicate the thermodynamic state properties of a fluid between two components. Thermal ports communicate heat transfer rates. Shaft ports communicate the torque and rate of rotation from turbomachinery to an attached shaft. The process of building an engine by connecting component ports in the proper order is called "linking." Links may be created and broken through a series of NPSS commands, automating the process of creating and modifying an engine model. In doing so, models may be created, run, and modified automatically based on the programming of the model run file. The flexibility of dynamically modifying models gives NPSS the capability to model a BNTR engine system.

The built-in NPSS solver is designed to generate a balanced engine solution by varying a set of default and user-defined independent variables until a similar set of dependent conditions is satisfied. For a non-linear, closed-cycle engine like a rocket, the solver incorporates NASA's "Rocket Engine Transient Simulation" (ROCETS). In general, the independent properties for these components are temperature, pressure, and mass flow rate. The dependent conditions ensure that conservation of mass, momentum, and energy are satisfied throughout the engine [88].

Engine models are created and run in NPSS through a series of interpreted files that contain programming code that defines the components and the overall model. NPSS does not require a rigid structure for file naming and usage, but a general protocol has been followed for this project as described in this paragraph. At the lowest level are component model files, which use the extension ".int" (*e.g.* Pump.int, Shaft.int). The component files contain a definition of the default ports,

solver variables, and the engineering calculations used to simulate the component performance. The next-highest type of file is the engine model file, which typically uses the extension ".mdl" (*e.g.* NTR.mdl, Brayton.mdl). The engine model file defines the components to use and links them in their proper order. Finally, the run file (extension: ".run") is used to control the entire process. The run file calls the engine model, sets up the solver sequence and design point parameters, runs the model, and controls the screen and file output. This arrangement allows the component files to be completely modular for use in a variety of engine models. The engine models then only define the engine configuration and basic solver setup, while the design-point specific data (which is modified most often) is contained only in the highest level of file. Figure 4.1 illustrates this hierarchy for the BNTR model created in this project.

4.3 New BNTR Model

The BNTR model has been created by modifying and combining portions of the various codes and models discussed above. All modeling is done in the NPSS environment. The NESS-derived expander-cycle NTR model is the basis of the propulsion mode model while CCSS is the basis of the power generation mode. A new, top-level BNTR model has been created in order to combine both modes into a single engine model such that the NTR-based reactor design can be easily communicated to the Brayton cycle analysis. The current model does not include feedback from the power cycle to update the reactor design, but the environment

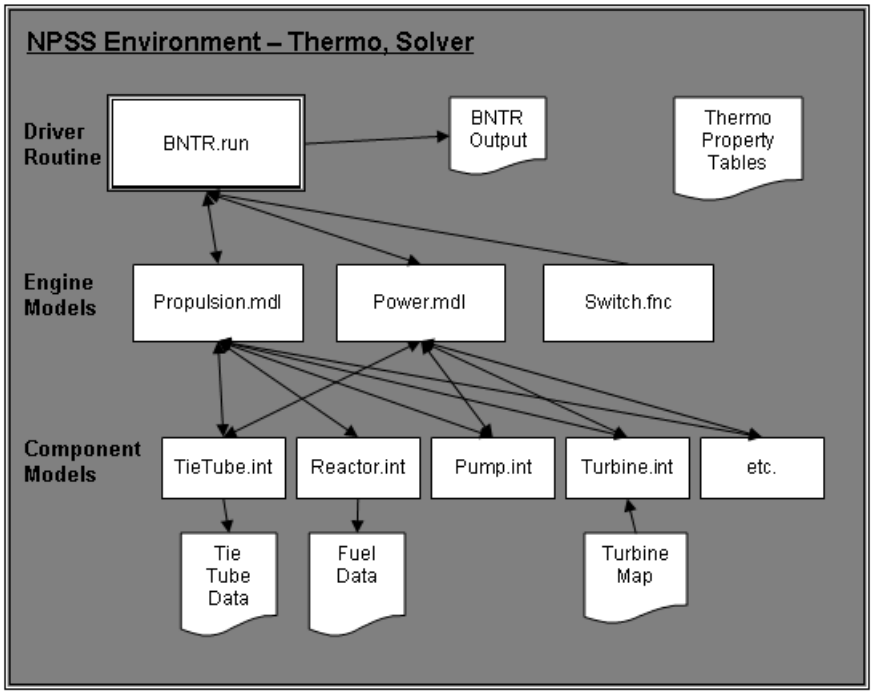

Figure 4.1: Flowchart of BNTR model operation.

has been created in such a manner this could be added on at a later date.

4.3.1 Operation

The file "BNTR.run" is used to control the entire BNTR model in NPSS. This file loads, links, and executes the two engine modes in sequence. It relies on a series of support functions contained within the file "BNTR_Switch.fnc." The actual propulsion model definition is contained within the file "BNTR_Propulsion.mdl." The propulsion model links to the appropriate component models, initializes each component in the solver, and defines any additional solver conditions for each component. Then, back in the run file, a function is called to link the propulsion components together in the solver, and then the engine model is run.

After the propulsion model has converged, the design reactor length and number of tie tubes are stored in global variables so that they may be passed on to the power-generation model. Then the solver is cleared, and the propulsion components are unlinked and removed from the workspace (the actual files remain untouched).

The power generation model is loaded from the file "BNTR_Power.mdl," which defines and loads the power-generation cycle components. During power-mode initialization, the tie tube component model has been specifically designed to set the reactor length and number of tie tubes from the global variables discussed above. Finally, the same procedure is carried out for linking and running the power generation model.

This entire process is performed automatically by the NPSS code, using a run file that was created specifically for this dissertation research. Different design points and trade studies are performed by changing the solver variables to match desired design values for thrust, chamber temperature, reactor length, etc. With this structure, the component models define only the most general physical operation of that component. The engine model files similarly contain only the physical layout of the flowpath. All design point and case study-specific data is contained in the run file. As such, users of this model need only work with a single file in order to perform most propulsion, power, and bimodal modeling studies.

4.3.2 Propulsion-Mode Model

4.3.2.1 Modifications to NESS-Based Model

As discussed in the previous chapter, the pre-existing NESS-based model had three major limitations: 1) it could not converge when the 1-D reactor component was used, 2) the accuracy of the calculations in that component and of the overall engine layout was questionable, and 3) it still relied on empirical parameters based on a high-thrust NERVA engine. In order to use this model, the reactor analysis and engine layout had to be re-derived. The details of the reactor analysis will be discussed in Chapter 5. The proper expander-cycle NTR configuration and the components used to model it are presented below.

An expander-cycle NTR model has been created in NPSS, using the same engine configuration and fundamental reactor analysis from NESS. The reactor fuel element analysis has been modified with modern heat deposition data and a more efficient update scheme. A new component model has also been created for the reactor tie tubes. The original tie tube analysis in NESS consists of an assumed pressure drop and heat addition to the coolant. The new tie tube model calculates the 1-D analysis of heat addition and friction in the dual-pass coolant channels, as well as radial thermal conduction with heat generation through the tie tube walls. This allows the direct calculation of the pressure drop across these elements in both propulsion and power generation modes.

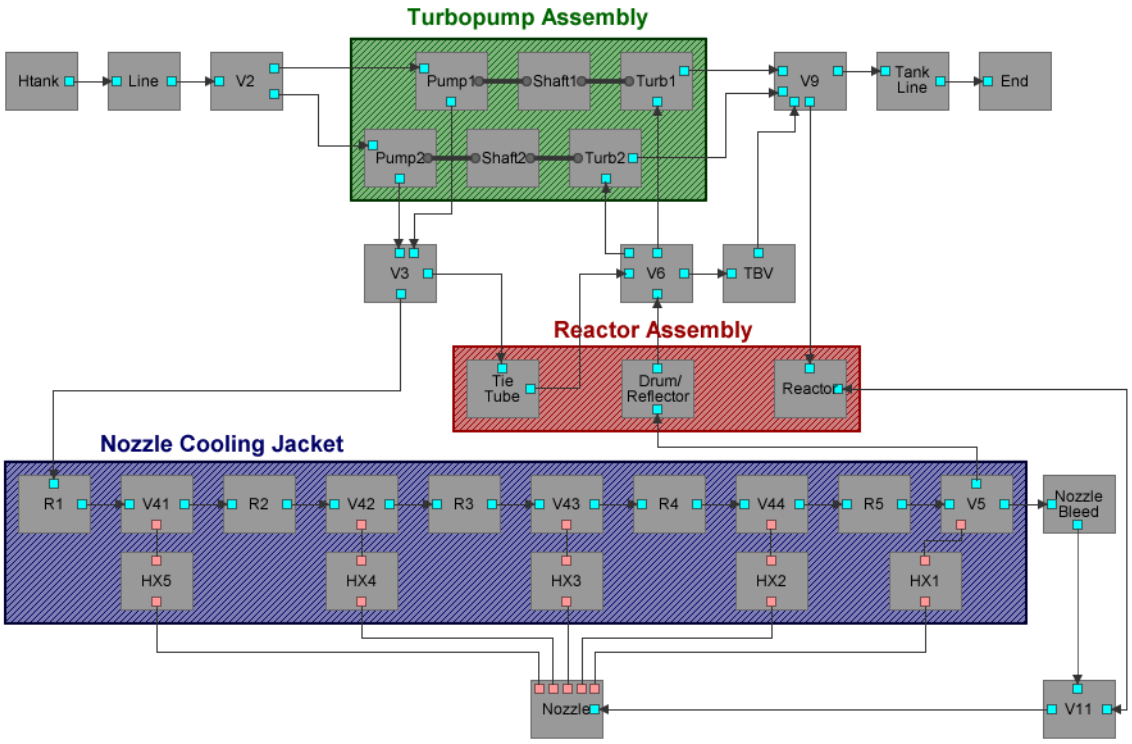

Figure 4.2: Block diagram of BNTR propulsion-mode engine model in NPSS.

4.3.2.2 Component Details

This section lists each NPSS component used by the propulsion model, in their execution order, along with a basic summary of the analysis performed by that component. The heading for each paragraph is the name of the component as shown in Fig. 4.2, followed in parenthesis by the NPSS component class used to model it.

Htank (Starter)

Htank is an NPSS "Starter" component that simply represents the thermodynamic state of the store liquid hydrogen propellant. It requires values for temperature and pressure to define the thermodynamics state, and uses the NPSS thermodynamic package to calculate any other properties that may be required.

Line (ResistanceInert)

This component connects the tank to the fuel pump(s) and represents the master shutoff valve in the engine. "ResistanceInert" is the simplest form of modeling a duct in NPSS; it simply assigns a design flow rate to either end of the pipe and assigns the value of flow enthalpy at the inlet of the pipe to the exit. This element also calculates the flow resistance based on the density and pressure at either end of the pipe (shown in Eq. 4.1), but this property is only used for transient analysis.

$$\mathcal{R} = \frac{\bar{\rho}\,\Delta p}{\dot{m}^2} \tag{4.1}$$

V2 (CoolingVolume)

This component divides the hydrogen propellant from the tank between the two fuel pumps. It uses a important type of NPSS component class, called a "CoolingVolume." CoolingVolumes are used whenever streams join or split within an engine and can have any number of input and output flow ports. In this case, V2 has one input port (coming from "Line") and either one or two output ports depending on the whether the engine uses a single- or dual-turbopump setup. For the case of a single-turbopump engine, this component is unnecessary, but is present to retain flexibility in the model.

A CoolingVolume essentially performs a simple bookkeeping analysis to assure that mass and energy are conserved across the junction of the connected ports. This is done by varying the enthalpy and pressure at the node until the total mass and energy into and out of the element are equal, as shown in Eqs. 4.2 and 4.3.

$$\sum \dot{m}_{in} = \sum \dot{m}_{out} \tag{4.2}$$

$$\sum \dot{m}_{in} h_{in} = \sum \dot{m}_{out} h_{out} \tag{4.3}$$

The conservation equations are predominately affected by the flow rates into and out of the element — values which are varied globally in the engine model. For a rocket analysis, CoolingVolume components also require an initial estimate of the local temperature and pressure.

Pump1, Pump2 (PumpJLF)

The pump component(s) are modeled by the NPSS component class "PumpJLF," which is a version of NPSS's standard pump model that had been modified by Jim

Fittje of NASA Glenn for the original NESS-based NTR model. The modifications allow this component to model a turbopump without using a performance map. Instead, the pump head and shaft torque a varied independently to match user-defined values for pump efficiency and exit pressure.

Pump head is defined as the pressure change divided by density, so the pump exit pressure can be calculated in terms of the given head and inlet density, as shown in Eq. 4.4.

$$p_{out} = h_p \rho_{in} + p_{in} \tag{4.4}$$

The enthalpy change across the pump is calculated in terms of the given torque, shaft speed, and flow rate. The pump efficiency is then defined as the pump head divided by the enthalpy change. These relations are shown in Eqs. 4.5 and 4.6.

$$\Delta h = \frac{2\pi\tau N_{shaft}}{60\dot{m}} \tag{4.5}$$

$$\eta_p = \frac{h_p}{\Delta h} \tag{4.6}$$

As stated above, the Pump solver is arranged to vary the head and torque until the calculated pump exit pressure and efficiency match design values input by the user.

V3 (CoolingVolume)

V3 is another CoolingVolume component that splits the combined pump exit flow between the tie tubes and the nozzle cooling jacket.

TieTube (TieTube)

The "TieTube" is one of the components that has been created specifically to model a NERVA-derived engine. It uses a 1-D analysis to calculate the temperature

and pressure change caused by the heat addition and friction in tie tube components. The original NESS-based NTR model used a resistance element with fixed heat addition and pressure drop to model the tie tubes. That analysis has been replaced with the direct calculation of the pressure drop from a 1-D analysis of the coolant thermodynamics and radial thermal conduction with heat generation through the tie tube walls. The TieTube component model and analysis is one of the main deliverables of this project and, as such, the details of its analysis will be presented separately in Chapter 5.

V6 (CoolingVolume)

V6 is another CoolingVolume that joins the tie tube and reflector coolant streams and splits them between the turbine(s) and the turbine bypass valve. Some proposed NTR engines are designed such that only the tie tubes or only the reflector provide the turbine drive gas. This model is designed such that both streams combine and provide as much turbine flow as required. Excess gas can bypasses the turbine to enter the reactor directly.

TBV (ResistanceInert)

TBV is a resistance element that models the turbine bypass valve. As explained above, this component aids in the turbopump balancing by allowing some portion of the combined tie tube and reflector exhaust to bypass the turbine entirely.

Turbine1, Turbine2 (Turb02)

In a similar manner to the pump model, "Turb02" models the turbine(s) through direct performance calculations without a map. The output power and torque are calculated based on the given shaft speed, efficiency, and input conditions. The flowrate, in turn, is an independent parameter that is varied by the solver in order to balance the pump and turbine.

The turbine inlet and exit pressures are assigned as the engine level. The required power is determined by first calculating the enthalpy change for isentropic expansion. The isentropic exit enthalpy is found by combining the inlet entropy and exit pressure in the NPSS thermodynamics package. The actual enthalpy change (and thus power requirement) is calculated by multiplying the isentropic enthalpy change by the given turbine efficiency and flow rate, as shown in Eq. 4.7. Torque is calculated by dividing the shaft power by the given shaft speed, as in Eq. 4.8.

$$\dot{W}_t = \dot{m}\ \eta_t \left(h_{in} - h_{out,s}\right) \tag{4.7}$$

$$\tau = \frac{60\ \dot{W}_t}{2\pi N_{shaft}} \tag{4.8}$$

V9 (CoolingVolume)

V9 joins the turbine(s) with the turbine bypass flow, and directs that flow primarily to the reactor, with a small amount bled off for tank pressurization.

TankLine (ResistanceInert)

TankLine represents the bleed line that carries a small portion of the turbine exhaust back to the fuel tank for tank pressurization. This line has a fixed flow rate

of 0.04 kg/s, which will be evident as a loss between the flow leaving the tank and entering the chamber in all of the results from this model.

E1 (Ender)

E1 is a bookkeeping component that simply terminates the tank pressurization fluid stream.

R1–R5 (ResistanceInert)

Component R1–R5 represent the flow resistance encountered in the pipes of the nozzle cooling jacket. The cooling jacket is split into five segments to account for variations in the nozzle wall temperature.

V41–V5 (CoolingVolume)

In addition to combining flow streams of varying thermodynamic properties, CoolingVolume components are also a means of adding thermal energy directly to a flow. These elements use that functionality to perform the actual heat transfer in the nozzle cooling jacket. Each CoolingVolume (V41–V5) is connected to a section of the nozzle wall by a thermal port. The order of the volumes is arranged such that V41 is thermally connected to the bottom-most cooled portion of the cooling jacket and V5 is connected to the throat.

ControlDrum (ResistanceInertQ)

Despite its name, the ControlDrum component represents the control drum *and* reflector cooling flow. The component type ResistanceInertQ operates in the same manner as the ResistanceInert duct model, with the addition of a user speci-

fied heat addition (Q). In this case, the heat addition from the control drums and reflectors is calculated from the empirical assumption that approximately 0.8% of the total reactor power is transferred into the control drum and reflector coolant. The only difference between this component and the ResistanceInert is that that the specific heat addition, "q," is added to the enthalpy at the component exit, as shown in Eq. 4.9.

$$h_{out} = h_{in} + \frac{\dot{Q}_{in}}{\dot{m}} \tag{4.9}$$

Reactor (NTR)

The Reactor component is the other entirely custom component created for this model. While named "Reactor," this component actually performs the heat transfer and thermodynamics analysis for the fuel elements and the hydrogen propellant. A 1-D analysis is employed in the same manner as the tie tube model. The benefits of the 1-D analysis here are having the ability to calculate the required reactor inlet pressure for a given chamber pressure as well as calculating the peak internal fuel temperature. The detailed analysis for this component is also presented in Chapter 5.

NozzleBleed (ResistanceInert)

This is another simple duct component that allows for some amount of bleed flow from the exit of the nozzle cooling jacket into the nozzle wall. This flow is used for film cooling at the wall, but is not generally required for the NTR engine. As such, it has a low target flow rate of 0.08 kg/s.

V11 (CoolingVolumeCEA)

The component V11 represents the chamber of the rocket. It combines the reactor exhaust and nozzle bleed flow from the cooling jacket, and sends them to the nozzle. The component type "CoolingVolumeCEA" works in the same manner as a standard CoolingVolume, except that it specifically uses NASA's Chemical Equilibrium with Applications (CEA) code to calculate the thermodynamics. CEA generally handles high temperatures better than the other packages, so it is used for the hot sections of the engine.

Nozzle (RocketNozzleCEA)

The nozzle is one of the most complex components in the NTR engine model, because it has to account for not only the expansion of the engine propellant but also the heat transfer from the nozzle wall to the cooling jacket. The primary purpose of the nozzle is to calculate the exit velocity and exit pressure of an isentropic nozzle with given chamber conditions, throat area, and area ratio.

The thrust equation is then used to calculate thrust and specific impulse, as shown in Eqs. 4.10 and 4.11. As in the chamber analysis, CEA thermodynamics are used for the high temperature propellant.

$$T = \dot{m} u_e + p_e A_e \tag{4.10}$$

$$I_{sp} = \frac{T}{g\,\dot{m}} \tag{4.11}$$

The nozzle exit velocity is calculated from the conservation of energy across the nozzle, which (assuming zero velocity in the chamber and ideal expansion) can

be written in terms of the difference between the total and static enthalpies at the engine exit, as in Eq. 4.12.

$$u_e = \sqrt{2\left(h_{e,t} - h_e\right)} \tag{4.12}$$

The total enthalpy at the exit comes from assuming isentropic flow to setting the exit total thermodynamic conditions equal to the nozzle inlet conditions. The only additional property required for the NPSS thermodynamics package to determine the static conditions is the nozzle exit area, which is determined from the given throat area and area ratio, as shown in Eq. 4.13.

$$A_e = A_{th} AR \tag{4.13}$$

The hot side of the cooling jacket analysis is based on a model of the RL10A created by Binder, Tomsik, and Veres at NASA Glenn Research Center in 1997 [90]. The full details of this analysis can be found in Ref. [90], but the general procedure will be summarized here. The cooled section of the nozzle is divided into five equally spaced segments of constant radius and wall temperature. Each of these segments is independently connected to a wall component by a thermal port, which communicates heat transfer rate and wall temperature between the wall and nozzle propellant. The average propellant, film, and adiabatic wall temperatures are calculated based on the ideal expansion from the throat to the local area of that segment. Finally, the convective heat transfer into the wall is calculated using the Bartz equation approximation for heat transfer coefficient.

HX1-HX5 (Wall2)

The final component of the nozzle cooling jacket is a model of the nozzle wall itself. As in the other components in the cooling jacket, there are five wall elements, numbered HX1–HX5. For steady-state operation, the "Wall2" component varies the nozzle wall material temperature until the net heat transfer rate across the element is zero. This is represented by the simply balance shown in Eq. 4.14. The actual heat transfer is handled by the thermal ports that connect the wall to the nozzle at the hot side and cooling jacket at the cold.

$$\sum Q_{in} = \sum Q_{out} \tag{4.14}$$

Shaft1, Shaft2 (Shaft)

The shaft component(s) provide a mechanical connection between the pump(s) and turbine(s). They connect in NPSS through special shaft ports that communicate the torque and rotating speed. For the current model, shaft speed is a fixed input parameter, so the shaft component performs a turbopump power balance by ensuring that the net torque is equal to zero, as shown in Eq. 4.15

$$\tau_t - \tau_c = 0 \tag{4.15}$$

4.3.3 Power-Mode Model

The BNTR engine model has been created by combining CCSS with the propulsion model discussed above and replacing the 0-D heat source with the tie tube component model. The final model employs a two-stage analysis process: 1)

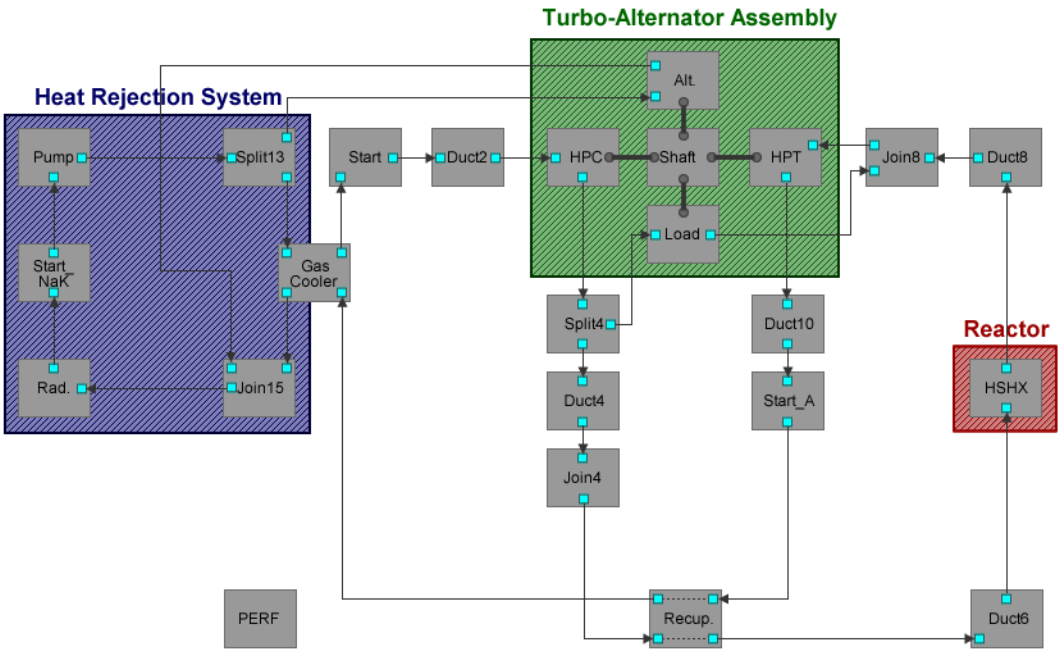

Figure 4.3: Block diagram of BNTR propulsion-mode engine model in NPSS.

the reactor is sized for propulsion operation based on user-specified thrust and chamber temperature requirements, 2) the propulsion-sized reactor is then used as the heat source for the Brayton cycle, determining the required reactor power input to produce a user-specified electric power. This process is performed automatically in a single NPSS model, which can then be used to verify the feasibility of proposed BNTR designs and perform trade studies on the engine-level impact of various design parameters such as engine thrust, chamber temperature, reactor temperature limits, Brayton cycle pressure ratio, etc.

4.3.3.1 Component Details

The power-generation model is based directly on CCSS, with the TieTube component acting as the heat source. With the exception of the tie tube model, all

other components are pre-existing and are being used in their default form. This section will present a brief overview of these components and their analyses. Details of the original CCEP model that CCSS is based upon can be found in Ref. [91]. As in the propulsion model description, the heading for each paragraph is the name of the component as shown in Fig. 4.3, followed in parenthesis by the NPSS component class used to model it.

Start (HeXeStart)

The Start component sets the compressor inlet flow properties for the Helium-Xenon (He-Xe) loop. In the Brayton cycle model, this component actually acts as both the flow starter and ender in order to form a closed loop. The "HeXeStart" accomplishes this by setting dependent conditions that the temperature, pressure, and flow rate at the inlet port must equal those properties at the outlet port. For this model, the temperature and pressure at this location are actually design parameters, while the flow rate (which controls the flow rate through the entire Brayton cycle) is varied as an independent.

Duct2 (GDuct)

Duct2 represents the duct that connects to cold-side heat exchanger to the compressor. The "GDuct" component is based on the duct analysis from CCEP, and calculates the pressure drop based on wall friction and number of bends (N_{bends}) in the duct. The coefficient of friction for the wall comes from a correlation based on Reynolds number, as shown in Eq. 4.16.

$$f_{wall} = [0.79 \ln (Re) - 1.64]^{-2} \tag{4.16}$$

The friction due to bends is assumed to be 0.19 times the number of 90-degree bends in the duct, as shown in Eq. 4.17.

$$f_{bends} = 0.19 N_{bends} \tag{4.17}$$

Finally, the duct exit pressure (as shown in Eq. 4.18) is calculated as the inlet pressure minus the total friction times the average dynamic pressure.

$$p_2 = p_1 - 0.5 \left(f_{wall} + f_{bends} \right) \overline{(\rho u)}^2 \tag{4.18}$$

As this model is for a hypothetical system, a representative geometry from the original CCSS model is used. In this case, Duct2 is specified as being 36 in. (0.91 m) long, with one 90 degree bend. The NPSS solver is then set up to vary the duct diameter to produce a 2% pressure drop across the duct.

HPC (Compressor_x)

The Brayton cycle compressor model calculates the exit gas properties and the shaft power and torque required to satisfy user specified pressure ratio and efficiency. Although NPSS has its own compressor component models, this particular model is based on the original CCEP high pressure compressor (HPC). The CCEP model originally calculated corrected flow, pressure ratio, and efficiency based on inlet corrected shaft speed from a generic compressor map. Through early use of this model, however, it was found that the BNTR power cycle required pressure ratios that extrapolated the map to unrealistically low component efficiencies. As such, the component model was changed to calculate the exit gas properties and required shaft torque and power directly.

The exit properties are calculated by applying the given pressure ratio and efficiency to the given inlet conditions. The exit pressure is simply equal to the inlet pressure times the pressure ratio, as in Eq. 4.19. The ideal exit temperature is then calculated from the isentropic relation of pressure ratio to temperature ratio shown in Eq. 4.20.

$$p_2 = p_1 \pi_c \tag{4.19}$$

$$T_{2s} = T_1 \pi_c^{(\gamma-1)/\gamma} \tag{4.20}$$

The NPSS thermodynamics package is used to automatically calculate all remaining thermodynamic state properties for the exit of an ideal compressor. From that, the actual enthalpy change (Eq. 4.21) can be calculated as the ideal (isentropic) enthalpy change divided by the compressor efficiency.

$$\Delta h = \frac{h_{2i} - h_1}{\eta_c} \tag{4.21}$$

The actual compressor exit properties are then set by the NPSS thermodynamics package based on the exit enthalpy and pressure. Finally, the required shaft power and torque can be calculated from the enthalpy change, as shown in Eqs. 4.22 and 4.23, respectively.

$$\dot{W}_c = \dot{m}\ \Delta h \tag{4.22}$$

$$\tau = \frac{60\ \dot{W}_c}{2\pi N_{shaft}} \tag{4.23}$$

Split4 (Splitter_x)

Split4 accounts for bleed flow after the compressor exit that is used for gas bearing lubrication and shaft and alternator cooling. This is represented in the

model by flow into the "Load" component only. "Splitter_x" is based on the NPSS "Splitter" component, which handles this process by splitting one entering stream into exit streams and applying separate pressure losses to each stream. This component had been modified for CCSS by setting the split bypass ratio directly and assuming zero pressure loss in both the primary and secondary exit streams.

The splitter bypass ratio (β_{split}) is defined as the ratio of the secondary to primary stream flow rates. The power system model, however, defines the bleed in terms of a bleed fraction (f_{bleed}), which is the ratio of bleed to inlet flow. The bypass ratio can be calculated in terms of bleed fraction as shown in Eq. 4.24.

$$\beta_{split} = \frac{f_{bleed}}{1 - f_{bleed}} \tag{4.24}$$

The primary and secondary flow rates are then calculated in terms of the known inlet flow and bypass ratio, as shown in Eqs. 4.25 and 4.26, respectively.

$$\dot{m}_{pri} = \frac{\dot{m}_{in}}{1 + \beta_{split}} \tag{4.25}$$

$$\dot{m}_{sec} = \dot{m}_{in} - \dot{m}_{pri} \tag{4.26}$$

Duct4 (GDuct)

Duct4 is another "GDuct" component that represents the connection between the compressor and the inlet of the cold leg of the recuperator. This duct is assumed to be 50 in. (1.3 m) long, with one 90 degree bend, and also varies the diameter to produce a 0.2% pressure drop.

Load (CCEPLoad)

The Load component uses another model that comes directly from CCEP. It calculates the bearing losses in the turbo-alternator system based on an empirical relation. The relation requires knowledge of the "cavity" thermodynamic properties, which are the gas properties around the shaft. The cavity pressure (p_{cav}) is defined in terms of the compressor inlet and exit pressures as shown in Eq. 4.27.

$$p_{cav} = p_{c,in} + 0.2\,(p_{c,out} - p_{c,in}) \tag{4.27}$$

The cavity temperature (T_{cav}) is assumed to be the temperature corresponding to the Load cooling flow, after it has absorbed the bearing, windage, and electromagnetic (E-M) losses in the form of heat from the turbo-alternator system. This state corresponds to the Load inlet pressure and inlet enthalpy, plus the enthalpy changes due to each form of loss, as shown in Eq. 4.28.

$$h_{cav} = h_{load,in} + \Delta h_{windage} + \Delta h_{E-M} + \Delta h_{bearing} \tag{4.28}$$

The windage and E-M losses are calculated by the alternator component, while the bearing loss is calculated by the load component and is a function of T_{cav}. As such, a shooting method is used to estimate and update the bearing loss until the cavity temperature converges.

With the cavity thermodynamic state set by the known temperature and pressure, the bearing loss is approximated by the empirical relation in Eq. 4.29 (developed by Klann for CCEP [91]), where μ_{cav} is the cavity viscosity in lbm/ft-hr, w_{wheel} is the total rotating weight of the turbo-alternator system (compressor + shaft +

turbine + alternator) in lbf, N_{shaft} is the shaft speed in rpm, and p_{cav} is the cavity pressure in psi.

$$\dot{W}_{bearing} = -0.01 \frac{\mu_{cav}}{0.080} \frac{w_{wheel}}{50.962}^{1} .5 \frac{N_{shaft}}{32000}^{1} .5 \frac{p_{cav}}{31.845} \tag{4.29}$$

Join4 (Joiner)

Join4 accounts for the return of some portion of the load cooling bleed that split off at the beginning of Duct4. The "Joiner" component class in NPSS operates in a similar manner to "Splitter_x" in reverse. It simply adds the flow rates of the two incoming streams, as shown in Eq. 4.30.

$$\dot{m}_{out} = \dot{m}_{in,1} + \dot{m}_{in,2} \tag{4.30}$$

Start_A (HeXeStart)

As a recuperator is used in this system, a second Start element is required for the hot side of the Brayton cycle. Start_A also represents He-Xe and is located immediately upstream of the recuperator hot leg inlet. The only difference between Start and Start_A is that the pressure, temperature, and mass flow rate all vary in this element such that the inlet conditions match the exit.

Recuperator (Recupx)

The recuperator component analysis comes directly from CCEP and uses the model of an offset strip fin compact heat exchanger that can be found in Kays and London [92]. The component solver is set up in NPSS to vary the recuperator length in order to match a user-specified effectiveness, which for this model is 90%.

Duct6 (GDuct)

Duct6 connects the recuperator cold flow exit to the reactor inlet. This duct assumes the same geometry as the Duct4 (1.3 m long, one 90 degree bend, diameter set to produce a 0.2% pressure drop).

HSHX (TieTube)

For the BNTR model, the hot-side heat exchanger (HSHX) component model has been replaced with the same tie tube model developed for the propulsion-mode. During power-mode operation, the solver setup for the tie tube is modified slightly from that for propulsion. First of all, the thermodynamic package is modified to model He-Xe rather than Hydrogen. Rather than being set as an independent, the weight flow rate through the tie tubes is assigned directly from the inlet port, meaning that it maintains the flowrate set by the original He-Xe Start component. Instead, the reactor power and tie tube exit pressure are varied in order to satisfy the user-specified turbine inlet temperature and the tie tube pressure matching constraint.

Duct8 (GDuct)

Duct8 connects the tie tube exhaust to the turbine inlet. It also assumes a length of 1.3 m with one 90 degree bend.

Join8 (Joiner)

Join8 combines some of the load cooling / lubrication flow with the tie tube exhaust before entering the turbine.

HPT (Turbine_x)

The high pressure turbine (HPT) component model is a combination of the standard NPSS turbine model, and that from CCEP. Similar to the compressor (HPC), the turbine model requires a user-specified efficiency but then varies the pressure ratio to match the power requirements of the compressor, alternator, and load.

The CCEP turbine analysis uses the inlet temperature and given pressure ratio to calculate the isentropic exit temperature, as shown in Eq. 4.31. The thermodynamic state for the isentropic exit conditions are then set by the NPSS thermodynamics package by combining the isentropic exit temperature with the actual exit pressure, which comes from applying the pressure ratio to the inlet pressure.

$$T_{out,s} = T_{in}\pi_c^{-(\gamma-1)/\gamma} \tag{4.31}$$

The actual turbine enthalpy change can now be found in terms of the inlet enthalpy, isentropic exit enthalpy, and turbine efficiency, as shown in Eq. 4.32. The enthalpy change is then used to determine the actual exit enthalpy, which (combined with exit pressure) sets the thermodynamic state for the turbine exit. The power and torque delivered by the turbine are calculated in the same manner as the NTR turbine model in Eqs. 4.7 and 4.8, respectively.

$$\Delta h_t = \eta_t \left(h_{in} - h_{out,s}\right) \tag{4.32}$$

Duct10 (GDuct)

Duct10 closes the He-Xe loop by connecting the turbine exhaust to the Start_A element. It also assumes the same geometry as Duct6 and Duct8.

Start_NaK (NakStart)

Start_NaK is the start/end of the Sodium Potassium (NaK) liquid metal heat rejection loop. It operates in an identical manner to the second He-Xe start element, Start_A.

Pump (Pump_x)

Pump is the model for the NaK liquid metal pump. Based on the user-specified exit pressure, the pump model calculates the volumetric flow rate and pressure rise across the pump, which are then used to estimate the pump efficiency and mass from a table for annular linear induction pumps (ALIP).

Volumetric flow rate is calculated in terms of the pump flow rate and inlet flow density, as shown in Eq. 4.33. As NaK is a liquid metal, it can be assumed to be incompressible. The pump pressure rise is simply the difference between the inlet pressure that is set by the engine solver, and the user-specified exit pressure, as shown in Eq. 4.34. For this model the exit pressure is assumed to be 40 psi. The pump efficiency comes from tabulated data for ALIP pumps in terms of $\dot{(V)}$, in gallons per minute, and Δp, in psi. Once the efficiency is known, the required pump power is calculated in terms of the pressure rise, density, efficiency and flow rate as shown in Eq. 4.35. While not shown here specifically, special attention should be

paid that the units of Δp and $\dot{W}$ are compatible.

$$\dot{V} = \frac{\dot{m}}{\rho_{in}} \tag{4.33}$$

$$\Delta p = p_{out} - p_{in} \tag{4.34}$$

$$\dot{W}_{pump} = \dot{m}\frac{\Delta p}{\eta_p \rho} \tag{4.35}$$

Split13 (Splitter_x)

Split13 accounts for Nak bleed flow that is used for alternator cooling. Although it uses a different working fluid, the function of this component is the same as Split4 in Brayton cycle loop.

Alternator (Alternator)

The alternator component model also comes directly from CCEP. Its purpose is to calculate the windage (viscous) and electro-magnetic (E-M) alternator losses and the required torque for a given electric power output. For the purposes of this project, an additional solver mode was added to vary the alterantor power in order to match a given reactor power. This was required as an intermediate solution step to help with model convergence – a process that will be explained at the end of this chapter.

The alternator windage loss is approximately by the empirical relation in Eq. 4.36 (developed by Klann for CCEP [91]), where W_{con} and R_{con} are semi-empirical parameters based on the flow density and shaft speed (as defined in Eqs. 4.37 and 4.38) and the vectors R and XL contain various scaled alternator dimensions (defined in Eqs. 4.39 and 4.40).

The geometry for the current system is defined as follows. The constant X_{gap} is the fluid gap between the rotor and stator, and is assumed to be 0.08 inches. The rotor diameter (D_A) and stator diameter (D_S) are scaled to be 3.42 and 2.22 inches, respectively. Finally the terms L_P, L_S, and L_T are the rotor pole, minor rotor side, and rotor taper lengths, and (in this model) have scaled values of 1.71, 1.74, and 1.01 inches, respectively.

$$\dot{W}_{windage} = -0.406\, W_{con} \sum_{i=1}^{3} \left[(R_{con} R_i)^{-}\, 0.2937 R_i^4 X L_i \right] \tag{4.36}$$

$$W_{con} = 1.3229e-4\, \rho \left(\frac{2\pi N_{shaft}}{60} \right)^3 \tag{4.37}$$

$$R_{con} = 3600\rho \frac{x_{gap}}{12} \left(\frac{2\pi N_{shaft}}{60} \right) \tag{4.38}$$

$$\mathbf{R} = \left[\frac{D_A}{24},\ \frac{D_A + D_S}{24},\ \frac{D_S}{24} \right] \tag{4.39}$$

$$\mathbf{XL} = \left[\frac{L_P}{12},\ \frac{L_T}{6},\ \frac{L_S}{24} \right] \tag{4.40}$$

The E-M losses are represented by a tabulated values of power generation efficiency (η_a) in terms of net output power (P_{sys}). In general, the table covers output power levels from 0 kW to 100 kW, with corresponding efficiency values from 90% to 94%, respectively. The E-M losses are then calculated from the given system power output and alternator efficiency, as shown in Eq. 4.41.

$$\dot{W}_{E-M} = \left(1 - \eta_a^{-1} \right) P_{sys} \tag{4.41}$$

Finally, the required torque is calculated by dividing the gross alternator power (system + windage + E-M) by the shaft speed, as shown in Eq. 4.42.

$$\tau_a = \left(P_{sys} - \dot{W}_{windage} - \dot{W}_{E-M} \right) \frac{60}{2\pi N_{shaft}} \tag{4.42}$$

Gas_Cooler (Whex)

Gas_Cooler is the name of the Brayton cycle cold-side heat exchanger. It is used to reject the waste heat from the Brayton cycle to the radiator loop. As such, the hot leg working fluid is He-Xe while the cold-leg is Nak. The component model is based on the same *Kays and London* analysis as the recuperator, modeling the gas cooler as a compact heat exchanger with a design effectiveness of 97%.

Join15 (Joiner)

Join15 combines the alternator coolant and gas cooler exhaust streams and send them to the radiator.

Radiator (Radiator)

Radiator is another CCEP component that calculates the required radiator size and mass in order to reject the Brayton cycle waste heat transferred across the gas cooler. It does so by varying the coolant tube diameter and length for a given flat, two-sided radiator rejecting to a sink temperature of 200 K with an emissivity of 90%. BNTR system radiators are generally single-sided, corrugated, truncated cones, so the CCSS-based weight analysis is ignored in the BNTR model. The radiator area, however, should still apply to any radiator design (keeping in mind that the BNTR radiators are 1-sided).

The radiator area is calculated from the traditional Stefan-Boltzmann Law (Eq. 4.43)for thermal radiation, which related the radiative heat transfer to the radiator area, radiator and sink temperatures, emissivity, and the Stefan-Boltzmann constant (σ = 5.670e-8 Wm-2K-4). The emissivity (ϵ) and sink temperature are

given, and the radiator temperature and heat transfer are calculated from the convective heat transfer from the NaK coolant through the radiator. This model assumes that the radiator is constructed of four panels with 28 tubes apiece, for a total of 112 coolant tubes. The friction and heat transfer in the tubes is modeled in a similar manner to the fuel elements, which will be presented in detail in the following chapter. As stated above, the diameter and length of the radiator tubes is varied until the calculated coolant pressure drop equals that coming from the NPSS solver.

$$Q_{rad} = \epsilon \sigma A_{rad} \left(T_{rad} - T_{sink}\right)^4 \tag{4.43}$$

Shaft (Shaft_x)

The shaft component connects the various components of the turbo-alternator system (compressor, turbine, alternator, and load). It operates in the same manner as the propulsion model shaft, verifying that the next torque is zero, as shown in Eq. 4.15.

PERF (Performance)

Performance is not a physical element in the system, but is instead performs a set of system-level calculations to complete the analysis from CCEP. It does not have its own component file, but instead is written directly into the power cycle model. The primary purpose of this element is to calculate the total mass of He-Xe gas required for the Brayton cycle. This is accomplished by adding the individual gas mass values, which are calculated at the end of each component from the local

gas density and gas-path volume, as shown in Eq. 4.44

$$m_{gas} = \sum_{i=1}^{N} (\rho_i V_i) \tag{4.44}$$

4.3.4 Power Mode Execution

The high non-linearity of the three coupled loops of the CCSS-based power model can make convergence extremely difficult within the NPSS solver. The design space for the model is sparse and the solver has difficulty finding a solution that can produce the desired output power with the CCSS-based initial conditions. To solve this problem, a multi-step solution method has been created. In the first step, the model is solved by varying the alternator output power in order to find a design that corresponds to a reactor thermal power of 180 MWt. Once that has been accomplished, the NPSS solver is modified so that the reactor power is varied in order to produce the required alternator power. This process has been automated, and the penalty for running the initial convergence case is approximately one minute on the computer used for this research.

Chapter 5

Reactor Analysis

5.1 Overview

As discussed in the previous chapter, the primary analytical focus of this dissertation has been reactor modeling. This has come in the form of separate component models for the reactor fuel elements and tie tubes. In both cases, 1-D thermodynamic models have been employed in order to account for the axial variation in heat deposition, wall temperature, and friction along the length of the reactor. This level of analysis adds fidelity over a 0-D model by calculating the pressure loss in each element directly. The following sections present the details of this analysis and its implementation in the fuel element and tie tube component models.

5.2 Fuel Elements

The purpose of the fuel element analysis is to calculate the propellant pressure drop across a single fuel coolant channel. The propellant temperature increase can be calculated directly from the known reactor power, but the pressure drop is driven by

friction along the length of the fuel element coolant channels. Friction is a function of wall temperature, which varies along the length of the element, so a 1-D analysis is required to solve this problem. This method is based on the reactor analysis from NESS [43], but has been changed slightly to allow for a different axial power profile and to correct mathematical errors.

For the sake of simplicity, the fuel element analysis is performed on a single coolant channel in the reactor. As is standard practice in nuclear engineering, this analysis is performed on the channel that experiences peak heating across the entire reactor. This is done in order to calculate the peak internal fuel material temperature in the reactor, which is the primary constraint during propulsion-mode operation. The radial power distribution in the reactor is accounted for by assuming a maximum-to-average power factor (Ω), which is defined as follows.

$$\Omega = P_{max.}/P_{avg.} \tag{5.1}$$

In a homogeneous, un-reflected reactor with a typical Bessel function power distribution, peak heating occurs in the center of the reactor core. For a real reactor, like the NERVA-based design studied here, the location of this channel is unknown. The effects of the reflector, control drums, and other non-homogeneous elements must be accounted for in order to calculate the location of peak heating. Such an analysis would require a 3-D model of the entire reactor geometry, materials, and neutron flux distribution and is beyond the scope of this project.

For a NERVA-derived engine, the power factor will have little impact on the coolant thermodynamics, because these engines employ flow orifices that are de-

signed to match the local flow in each channel with the local heating [31]. The net result is that the propellant inlet and exit temperatures should be nearly equal for every channel.

5.2.1 Propellant Thermodynamics

The temperature change across the reactor is driven by the heat transfer from the reactor fuel elements to the hydrogen propellant. The pressure change, on the other hand, is driven by friction along the channel wall. As such, the fuel element analysis requires the calculation of flow in a constant area duct with heat addition and friction. A closed-form solution for this problem could be generated using the method of influence coefficients, as presented by Shapiro [93]. For use with NPSS and its solver and thermodynamics packages, however, this analysis is more easily performed by discretizing the fuel element into many segments of constant wall temperature and numerically integrating the effects of heat addition and friction along the channel. The fuel element differential for this system is illustrated in Fig. 5.1. Note that the solver traverses the element from the chamber to the inlet, opposite of the flow of hydrogen propellant.

The heat addition along a single element is derived from the quasi-1D form of the conservation of energy.

$$h_{o,i+1} = h_{o,i} - d\dot{Q} \tag{5.2}$$

For a calorically perfect gas, Eq. (5.2) can be rewritten in terms of total temperature.

$$T_{o,i+1} = T_{o,i} - d\dot{Q}/\left(\dot{m}C_p\right) \tag{5.3}$$

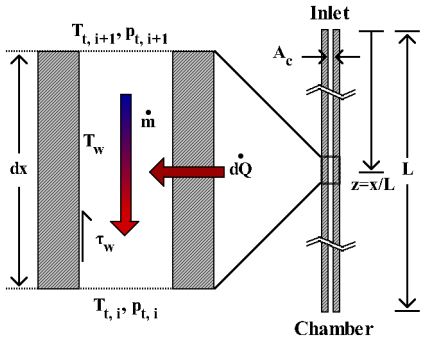

Figure 5.1: Fuel differential element.

For steady state operation, the incremental heat addition ($d\dot{Q}$) to the coolant is equal to the reactor power generated at that axial location. The axial power distribution for this study comes from recent 3-D reactor modeling performed by Bruce Schnitzler at NASA Glenn Research Center, and will be discussed further in the following chapter [94].

Pressure is calculated from a momentum balance across the differential, where the pressure drop is driven by the friction at the channel wall. This calculation begins with the quasi-1D form of the conservation of momentum, as shown in Eq. 5.4.

$$p_{i+1}A_c + \rho_{i+1}u_{i+1}^2 A_c = p_i A_c + \rho_i u_i^2 A_c + \tau_w dA_w \tag{5.4}$$

The shear stress at the wall (Eq. 5.5 can be written in terms of the coefficient of friction and average density and velocity across the element.

$$\tau_w = \frac{1}{2}\rho \bar{u}^2 C_f \tag{5.5}$$

Equations (5.4) and (5.5) can then combined and further simplified by using conti-

nuity to write ρu^2 in terms of $\dot{m}$, A, and ρ, as shown in Eq. 5.6.

$$p_{i+1}A_c + \frac{1}{\rho_{i+1}}\left(\frac{\dot{m}}{A_c}\right)^2 A_c = p_i A_c + \frac{1}{\rho_i}\left(\frac{\dot{m}}{A_c}\right)^2 A_c + \frac{1}{2\bar{\rho}}\left(\frac{\dot{m}}{A_c}\right)^2 C_f dA_w \tag{5.6}$$

The final form shown in Eq. (5.7) is generated by dividing both sides of Eq. (5.6) by A_c, grouping like terms, rewriting the areas in terms of the hydraulic diameter (D_h) and dx, and finally rewriting the average density in terms of the boundary values.

$$p_{i+1} = p_i + \left(\frac{\dot{m}}{A_c}\right)^2 \left[\frac{1}{\rho_i} - \frac{1}{\rho_{i+1}} + \frac{1}{\rho_i + \rho_{i+1}}\frac{4C_f dx}{D_h}\right] \tag{5.7}$$

The coefficient of friction (C_f) for turbulent flow in a long, smooth tube is calculated from the Taylor correlation with film temperature correction [95].

$$C_f = \left(0.0014 + 0.125 Re_w^{-0.32}\right)\sqrt{\frac{\bar{T}_o}{T_w}} \tag{5.8}$$

5.2.2 Propellant-Fuel Element Heat Transfer

Now that the average bulk propellant temperature is known, the channel wall temperature can be calculated from convection between the wall and propellant, as shown in Eq. 5.9.

$$T_w = \bar{T}_o + \frac{d\dot{Q}}{h_c A_w} \tag{5.9}$$

The convective heat transfer coefficient can be written in terms of the Nusselt number, as shown in Eq. (5.10), where $\bar{k}$ is the average propellant thermal conductivity for that segment of the channel. For turbulent flow, the Nusselt number is calculated from the McCarthy-Wolf correlation, with film temperature and entry corrections (Eq. 5.11 [96].

$$h_c = Nu\,\bar{k}/D_h \tag{5.10}$$

$$Nu = 0.025 Re^{0.8} Pr^{0.4} \left(\frac{\bar{T}_o}{T_w}\right)^{0.55} \left[1 + 0.3 \max\left(4.8, \frac{x}{D_h}\right)^{-0.7}\right] \tag{5.11}$$

The peak temperature inside the fuel rod at a particular axial location is calculated from thermal conduction from the wall into the fuel, assuming negligible axial heat transfer. This assumption should be valid as the fuel rod is many times longer than it is wide. For the hexagonal fuel geometry of a NERVA-derived NTR, the expression for peak internal fuel temperature (T_f) in Eq. 5.12 may be derived, where ψ and κ are empirical constants based on the geometric properties of the fuel element as defined by Eqs. (5.13) and (5.14).

$$T_f = T_w + \frac{d\dot{Q}\psi}{k_f A_f \kappa} \tag{5.12}$$

$$\psi = \left(\frac{S}{2}\right)^2 \left[0.55133 \ln\left(\frac{S}{D_h}\right) + 0.25\left(\frac{D_h}{S}\right)^2 - 0.23446\right] \tag{5.13}$$

$$\kappa = \frac{D_h}{4}\left[\left(\frac{\pi D_h^2}{3.14641 S^2}\right)^{-1} - 1\right] \tag{5.14}$$

5.2.3 Solution Method

Equations (5.8) and (5.11) require prior knowledge of the wall temperature and Eq. (5.7) requires prior knowledge of the density at $i+1$, so this problem must be solved iteratively. For simplicity, a shooting method is employed such that initial values of T_w and ρ_{i+1} are assumed and then updated until they converge. A more sophisticated update scheme could reduce the total run time of this analysis, but with modern computing power the shooting method is fast enough and an updated scheme is unnecessary.

As mentioned previously, the solver traverses the fuel element channel in reverse, calculating the required fuel element inlet pressure and temperature for given chamber conditions. The chamber conditions are fixed by engine thrust and specific impulse, which are generally specified by the engine design point. This process is implemented in NPSS by defining the fuel element flowrate as an independent parameter that is varied until the reactor inlet pressure calculated by the component model equals the actual inlet pressure from the engine model.

5.3 Tie Tubes

A similar analysis to that of the fuel element is used to calculate the pressure drop across a reactor tie tube. The primary difference in the tie tube analysis is that the two counter-flow channels must be solved simultaneously. As presented in Chapter 3, NERVA-derived tie tubes are constructed from several concentric layers, with heating loads that vary widely between propulsion and power generation modes. As such, the tie tube analysis must also account for heat generation within the solid walls, as wells as conduction through the walls and convection to the coolant. This has required a more rigorous heat transfer analysis to be developed for the tie tube component model, as presented below.

5.3.1 Coolant Thermodynamics

Figure 5.2 illustrates the thermodynamics of a tie tube differential element control volume. As mentioned previously, heat transfer into the coolant comes

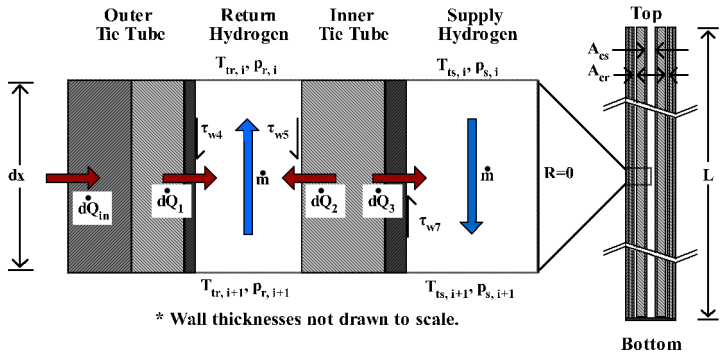

Figure 5.2: Differential element illustrating tie tube thermodynamic analysis.

from conduction into the tie tube from adjacent fuel elements ($d\dot{Q}_{in}$) and from heat generation within the material layers ($\dot{g}$). To simplify calculations, the outer layer is assumed to be cylindrical, ignoring the hexagonal cross-section at the outer wall. As such, the entire tie tube is axisymmetric and the differential element is a radial slice of height dx.

The temperature and pressure changes in the tie tube are calculated in a similar manner to the fuel element. The complex tie tube geometry, however, requires some changes to the equations. The solver traverses in the same direction as the supply flow but in the opposite direction of the return flow. Thus, the signs on some of the terms are reversed. Additionally, the return channel calculations contain additional terms to account for the simultaneous heat addition and friction from the outer and inner channel walls (labeled as $w4$ and $w3$, respectively). The temperature and pressure changes are presented in Eqs. 5.15 through 5.18.

$$T_{os,i+1} = T_{os,i} + \frac{d\dot{Q}_{w1}}{\dot{m}C_p} \tag{5.15}$$

$$T_{or,i+1} = T_{or,i} - \frac{d\dot{Q}_{w3} + d\dot{Q}_{w4}}{\dot{m}C_p} \tag{5.16}$$

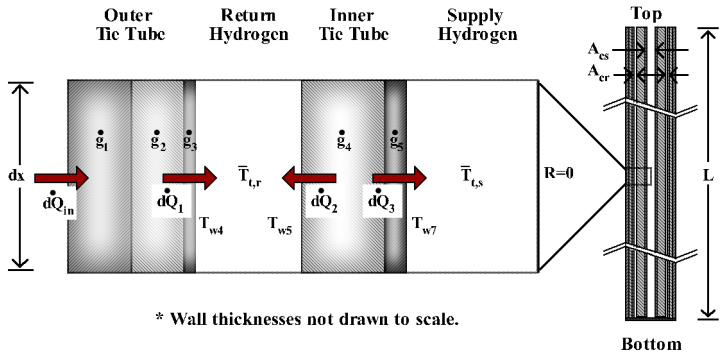

Figure 5.3: Differential element illustrating tie tube heat transfer analysis.

$$p_{s,i+1} = p_{s,i} + \left(\frac{\dot{m}}{A_{c\,s}}\right)^2 \left[\frac{1}{\rho_{s,i}} - \frac{1}{\rho_{s,i+1}} - \frac{1}{\rho_{s,i}+\rho_{s,i+1}} \frac{4C_{f\,w1}dx}{D_{h\,s}}\right] \tag{5.17}$$

$$p_{r,i+1} = p_{r,i} + \left(\frac{\dot{m}}{A_{c\,r}}\right)^2 \left[\frac{1}{\rho_{r,i}} - \frac{1}{\rho_{r,i+1}} + \frac{1}{\rho_{r,i}+\rho_{r,i+1}} \frac{1}{A_{c\,r}} \left(C_{f\,w3}dA_{w3} + C_{f\,w4}dA_{w4}\right)\right] \tag{5.18}$$

5.3.2 Heat Transfer

The tie tube heat transfer is also more complicated than that of the fuel element. In this case, there is heat transfer into the tie tube from adjacent fuel elements, volumetric heat generation within the material layers, and thermal conduction between layers. Finally, all of the heat which enters the tie tube must transfer to the coolant through convection at the channel walls. Figure 5.3 illustrates these processes in the tie tube system.

Heat transfers from the tie tube walls to the supply and return coolant by convection (Eq. 5.19, and through the tie tube walls by conduction. For a cylindrical geometry with negligible axial and azimuthal conduction, Eq. (5.20) gives the general form for steady-state radial conduction with constant conductivity and heat

generation. The values for heat generation ($\dot{g}$) in each of the tie tube walls come from the same 3-D reactor modeling as the reactor power distribution, and will be discussed in the following chapter.

$$d\dot{Q} = h_c A_c \left(T_w - \bar{T}_o \right) \tag{5.19}$$

$$\frac{1}{r}\frac{d}{dr}\left(r\frac{dT}{dr} \right) + \frac{\dot{g}}{k} = 0 \tag{5.20}$$

Equation (5.21) gives the radial temperature distribution in a particular tie tube wall, and is produced by integrating Eq. (5.20) twice with respect to r, where C_1 and C_2 are constants of integration determined by the boundary conditions of that layer.

$$T_w(r) = -\frac{\dot{g}r^2}{4k} + C_1 \ln r + C_2 \tag{5.21}$$

The boundary conditions for this system are: convection at the supply and return channel walls (as given by Eq. (5.19)), equal temperature and heat flux at the interface of adjacent layers, and specified heat flux at the outside of the tie tube. As with the fuel power distribution and tie tube heat generation, the relative magnitude of heat conducted into a tie tube from adjacent fuel elements comes from the 3-D modeling work of Schnitzler [94]. These boundary conditions give a system of ten equations that can be solved for the ten unknown constants. The constants then allow the calculation of the wall temperatures and thus the solution of the rest of the system.

5.3.3 Solution Method

The coupled nature the tie tube analysis requires a slightly different solver setup from the fuel element. The supply and return coolant channels are treated as unique flowpaths with equal flow rates that are coupled by the conduction through the inner tie tube walls. The tie tube coolant inlet and exit temperature and pressure are varied at the engine level by the NPSS solver. The tie tube model then marches from those boundary conditions at the cold end down to the hot end of the tie tube, where the two channels should meet. In a real tie tube, the supply and return channels connect at the bottom, so the temperatures and pressures must be equal. The iteration scheme is set up such that the temperatures will always be equal at the bottom. To ensure that the pressures match as well, the tie tube flow rate has been added as an independent property in the NPSS solver that is varied until the pressures at the bottom of each channel are equal. As in the fuel element model, a shooting method is employed.

Chapter 6

Reference Engine Designs

Two reference engine designs will provide design points to test the new BNTR model. The first design is the Small Nuclear Rocket Engine (SNRE), which was published at the end of the NERVA program [37]– [39]. The SNRE is a propulsion-only engine and has been selected for its similarity to current BNTR engines and because current 3-D reactor modeling activities at NASA Glenn Research Center are using this design. The second reference design is the BNTR engine system proposed for use with DRM 4.0. This design has been selected for the BNTR design point because it represents the current standard for bimodal-powered spacecraft.

6.1 Small Nuclear Rocket Engine (SNRE)

The SNRE, as described in Section 2.1.2.3, is a propulsion-only engine with a thrust of approximately 72 kN and specific impulse of 860 s. The multi-mission, reusable SNRE design will be the first design point examined in this study. This point has been selected over other possible designs for several reasons: 1) it is comparable in size to the 66.7 kN thrust engines assumed for modern BNTR vehicles, 2) extensive details on the reactor design and operation are available in refs. [37]

and [38], and 3) this design is currently being used in a large-scale 3-D reactor modeling effort at NASA Glenn Research Center. As such, a great deal of data from that study has been provided, and will anchor the tie tube and fuel element heat deposition and heat transfer analysis in the current model.

6.1.1 Design Point Details

The multi-mission reusable SNRE, as explained previously, is designed to operate with a lower reactor power and fuel temperature to extend the usable life of the reactor. It has a total reactor power of 354 MW, which is provided by 564 fuel elements and 241 tie tubes. Figure 6.1 shows a summary of this design, including a flowpath layout with state point data throughout the engine. Most of the information should be self-explanatory, but a few important points should be noted. All of the coolant leaving the reflector and control drums enters the reactor core. The turbopump is driven entirely by the tie tube coolant. There is a pressure difference of approximately 0.08 MPa between the reflector and turbine exit flows as they meet at the reactor inlet. As such, backflow may be a concern at that location [37].

6.1.2 Heat Deposition Data

Proper quantification of the heat deposition and transfer into and between the fuel elements and tie tubes is essential to the accurate modeling of an NTR engine. Previous models, such as NESS, assume fixed empirical values for the heat transfer into each tie tube and fuel element, but do not specify what fraction of the tie tube

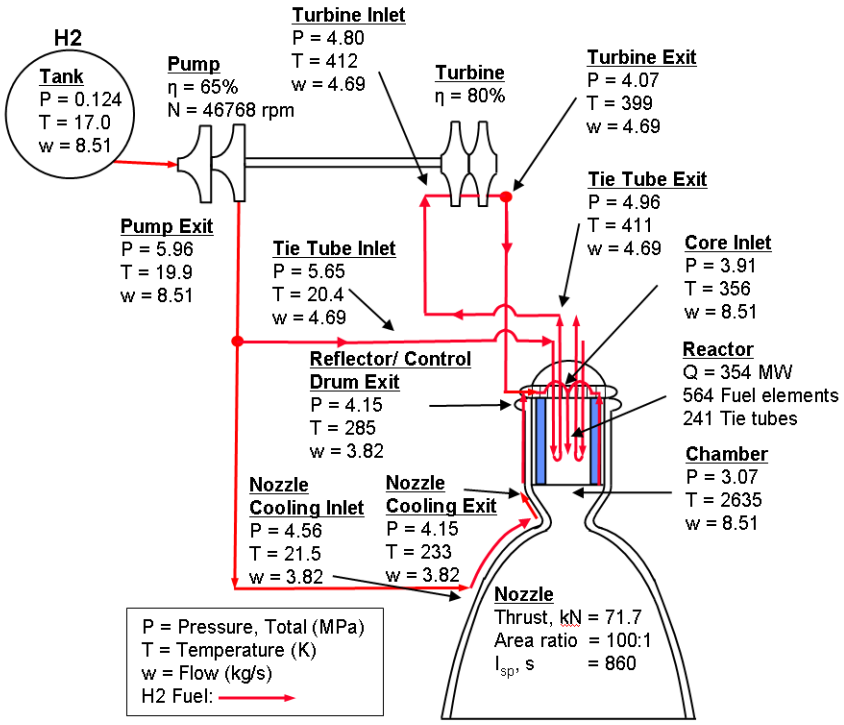

Figure 6.1: Detailed thermodynamic data for SNRE multi-mission design point. Data from Ref. [37], diagram courtesy of Stan Borowski.

heat is deposited directly into the material by radiation or is conducted through adjacent fuel elements [43]. Furthermore, the empirical data in NESS is based on the large 1000 MW reactors from the NERVA program, and will not be valid for modern BNTR design points. As such, updated values for the heat deposition and transfer must be obtained.

As stated previously, several individuals at NASA Glenn Research Center are currently performing a 3-D neutronics and heat transfer analysis of the 354 MW SNRE reactor design. Bruce Schnitzler is using the LANL Monte Carlo n-Particle (MCNP) code to model the 3-D neutronics of the reactor fuel elements and tie tubes. Mark Stewart is performing 3-D thermal and structural analysis of the fuel elements, tie tubes, their interfaces, and reactor coolant with ANSYS. These efforts

are being coordinated by Stan Borowski of NASA Glenn. As of the spring of 2007, this work is still in progress and has not been published. However, preliminary data from these studies have been provided in order to update the fuel element and tie tube heat transfer analysis [94].

Fuel Element Heat Deposition

From Schnitzler's analysis, the SNRE fuel elements have a direct energy deposition rate of 595.110 kW. Of this total amount, 99.51% goes into the fuel element itself, 0.46% goes into the protective ZrC coatings, and 0.03% is deposited directly to the coolant [94]. As such, it can be assumed that all propellant heating comes from convective transfer from the fuel element channel walls.

Tie Tube Heat Deposition

A similar analysis found that the average tie tube receives 28.128 kW directly. Of that, the majority (57.17%) is deposited in the ZrH moderator layer. The next highest deposition values are 21.00% and 12.40% to outer graphite filler and ZrC insulator layers, respectively. The Inconel layers of the outer and inner tie tubes themselves see 4.93% and 4.09%, respectively. Finally, the outer and inner hydrogen coolant channels receive only 0.30% and 0.11%, respectively, so this model will also assume all heating from convection at the channel walls [94].

Conduction at Fuel Element - Tie Tube Interface

Stewart is modeling the fuel element - tie tube interface by examining two adjacent 60 degree sectors of each, as illustrated in Fig. 6.2. This analysis shows

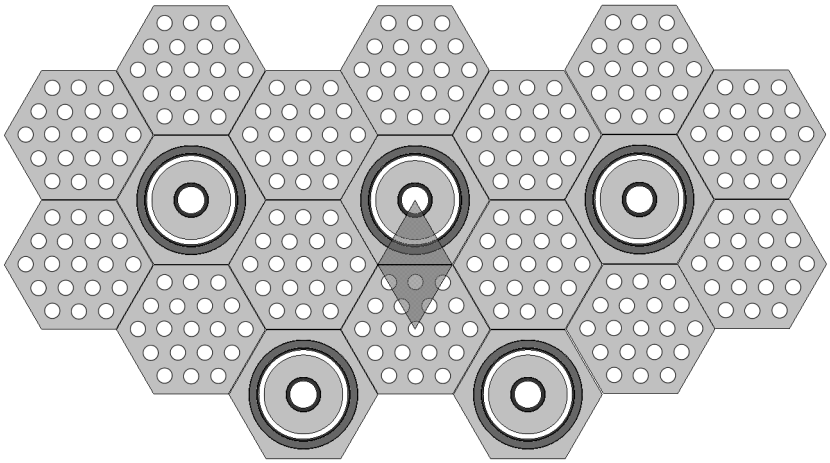

Figure 6.2: Portion of reactor core. Shaded region represents 60 degree sector interface examined by Stewart.

that 8% of the heat deposition into the fuel element sector conducts into the tie tube sector. This analysis, however, only represents one sixth of the total fuel element. As such, 1.33% of the total fuel element heat conducts across a single fuel element - tie tube interface. Looking at the adjacent elements around it, it is clear that one fuel element contacts tie tubes at only three of its six faces. As such, each whole fuel element actually loses 4% of its total heat deposition to adjacent tie tubes. A similar examination of a tie tube shows that it contacts fuel elements at all six faces, therefore the heat conduction it sees is equal to 8% of the heat deposited in the average fuel element [94].

Axial Power Distribution

The data so far only represents the total heat deposited in each portion of the fuel elements and tie tubes, but does not address its distribution. In order to reduce neutron leakage and maintain reactor criticality, nearly all nuclear reactors are designed with an axial power distribution such that the peak power is reached in

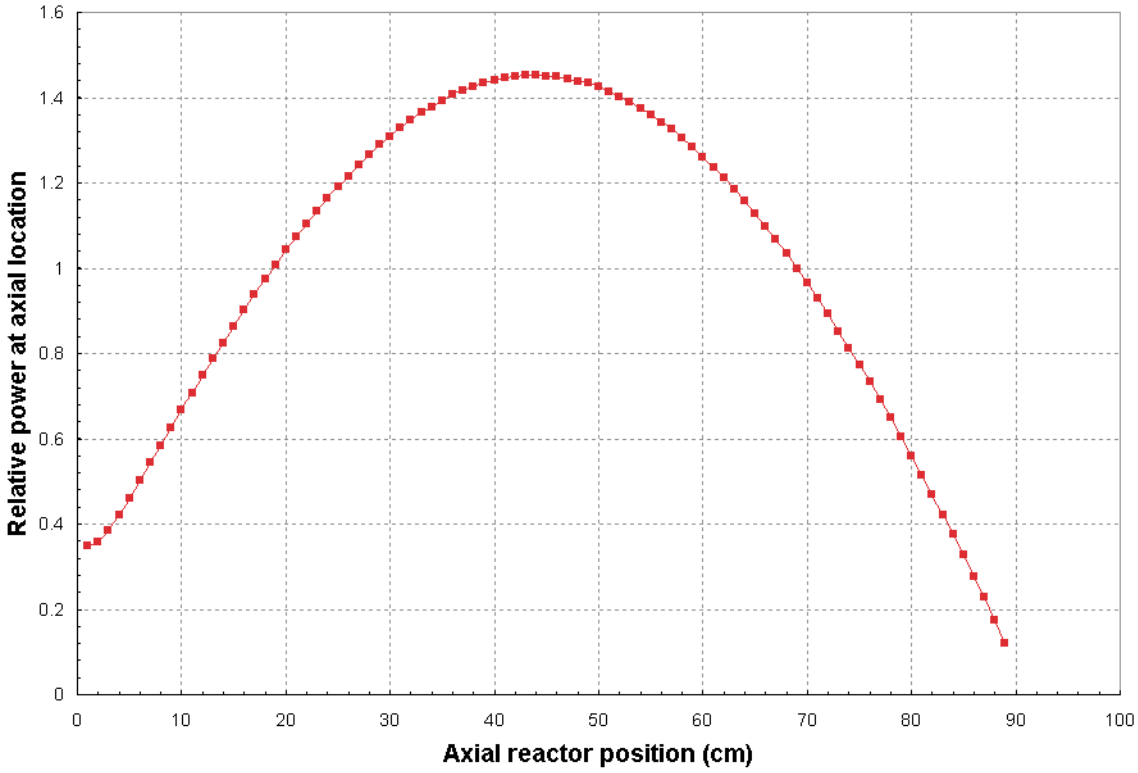

Figure 6.3: Average local power distribution, based on data from Schnitzler [94].

the center of the reactor, and tapers towards the outside. As a 1-D reactor analysis is employed in this study, only an axial distribution is required. This profile, as shown in Fig. 6.3 has been calculated by Schnitzler, and will be applied to all heat transfer and deposition values in the reactor [94].

Summary

Figure 6.4 combines all of the above data together to show the heat conduction into the tie tube as well as the heat generation within all of the tie tube layers. These values represent a single average element and are used directly in the tie tube component model. To model reactor of a different size (and power) than the SNRE, the magnitude of the heat deposition and transfer values in the fuel element and tie

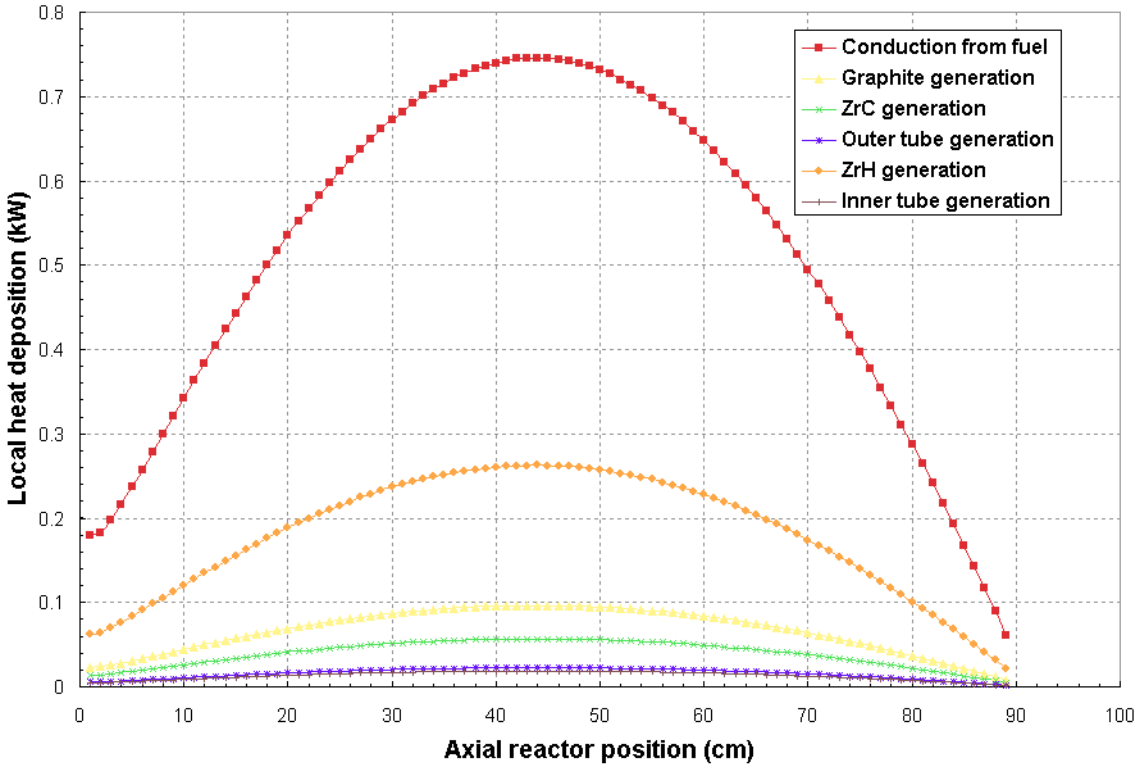

Figure 6.4: Tie tube heat conduction and generation distributions.

tubes models are scaled against again the 354 MW size used to produce the numbers presented above.

6.2 Design Reference Mission 4.0

As discussed in Section 2.2.3, DRM 4.0 is the current reference design for the manned exploration of Mars using BNTR technology. In DRM 4.0, all vehicles use three BNTR engines to provide propulsion and power generation throughout the entire mission. Each engine is capable of producing 66.7 kN thrust and 25 kWe power, though nominally all three engines will operate at 2/3 power to provide the 50 kW total power required by the vehicles [4].

Three smaller engines are chosen over one larger one for reduced manufacturing costs, engine-out capability, and (most importantly) to allow nuclear ground testing with currently available facilities. Current environmental safety regulations (not to mention general public opinion of nuclear technology) prohibit the type of upward-firing, open air NTR tests that took place during the majority of the NERVA program. The NERVA Nuclear Furnace reactor tests, however, demonstrated the use of a downward-firing engine test stand with exhaust radiation scrubbers [13]. It has been proposed that 66.7 kN thrust engines could use a similar system to allow safe nuclear ground testing at a relatively low cost [97].

The engine system from the original 1998 DRM 4.0 is not NERVA-derived; it is a BNTR based on a joint program with the former Soviet Commonwealth of Independent States (CIS). The CIS engine uses ternary carbide fuel material that can produce hydrogen exit temperatures of 3100 K and a chamber pressure of 13.8 Mpa. As shown in Fig. 6.5, it does not contain tie tubes like the NERVA engines, but instead uses a retractable plug to close off the nozzle for power-mode operation. In this manner, the fuel elements provide direct heating for both propulsion and power generation. The full details of this engine system can be found in Refs. [4] and [98].

The most recent DRM 4.0 studies have returned to a NERVA-derived BNTR system that uses the tie tubes to create a closed-loop Brayton cycle [22, 45]. As such, those studies will form the basis for the second reference engine for this project.

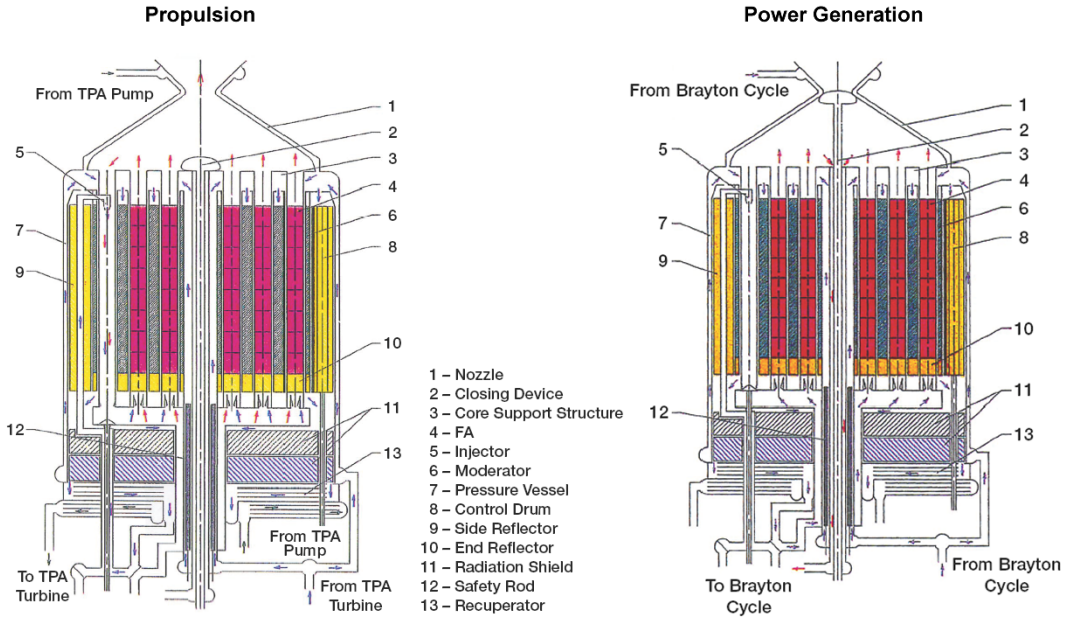

Figure 6.5: CIS BNTR engine originally assumed for Design Reference Mission 4.0 [4].

6.2.1 Propulsion Operation

While nearly all DRM 4.0 studies call for the use of 66.7 kN thrust engines, there is some discrepancy in the component details. Chamber temperature values from 2300–3100 K, chamber pressures from 5.4–13.8 MPa, nozzle area ratios from 100:1–300:1, and all manner of compressor and turbine efficiencies have been assumed among the various DRM 4.0 studies. Adding insult to injury, only a few of these studies actually present sufficient component-level results to permit comparison with the updated model. To account for these differences, a baseline DRM 4.0 engine design will be assumed and trade studies on these parameters will be examined. To compare the component-level results of the new model, two specific DRM 4.0-based engine designs will also be used for approximate matching case studies.

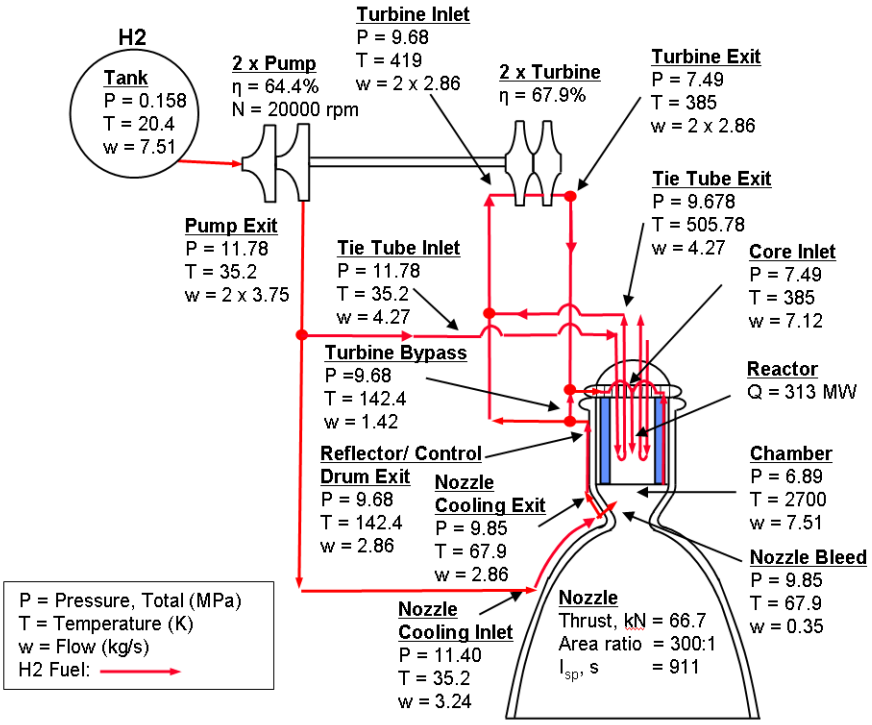

Figure 6.6: Propulsion mode details from DRM Case Study 1, data from Ref. [45], graphic modified from Ref. [22].

6.2.1.1 DRM Case Study 1 - Propulsion

The first DRM case study is useful because its results come from NESS, and will allow for a direct comparison between the new BNTR model and NESS. Reference [45] uses NESS to calculate the component-level data for another 66.7 kN NTR, operating with chamber conditions of 2700 K and 6.9 Mpa and compressor and turbine efficiencies of 68.5% and 70%, respectively. This case assumes a nozzle design with an area ratio of 300:1 that employs active cooling only up until an area of 25:1. This particular engine does not have a power-mode, but its propulsion-mode operation is nearly identical to the most common BNTR assumptions. The detailed component-level operating conditions for this engine are illustrated in Fig. 6.6.

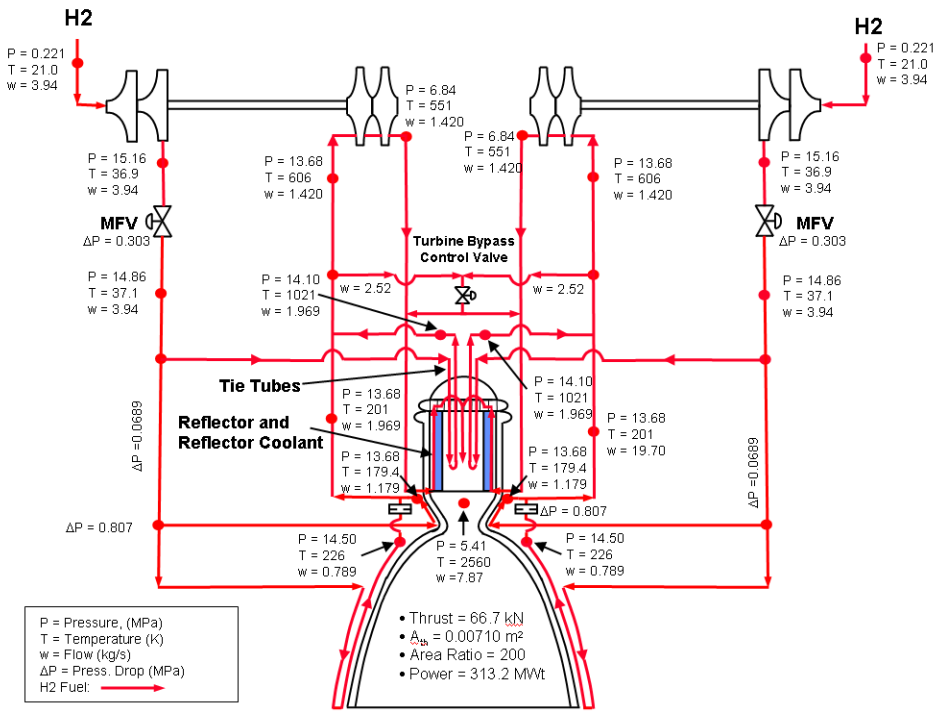

Figure 6.7: Propulsion mode details from DRM Case Study 2 [22].

6.2.1.2 DRM Case Study 2

The second DRM case study is based on the only known BNTR study that actually assumes tie tube heating for the power mode and provides accompanying cycle component data [22]. Reference [22] provides component thermodynamic data for a 66.7 kN BNTR with a chamber temperature and pressure of 2560 K and 5.41 MPa, respectively. Compressor and turbine efficiencies are 82% and 90%, respectively. Finally, a nozzle area ratio of 200:1 is assumed, with active cooling along the entire nozzle. Figure 6.7 shows detailed thermodynamic state data for this engine.

6.2.2 Power Generation

The power generation mode of DRM 4.0 assumes that a total spacecraft power requirement of 50 kWe is generated by three closed Brayton cycle generators attached to the three reactors. This corresponds to a nominal power level of 17 kWe per engine, or 25 kWe for engine-out capability. The 50 kWe design allows for hydrogen refrigeration to prevent boil-off en route to Mars and high date rate communications, in addition to traditional spacecraft power requirements. The primary power-mode variables between the various DRM 4.0 studies are the compressor and turbine inlet conditions. Turbine inlet temperatures can range from 1150–1300 K, depending on turbine materials selected. So, in a similar manner to the propulsion-mode, a baseline design will be selected and used for trade studies, while the power mode of DRM Case Study 2 will be examined for component performance comparison.

6.2.2.1 DRM Case Study 2 - Power

The power-mode operation of the BNTR in Ref. [22] assumes an electric power output of 37 kWe, turbine inlet temperature of 1150 K, and compressor and turbine efficiencies of 82% and 90%, respectively. Figure 6.8 shows the detailed component-level operating conditions for this design. While the electric power generation for this design is substantially higher than that of the typical DRM 4.0 design, it is the only known study that presents component-level details for a power generation systems that assumes the use of tie tubes for heating [22].

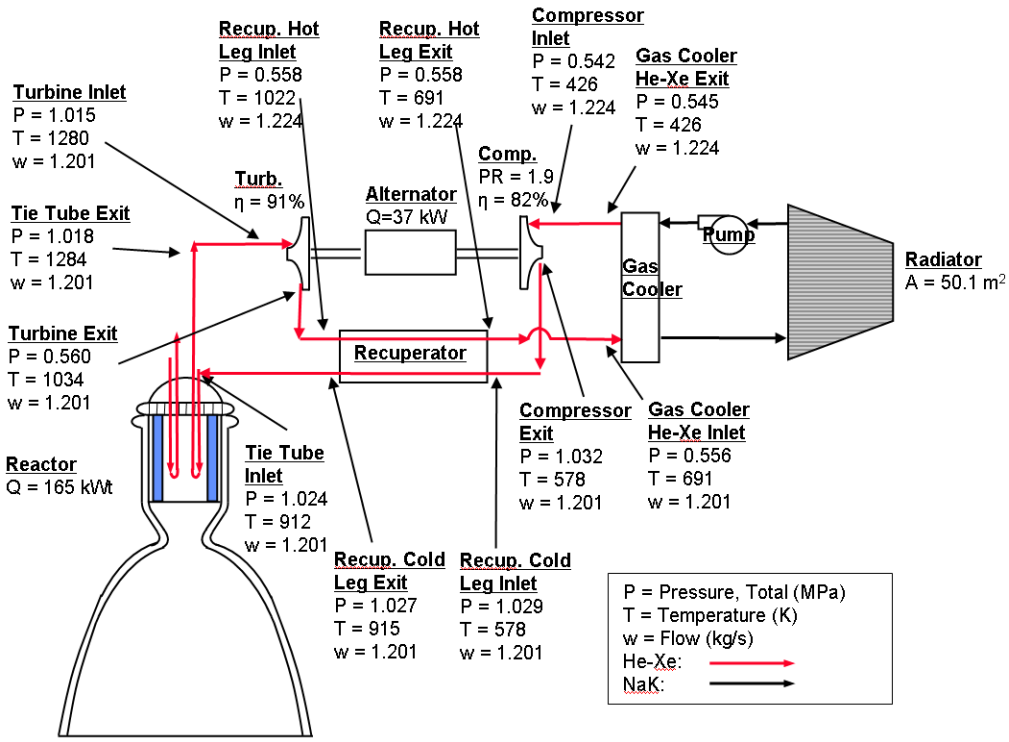

Figure 6.8: Power mode details from DRM Case Study 1 [22].

Chapter 7

Results

This chapter begins with the results obtained by modeling the reference designs discussed in Chapter 6. The propulsion mode operation of SNRE and two DRM case studies will be presented first, followed by the power generation case study and finally, the BNTR baseline design. Next, the results of trade studies on the sensitivity of propulsion and power performance to some of the assumed input parameters will be presented. This chapter concludes with a brief discussion of engine technology limitations that arise from the results.

7.1 Design Point Results

7.1.1 SNRE

As discussed previously, the SNRE engine is the basis of the high-fidelity reactor modeling efforts at NASA Glenn. The data from this NASA work is being used to anchor the heat generation and transfer assumptions within the current model. As such, a comparison between the results from the present model and from the original SNRE publication should highlight possible strengths and limitations of the new BNTR model.

7.1.1.1 Engine-Level Performance

Figure 7.1 shows the state point results for the SNRE design point. The bold-face values represent user-specified input conditions, the values of which have been selected to represent the SNRE as closely as possible. The primary design conditions are a thrust of 71.7 kN, chamber temperature and pressure of 2635 K and 3.07 MPa, respectively, and nozzle area ratio of 100:1. Additionally, the tank conditions are assumed to be 17 K and 0.124 MPa and the compressor and turbine are assumed to operate with 65% and 80% efficiency, respectively. The original SNRE design assumed a shaft speed of more than 46000 rpm, but without the same pump and turbine maps, that operation cannot be matched. As such, all propulsion designs in the BNTR model will assume the same shaft speed of 10000 rpm. For the present model of steady-state operation with a user-specified efficiency, the shaft speed should not affect the engine performance.

Based on the results of the BNTR model, the SNRE design requires a reactor power of 336.3 MW with 535 fuel elements and 202 tie tubes. This is somewhat lower than the 354 MW, 564 fuel elements and 241 tie tubes of the original SNRE design. The reactor power and number of fuel elements are each approximately 5% lower with the new BNTR model. The reduction in number of tie tubes is more significant at 16%. One possible reason for this difference is that the number of tie tubes in the present model is still based on an empirical calculation from NESS. Although the fuel-to-tie tube ratio is assumed to be nominally 3:1, NESS adds on an additional factor to account for extra tubes around the periphery of the core.

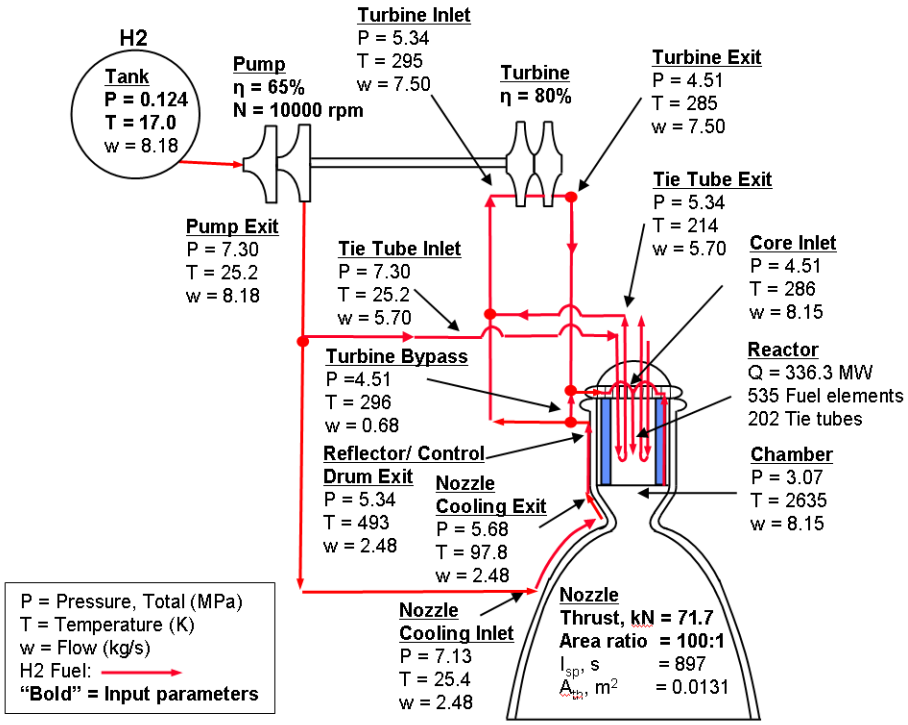

Figure 7.1: Detailed thermodynamic results for SNRE design point. Engine diagram courtesy of Stan Borowski.

Table 7.1 lists these differences as well as those in other engine parameters.

The last column of Table 7.1 shows that although the tank and chamber pressures are the same for the BNTR model and SNRE design, the rest of the pressure values throughout the engine are predicted to be much higher with the BNTR model. The pressure increase starts at the fuel pump, which has an exit pressure nearly 22.5% higher than that of the original SNRE design. The tie tube, nozzle cooling jacket, and reactor core inlet pressures are all similarly high as well, but by the time the propellant leaves the reactor core, it has met the user-specified chamber pressure. This implies that the friction losses within the BNTR model are more severe than those assumed in Ref. [37]. One possible reason for this is that tie tube exit temperature calculated by the BNTR model is significantly lower than

Table 7.1: Difference between SNRE results from BNTR model and design from Ref. [37].

Component	Properties	BNTR Model	SNRE	Δ,%
Nozzle	Specific impulse, s	897	860	4.30
Reactor	Power, MW	336	354	-5.00
	Fuel Elements	535	564	-5.14
	Tie Tubes	202	241	-16.18
Tank	Pressure, MPa	0.124	0.124	0.00
	Temperature, K	17.0	17.0	0.00
	Flow rate, kg/s	8.18	8.51	-3.88
Pump Exit	Pressure, MPa	7.30	5.96	22.48
	Temperature, K	25.2	19.9	26.63
	Flow rate, kg/s	8.18	8.51	-3.88
Tie Tube Inlet	Pressure, MPa	7.30	5.65	29.20
	Temperature, K	25.2	20.4	23.53
	Flow rate, kg/s	5.7	4.69	21.54
Tie Tube Exit	Pressure, MPa	5.34	4.96	7.66
	Temperature, K	214	411	-47.93
	Flow rate, kg/s	5.70	4.69	21.54
Nozzle Cooling Inlet	Pressure, MPa	7.13	4.56	56.40
	Temperature, K	25.4	21.5	18.14
	Flow rate, kg/s	2.48	3.82	-35.08
Turbine Inlet	Pressure, MPa	5.34	4.80	11.25
	Temperature, K	295	412	-28.40
	Flow rate, kg/s	7.50	4.69	59.91
Core Inlet	Pressure, MPa	4.51	3.91	15.35
	Temperature, K	286	356	-19.66
	Flow rate, kg/s	8.15	8.51	-4.23
Chamber	Pressure, MPa	3.07	3.07	0.00
	Temperature, K	2635	2635	0.00
	Flow rate, kg/s	8.15	8.51	-4.23

that of SNRE. Therefore, a higher flowrate is required through the same number of tie tubes in order to produce the required energy increase. As shown in Eq. 5.7, holding all else the same, an increase in flow rate would increase the pressure change in the tie tube element. Interestingly, the core inlet temperature is actually lower for the BNTR model than the SNRE design. This means that the BNTR model predicts a higher reactor heat addition.

The hydrogen flow rates leaving the tank and entering the chamber are within about 5% of the SNRE design. These flow rates are driven by the engine thrust design, and since the BNTR model exactly matches the thrust and chamber temperature and pressure, the flow rates should be nearly the same as well.

7.1.1.2 Reactor Level Details

This section presents the detailed results that have been produced by the 1-D fuel element and tie tube component analyses. Figure 7.2 is a plot of the axial power distribution as well as the propellant, channel wall, and peak internal fuel temperatures of the fuel element experiencing peak heating within the reactor. The reactor is designed such that the propellant temperature distribution is uniform across the reactor, but the channel wall and peak internal fuel temperatures will be highest for the hottest element. As shown in Fig. 7.2, the propellant enters the cold end of the reactor (axial position of 0) at approximately 300 K. The propellant then heats continually across the reactor, reaching a peak temperature of 2635 K at the exit. The internal fuel temperature, on the other hand, reaches a maximum inside the

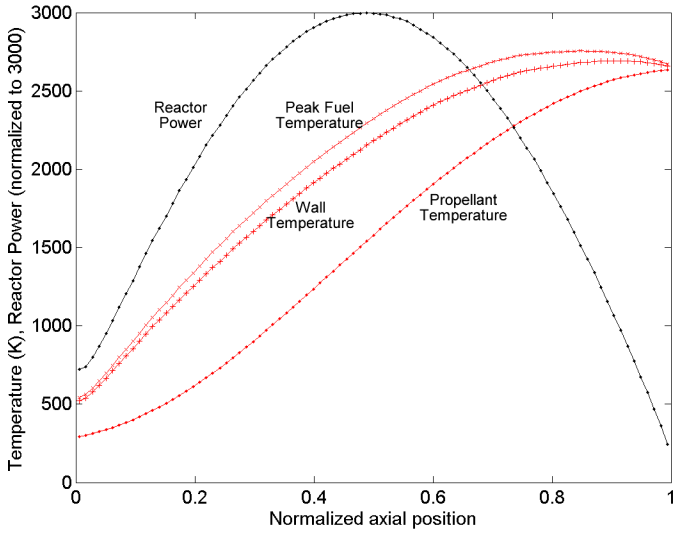

Figure 7.2: Fuel element axial temperature distribution for SNRE design point.

reactor, at approximately 82% of the reactor length. The axial power distribution is the reason for the differences in these peaks; the propellant temperature is based on the integrated heating across the entire element, while the fuel element temperature depends more strongly on the internal heating, which tapers off at the aft end of the element. The channel wall temperature follows the same trend as the internal temperature, but is slightly cooler as it is in direct contact with the hydrogen propellant.

Figure 7.3 is a plot of the tie tube coolant temperature distribution along the supply and return channels. As illustrated here, the coolant enters the tie tube at the left end at 25 K and warms to 52 K on its first pass. Then, the coolant reverses and returns for a second pass moving back up the return channel, exiting at a temperature of 214 K. From this figure, it is evident that the majority of the tie tube heating occurs in the return channel.

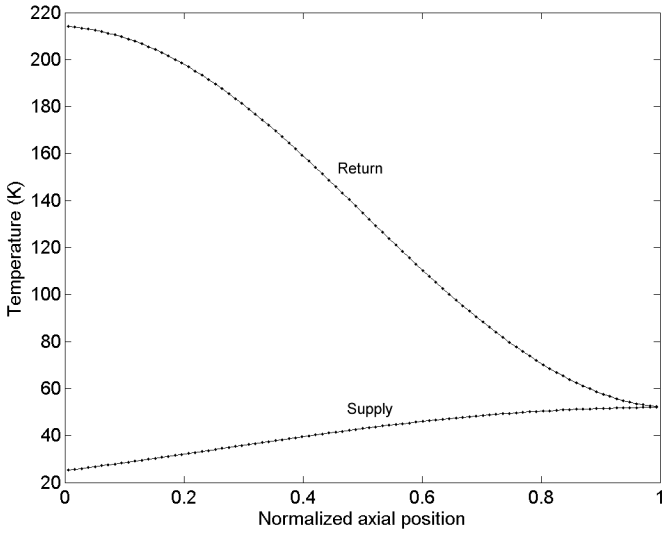

Figure 7.3: Tie tube coolant axial temperature distribution for SNRE design point.

Finally, Fig. 7.4 illustrates the reason that the tie tube coolant temperature increases more in the return channel than in the supply. The tie tube heat transfer is dominated by conduction from the adjacent fuel elements, and majority of the tie tube heat remains outside of the return channel, specifically in the graphite and ZrC layers. As such, very little heat conducts to the center of the tie tube, and the coolant temperature remains relatively constant along the supply channel. This occurs because graphite and ZrC, by design, have a low conductivity and act as insulators. The effect of heat generation can be seen in the "hot-spot" at the upper-right hand portion of the inner tie-tube. Here, the wall temperature is higher from the relatively high coolant exit temperature. Along the entire moderator layer, which is the thickest layer (shown from radii of 0.0025–0.006 m), there is a slight radial profile in the material temperature, which is caused by the heat generation within that layer. Without generation, the temperature would drop off steadily from

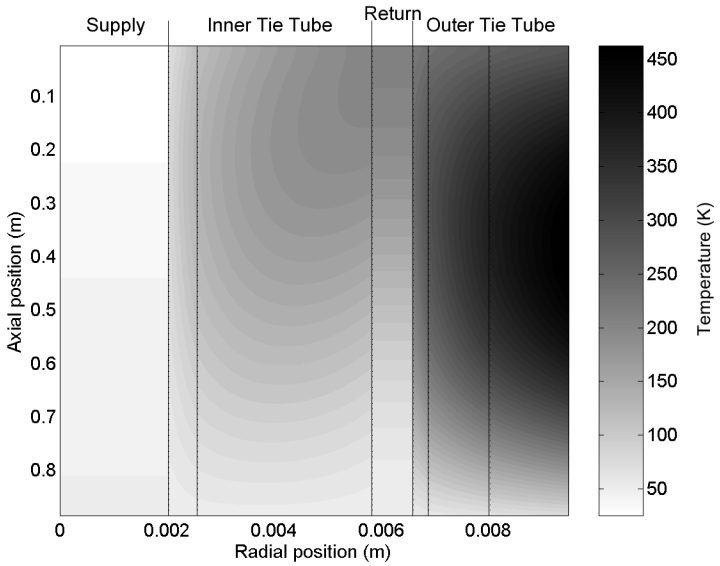

Figure 7.4: Tie tube wall axisymmetric temperature distribution for SNRE design point.

the outer to inner radii.

7.1.2 DRM Case Study 1

7.1.2.1 Engine-Level Performance

As discussed in the previous chapter, the first DRM case study is the non-bimodal NTR discussed in Ref. [45]. This engine is closest to the baseline thrust and chamber conditions, producing 66.7 kN of thrust with a chamber temperature and pressure of 2700 K and 6.89 MPa. Thermodynamic state data from the BNTR model for this design point are illustrated in Fig. 7.5. As with the SNRE, the compressor and turbine efficiencies from Case Study 1 have been input into this model, but there was no attempt to match the shaft speed as the compressor and turbine maps are not the same. The model could not converge with the low compressor and turbine

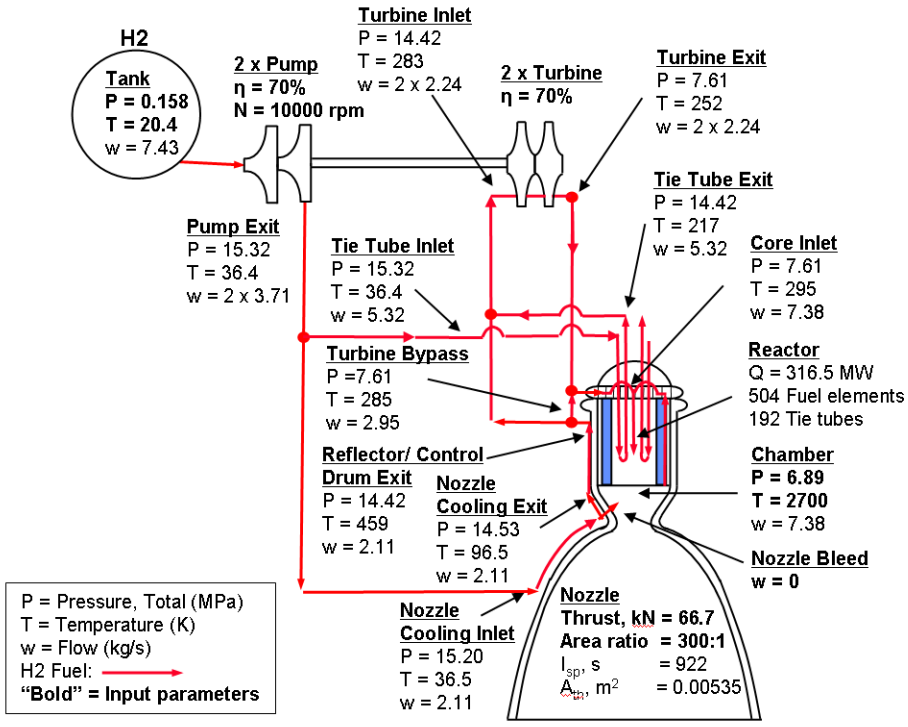

Figure 7.5: Detailed thermodynamic results for DRM Case Study 1. Engine diagram courtesy of Stan Borowski.

efficiencies (64.4% and 67.9%, respectively) of the original Case Study 1 assumptions. The closest values that could work are 70% efficiency for each component. These values are relatively low for a hydrogen turbopump system, so this limitation should not be a problem for other designs. The nozzle design for DRM Case Study 1 is quite different from that of SNRE, as evident in the engine performance. This engine is designed for more than twice the chamber pressure, a slightly higher chamber temperature, larger nozzle area ratio, and slightly lower thrust. Taken together, these changes results in an engine with a specific impulse above 920 s and nozzle throat area less than half of that of the SNRE. The combination of a smaller throat area and larger area ratio leads to a nozzle exit area (and thus overall size) that is only 23% larger.

Table 7.2 presents the difference in engine component performance between the original DRM Case Study 1 design and the results of the BNTR model. The results are very similar to that of the SNRE design point. The tank and chamber conditions are matched exactly, but the coolant pressure inside the engine is significantly higher in the BNTR model. Once again the source of this discrepancy is that the reactor heats more effectively and the tie tubes heat less effectively in the BNTR model.

Another significant difference is that the tie tube flow rate is 25% higher in the BNTR model, while the nozzle cooling jacket flow rate is 35% lower. One important consideration in this comparison is that the nozzle - tie tube cooling split is solved for directly with the BNTR model, while it is a user-specified assumption in NESS (which is the source of the numbers in Ref [45]). With that in mind, this particular discrepancy may not be a concern.

7.1.2.2 Reactor-Level Details

As in the SNRE results, Fig. 7.6 shows the reactor power and temperatures as a function of axial position. The trends here are identical to those shown before, with some variation in the magnitudes. The normalized power distribution is identical, although the magnitude of the power seen by the engine is lower for this design point. For this engine, the propellant exit temperature is 2700 K and the peak fuel temperature is 2830 K. The location of peak heating once again appears to be at approximately 82% of the reactor length.

The tie tube coolant, as shown in Fig. 7.7, also demonstrates the same trends

Table 7.2: Difference between DRM Case Study 1 results from BNTR model and design from Ref. [45].

Component	Properties	BNTR Model	Case 1	Δ, %
Engine	Specific impulse, s	933	911	2.41
	Reactor power, MW	317	313	1.12
Tank	Pressure, MPa	0.158	0.158	0.00
	Temperature, K	20.4	20.4	0.00
	Flow rate, kg/s	7.43	7.51	-1.07
Pump Exit	Pressure, MPa	15.32	11.78	30.05
	Temperature, K	36.4	35.2	3.41
	Flow rate, kg/s	3.71	3.75	-1.07
Tie Tube Inlet	Pressure, MPa	15.32	11.78	30.05
	Temperature, K	36.4	35.2	3.41
	Flow rate, kg/s	5.32	4.27	24.59
Tie Tube Exit	Pressure, MPa	14.42	9.68	48.97
	Temperature, K	217	506	-57.11
	Flow rate, kg/s	5.32	4.27	24.59
Nozzle Cooling Inlet	Pressure, MPa	15.20	11.40	33.33
	Temperature, K	36.5	35.2	3.69
	Flow rate, kg/s	2.11	3.24	-34.88
Turbine Inlet	Pressure, MPa	14.42	9.68	48.97
	Temperature, K	283	419	-32.46
	Flow rate, kg/s	2.24	2.86	-21.68
Core Inlet	Pressure, MPa	7.61	7.49	1.60
	Temperature, K	295	385	-23.38
	Flow rate, kg/s	7.38	7.12	3.65
Chamber	Pressure, MPa	6.89	6.89	0.00
	Temperature, K	2700	2700	0.00
	Flow rate, kg/s	7.38	7.51	-1.73

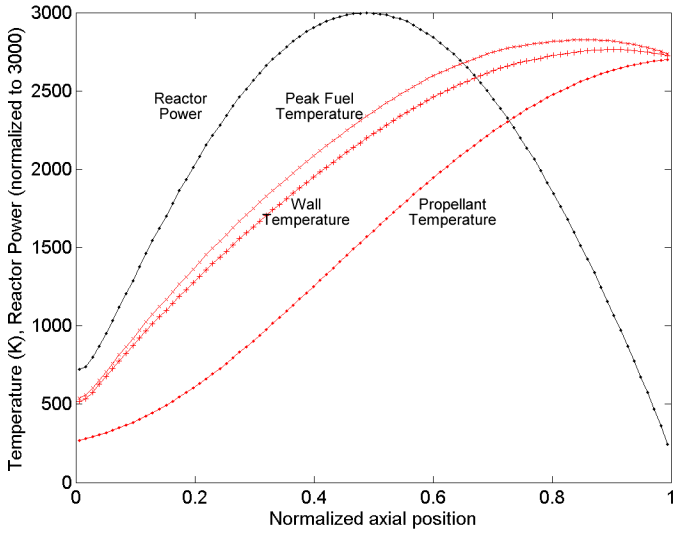

Figure 7.6: Fuel element axial temperature distribution for DRM Case Study 1.

in DRM Case Study 1 as those seen for the SNRE. The inlet and exit temperatures here are slightly higher, nearly 40 K into and 220 K leaving the tie tubes. Once again it is evident that the majority of the tie tube heating occurs in the outer portion of the element, due to fuel element conduction.

Figure 7.8 confirms that the fuel element conduction also dominates the tie tube heating for Case Study 1. Although the coolant leaves the return channel at a temperature of 220 K (as verified in Fig. 7.7), the outer wall material has a peak temperature of approximately 450 K. As in the DRM design point, the effects of heat generation can be seen in the thick moderator layer of the inner tie tube.

7.1.3 DRM Case Study 2

The second DRM case study allows the examination of both the propulsion and power generation modes of the BNTR model. The propulsion results, following

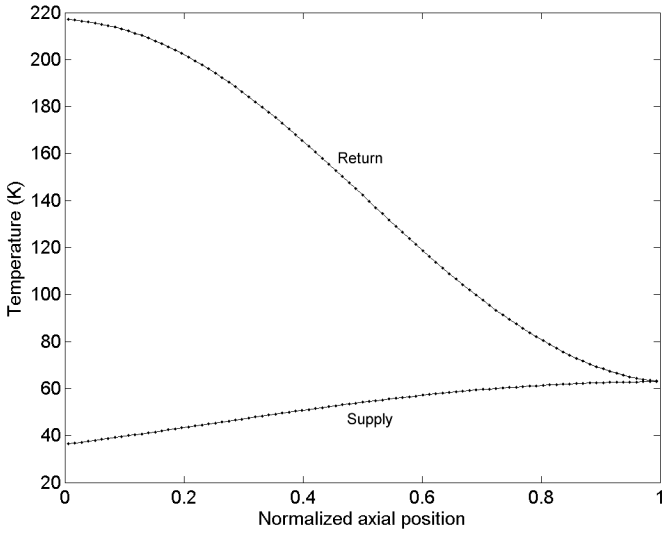

Figure 7.7: Tie tube coolant axial temperature distribution for DRM Case Study 1.

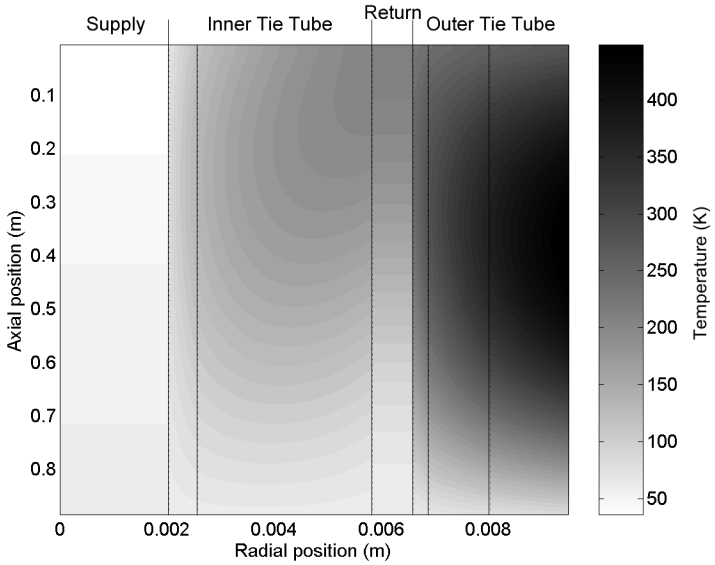

Figure 7.8: Tie tube wall axisymmetric temperature distribution for DRM Case Study 1.

the format of the above design points, will be presented first, followed by the power generation results.

7.1.3.1 Propulsion Operation

Figure 7.9 shows the state point thermodynamics results for the DRM Case Study 2 engine in propulsion-mode operation. The main differences between this and the previous engines are the nozzle area ratio (200:1 here), chamber conditions (2556 K, 5.40 MPa), and pump and turbine efficiencies (82% and 90%, respectively). The lower chamber temperature leads to a lower specific impulse, while the lower chamber pressure and nozzle area ratio require a slightly higher flow rate and larger nozzle to produce the same thrust as Case Study 1. The remaining parameters are illustrated in Fig. 7.9 and listed, with a comparison to the originally published results, in Table 7.3.

As shown in table 7.3, beyond the tank and chamber, the pressure, temperature, and flow rate are widely different between the BNTR model and results of Ref. [22]. Although the calculated engine/nozzle performance matches within 5%, the breakdown of the flows between the engine components shows large discrepancies. The main reason for this discrepancy is that the engine design in Case Study 2 uses a flow path with many additional flow splits and crossovers than what is assumed in the BNTR model layout. As shown in Fig. 6.7, the pump exit flow from Ref. [22] actually splits into three separate flow legs, cooling the nozzle, tie tubes, and reflector separately. Additionally, from the various valves and connections past

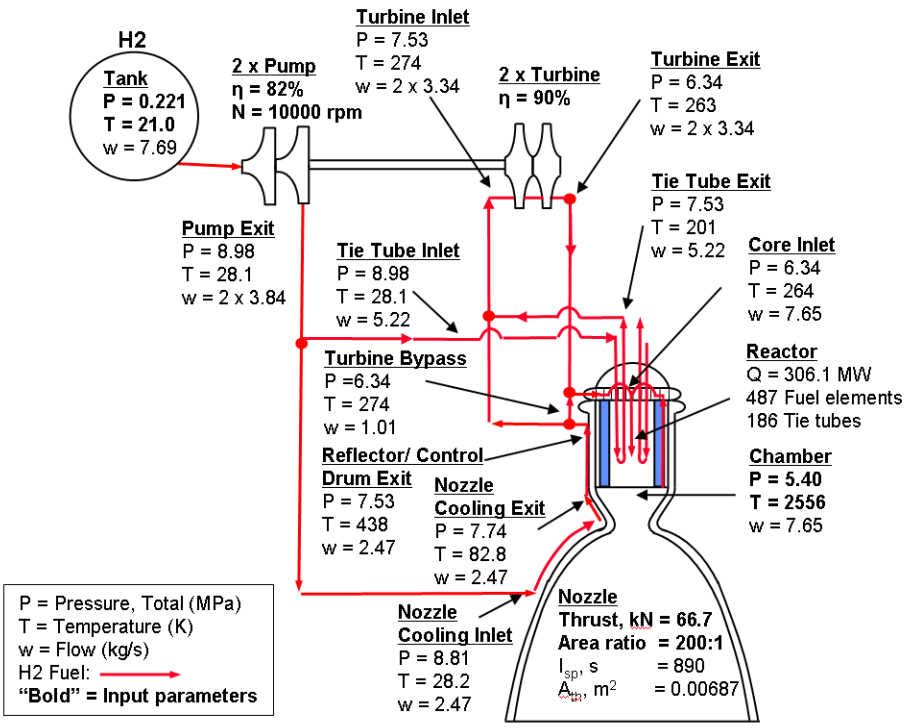

Figure 7.9: Detailed thermodynamic results for DRM Case Study 2. Engine diagram courtesy of Stan Borowski.

the exits of these cooling flows, the conditions of the flow entering the reactor core are not clear.

Ultimately, this comparison (as well as the ones above) shows that the BNTR model can closely match the overall flow rate and nozzle design and performance for any design point. In order to match the thermodynamic properties at the component level, however, the BNTR model must be refined to model each flowpath exactly.

Figures 7.10, 7.11, and 7.12 once again illustrate the temperature distributions of the fuel element, tie tube coolant, and tie tube walls, respectively. The trends are once again similar to the previous design points, but the magnitudes of the temperatures are lower here, corresponding to the lower chamber temperature, and thus, reactor power.

Table 7.3: Difference between DRM Case Study 2 propulsion-mode results from BNTR model and design from Ref. [22].

Component	Properties	BNTR Model	Case 2	Δ, %
Engine	Specific impulse, s	890	864	3.00
	Throat area, m2	0.00687	0.00710	-3.20
	Reactor power, MW	306.1	313	-2.20
Tank	Pressure, MPa	0.221	0.221	0.00
	Temperature, K	21.0	21.0	0.00
	Flow rate, kg/s	7.69	7.88	-2.41
Pump Exit	Pressure, MPa	8.98	15.16	-40.77
	Temperature, K	28.1	36.9	-23.85
	Flow rate, kg/s	3.84	3.94	-2.54
Tie Tube Inlet	Pressure, MPa	8.98	14.86	-39.57
	Temperature, K	28.1	37.1	-24.26
	Flow rate, kg/s	5.22	3.94	32.49
Tie Tube Exit	Pressure, MPa	7.53	14.10	-46.60
	Temperature, K	201	1021	-80.31
	Flow rate, kg/s	5.22	3.94	32.49
Nozzle Cooling Inlet	Pressure, MPa	8.81	14.86	-40.71
	Temperature, K	28.2	37.1	-23.99
	Flow rate, kg/s	2.47	1.578	56.53
Turbine Inlet	Pressure, MPa	7.53	13.68	-44.96
	Temperature, K	274	606	-54.79
	Flow rate, kg/s	3.34	1.420	135.21
Core Inlet	Pressure, MPa	6.34	N/A	
	Temperature, K	264	N/A	
	Flow rate, kg/s	7.65	N/A	
Chamber	Pressure, MPa	5.41	5.41	0.00
	Temperature, K	2556	2560	-0.16
	Flow rate, kg/s	7.65	7.87	-2.80

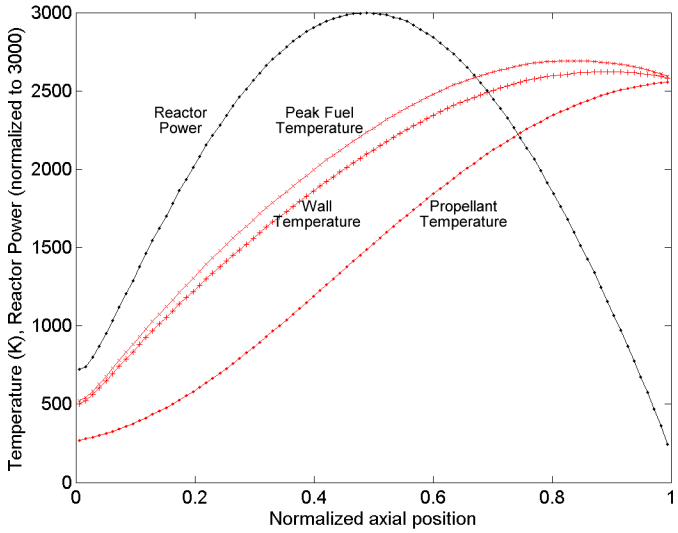

Figure 7.10: Fuel element axial temperature distribution for DRM Case Study 2.

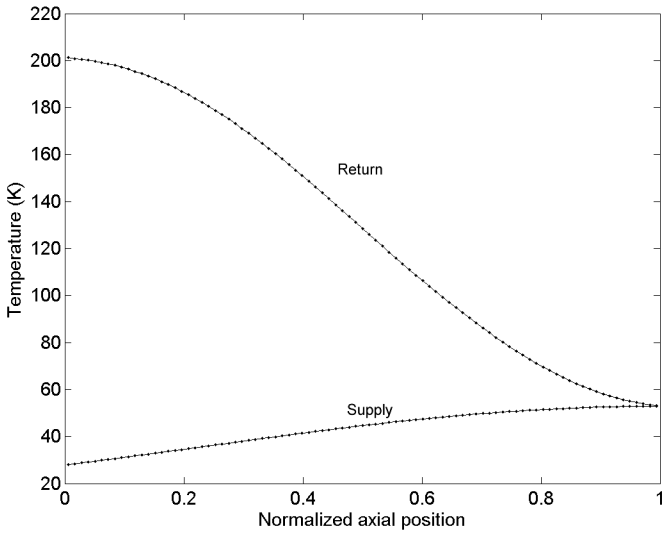

Figure 7.11: Tie tube coolant axial temperature distribution for DRM Case Study 2.

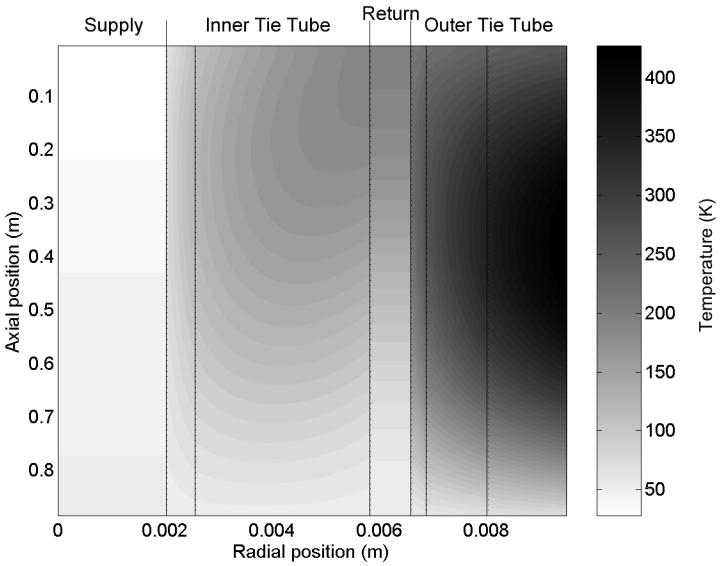

Figure 7.12: Tie tube wall axisymmetric temperature distribution for DRM Case Study 2.

7.1.3.2 Power Operation

The power-mode operation for the DRM Case Study 2 design point was calculated using the Brayton cycle portion of the BNTR model, with a reactor size of 186 tie tubes, as determined by the propulsion analysis. One problem encountered while trying to run this power-mode design point is that the BNTR model could not produce converged results with the same input conditions as those in Ref. [22]. The BNTR model has demonstrated a high pressure drop across the tie tubes during power generation, which in this case, requires a higher compressor inlet pressure and pressure ratio to produce a balanced engine. For the results shown here, the pressure ratio and compressor inlet pressure are increased 2.2 and 2.41 MPa, respectively. This is in contrast to the original study, which assumes a pressure ratio of 1.9 and inlet pressure of 0.543 MPa. The detailed thermodynamics results throughout the engine for this mode of operation are illustrated in Fig. 7.13.

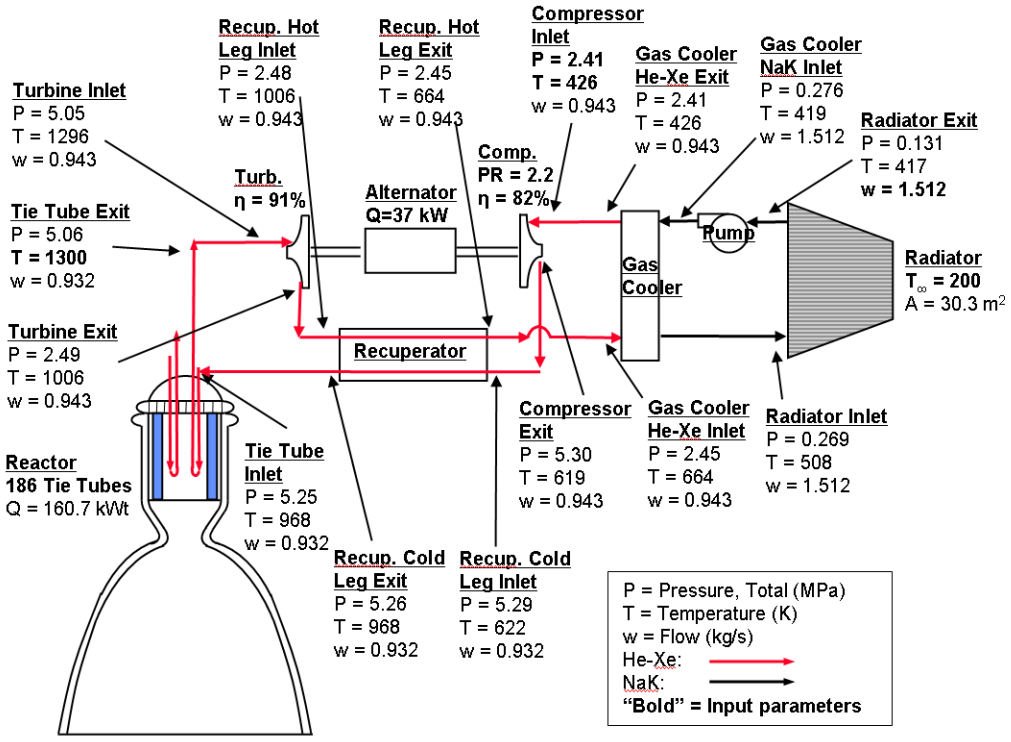

Figure 7.13: Detailed thermodynamic results for DRM Case Study 2.

Table 7.4 presents the difference in power-mode operation between the original DRM Case Study 2 design and the results of the BNTR model. At the cycle level, both are able to produce 37 kWe power at nearly the same reactor power (and thus conversion efficiency). The required reactor power for the BNTR model is 161 kWt, which is less than 3% lower than that of the Case Study 2 design. The radiator area, on the other hand, is nearly 40% smaller for the BNTR model, but the heat rejection loop results are not given in the Case Study 2 design, so the reason for this discrepancy is unclear.

The most striking difference between the two models is that the pressure differs by approximately 400% throughout the He-Xe loop. This, of course, is due to the higher required pressure ratio and compressor inelt pressure, as discussed above. The

Table 7.4: Difference between DRM Case Study 2 power-generation results from BNTR model and design from Ref. [22].

Component	Properties	BNTR Model	Case 2	Δ ,%
Reactor	Power, kWt	161	165	-2.61
Radiator	Area, m2	30.3	50.1	-39.52
Compressor Inlet	Pressure, MPa	2.41	0.542	344.65
	Temperature, K	426	426	0
	Flow rate, kg/s	0.943	1.224	-22.96
Recup. Cold Leg Inlet	Pressure, MPa	5.29	1.03	414.09
	Temperature, K	622	578	7.61
	Flow rate, kg/s	0.932	1.20	-22.40
Tie Tube Inlet	Pressure, MPa	5.25	1.02	412.70
	Temperature, K	968	912	6.14
	Flow rate, kg/s	0.932	1.20	-22.398
Turbine Inlet	Pressure, MPa	5.05	1.015	397.54
	Temperature, K	1296	1280	1.25
	Flow rate, kg/s	0.943	1.201	-21.48
Recup Hot Leg Inlet	Pressure, MPa	2.48	0.558	344.44
	Temperature, K	1006	1022	-1.57
	Flow rate, kg/s	0.943	1.224	-22.96
Gas Cooler He-Xe Inlet	Pressure, MPa	2.45	0.556	340.65
	Temperature, K	664	691	-3.91
	Flow rate, kg/s	0.94	1.22	-22.96

temperatures throughout the engine match within 8% for all of the components, so although the BNTR model requires a higher cycle pressure, the overall operation appears to be very similar.

The final significant difference between the BNTR model results and those from Ref. [22] is that the He-Xe mass flow rate throughout the BNTR model is about 23% lower than that of the original Case Study 2 design. The cause of this discrepancy is unclear.

Figure 7.14 is a plot of the tie tube coolant temperature distribution along

the supply and return channels for power-mode operation. From this figure, it is immediately apparent that tie tube operation during power-generation is drastically different from that in propulsion-mode. First of all, the tie tube He-Xe coolant enters at nearly 1000 K and exits at 1300 K — a 600% increase in exit temperature from propulsion operation! Even more interesting, though, is the fact that the peak tie tube coolant temperature actually occurs halfway down the return channel, and that the coolant temperature where the supply and return channels meet is nearly 1650 K, much higher than the inlet or exit temperatures.

The high tie tube temperatures are caused by the power-mode design point, which specifies a tie tube outlet temperature equal to the turbine inlet temperate limit, which is assumed to be 1280 K here. It is common to drive a traditional Brayton cycle to the turbine inlet temperature limit, but for the BNTR and its low tie tube heat transfer, doing so constrains the tie tubes to operate at a much higher temperature.

Furthermore, during power-mode operation, all tie tube heating comes from heat conduction at the outer layer, and heat is no longer being generated in the moderator layer between the two coolant channels. The net result is that the return coolant channel actually transfers heat into the moderator layer as it moves back towards the top of the element. That heat is then transferred through the moderator to the supply channel, helping to heat to coolant on its first pass. This effect is dramatic near the inlet/exit of the tie tube because the external heating distribution is nearly zero at this location. The location of peak temperature in the return channel corresponds to the location of peak heating in the power profile that is used

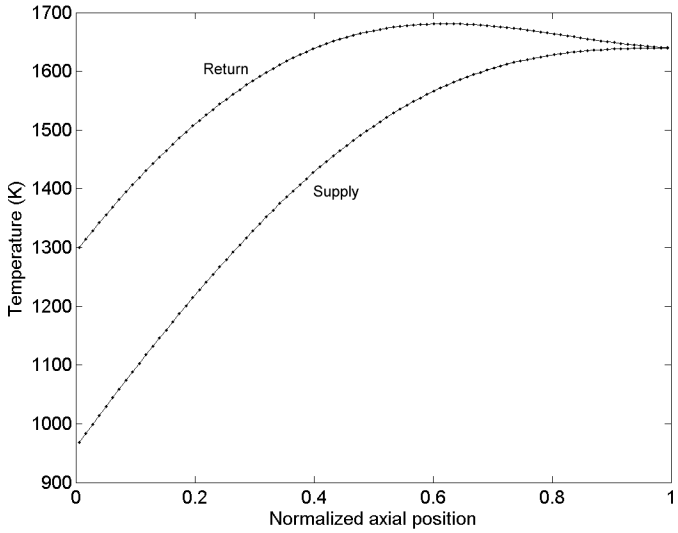

Figure 7.14: Tie tube coolant axial temperature distribution for DRM Case Study 2.

in this model.

Figure 7.15 further illustrates this point by showing the temperature distribution in the tie tube layers as a function of radial and axial position. From this figure, it is clear that the peak heating occurs at the outer layer of the tie tube, especially from about 0.5–0.6 m from the inlet/exit plane. This is the location of peak coolant temperature indicated in the previous figure. An examination of the temperature distribution in the various material layers shows that the temperature of each layer increases from the inlet/exit plane down to the middle, further illustrating the reason that the minimum coolant temperature in both the supply and return channels occurs at the inlet/exit plane.

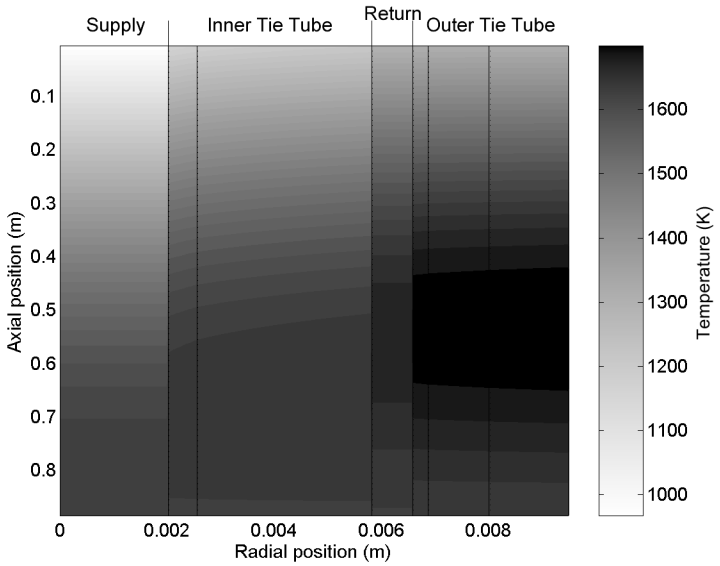

Figure 7.15: Tie tube wall axisymmetric temperature distribution for DRM Case Study 2.

7.1.4 Baseline BNTR Design

The above case studies contain some assumptions that are either not realistic or do not properly correspond the engines required for DRM 4.0. As such, a baseline BNTR design point has also been run in order to combine the most common, realistic design parameters. The propulsion-mode assumes a design thrust of 66.7 kN, chamber temperature and pressure of 2700 K and 6.89 MPa and compressor and turbine efficiencies of 72% and 80%, respectively. The power-mode will be designed for 16.7 kWe power nominal operation, 25 kWe for engine-out, with a turbine inlet temperature of 1150 K and compressor and turbine efficiencies of 80% and 85%, respectively. The compressor pressure ratio and inlet pressure will be varied in order to determine the optimal conversion efficiency.

7.1.4.1 Propulsion Operation

Figure 7.16 shows the detailed component results for the propulsion-mode operation of the baseline design point. The results here are very similar to those shown in DRM Case Study 1, as the only difference is more optimistic assumptions of pump and turbine efficiency. The total hydrogen flow-rate is 7.51 kg/s, with 69% of that going to the tie tubes, and 31% to the nozzle cooling jacket. With a large amount of turbine bypass, nearly 76% of the total flow goes to the fuel pumps, and very little of the control drum cooling flow going directly to the reactor. This engine also assumes 0.08 kg/s of nozzle bleed flow, which reduces the specific impulse slightly by diluting the reactor exit temperature, but makes the engine model easier to balance.

The reactor requires a thermal power level of 316.5 MW to produce 66.7 kN of thrust at a chamber temperature of 2676 K (2700 K leaving the reactor). This corresponds to 500 fuel elements and 190 tie tubes. Overall, this engine is smaller than the SNRE due to the lower thrust and power, slightly smaller than Case Study 1 due to the higher turbopump efficiency, and marginally larger than the Case Study 2 engine due to the higher chamber temperature and lower turbopump efficiency.

Figures 7.17, 7.18, and 7.19 show the fuel element and tie tube temperature distributions for propulsion-mode operation of the baseline BNTR. Due to the similarity of the baseline engine to the other design points, the trends and results here are nearly the same as those shown previously.

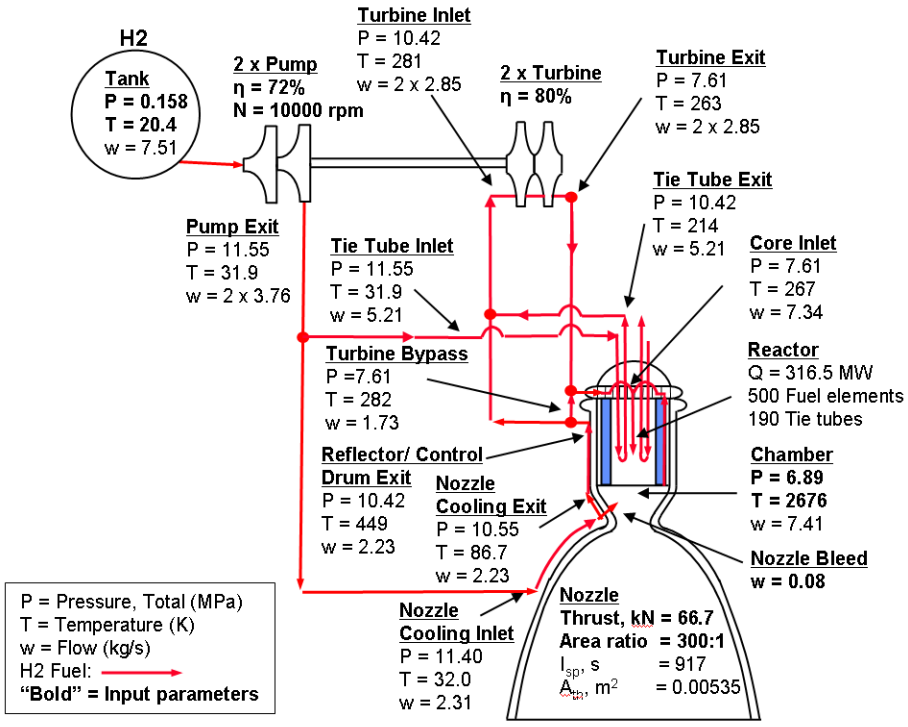

Figure 7.16: Detailed thermodynamic results for propulsion mode of BNTR baseline design point. Engine diagram courtesy of Stan Borowski.

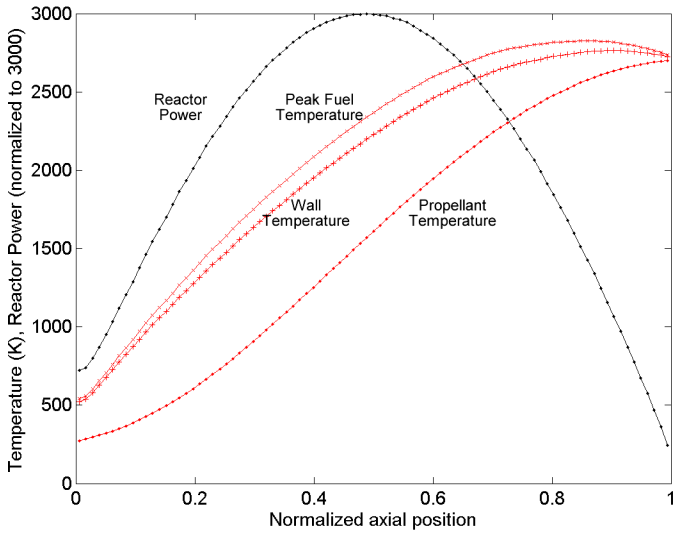

Figure 7.17: Fuel element axial temperature distribution for baseline propulsion-mode operation.

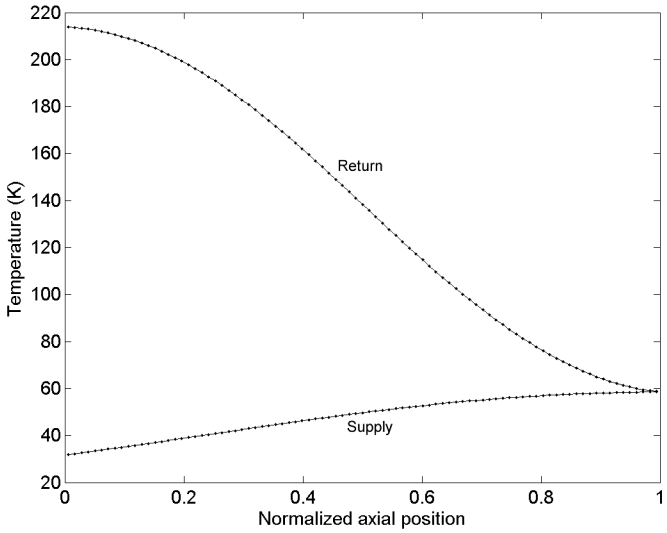

Figure 7.18: Tie tube coolant axial temperature distribution for baseline propulsion-mode operation.

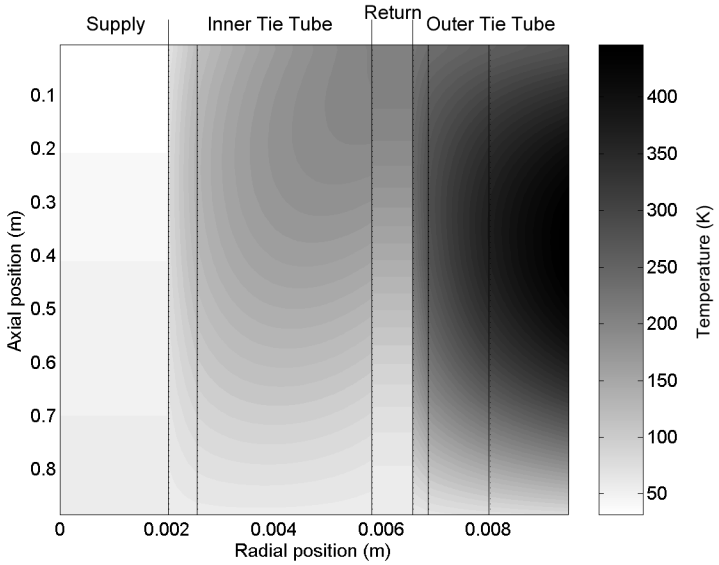

Figure 7.19: Tie tube wall axisymmetric temperature distribution for baseline propulsion-mode operation.

7.1.4.2 Power Operation

The following three figures show the results of nominal power-mode operation of the baseline BNTR engine design. As discussed previously, each Brayton cycle unit nominally operates at an output power of 16.7 kWe. Figure 7.20 shows the detailed engine-level results for this design point. The compressor inlet pressure and pressure ratio have been set to 2.41 MPa and 2.2, as that was found to produce nearly optimal performance with reasonable computation time. As the output power is only 16.7 kWe, this engine only requires a He-Xe flow rate of 0.499 kg/s, nearly half that of the DRM Case Study 2 design. The radiator area here is actually larger than that of Case Study 2, however, because the radiator inlet temperature is much lower, requiring a larger area to reject an even smaller amount of waste heat. The connection between radiator temperature and area is shown in Eq. 7.1, which restates the Stefan-Boltzmann law originally shown in Eq. 4.43. The rate of radiation heat transfer scales with the fourth-power of radiator temperature but is linear with area, so even a small decrease in temperature will require a large increase in area to maintain the same level of heat rejection.

$$Q = \epsilon \sigma A \left(T^4 - T_\infty^4 \right) \tag{7.1}$$

Figure 7.21 is a plot of the tie tube coolant temperature distribution along the supply and return channels. This figure demonstrates the same trends seen in the Case Study 2 design point results. The minimum temperature in the supply and return channels occurs at the inlet/exit plane, with peak values near 70% of the elements length. The baseline turbine inlet temperature is only 1150 K, so the peak

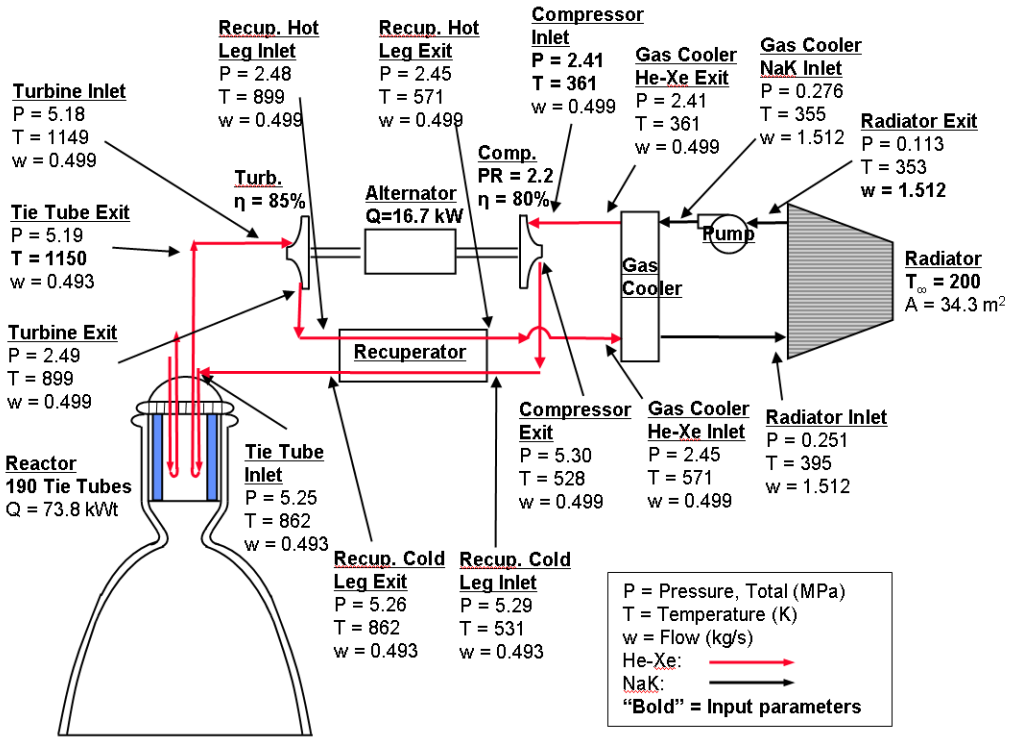

Figure 7.20: Detailed thermodynamic results for propulsion mode of BNTR baseline design point.

coolant temperature is lower here than in the Case Study 2 engine.

The same tie tube response is shown in Fig. 7.22. The baseline BNTR follows the same trends as the results of DRM Case Study 2, but at a slightly lower temperature. The peak tie tube element temperature is approximately 1550 K here, and again occurs at an axial position located 70% down the element length.

7.1.4.3 Power Operation - Engine Out

The preceding case assumes that all three Brayton engines are operating nominally at 16.7 kWe each, but the DRM specifies that the engines will be rated for 25 kWe, so that the remaining two can produce the required 50 kWe in the case of an engine failure. The following presents the results of the BNTR power model for 25

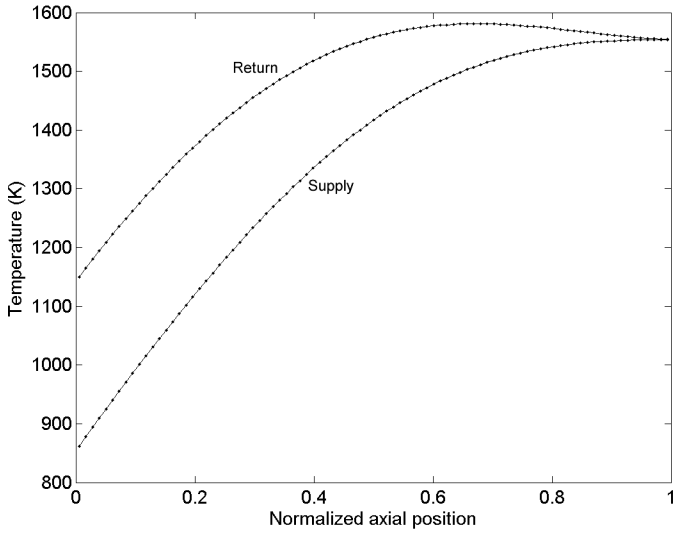

Figure 7.21: Tie tube coolant axial temperature distribution for baseline propulsion-mode operation.

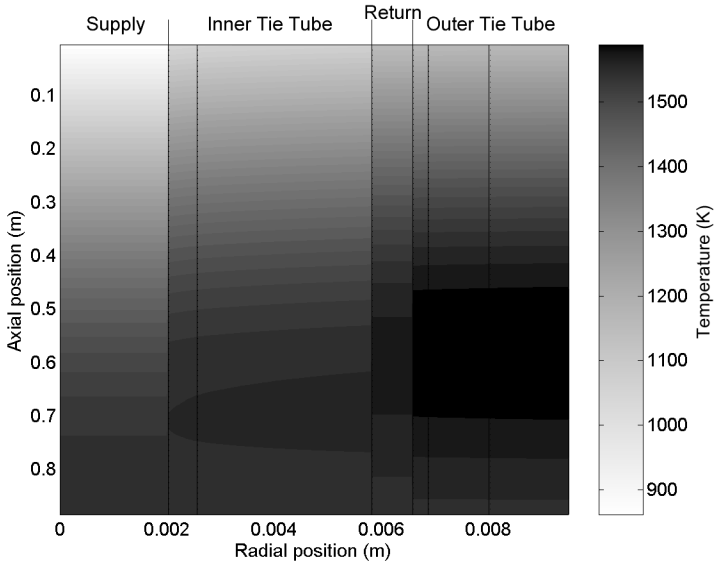

Figure 7.22: Tie tube wall axisymmetric temperature distribution for baseline propulsion-mode operation.

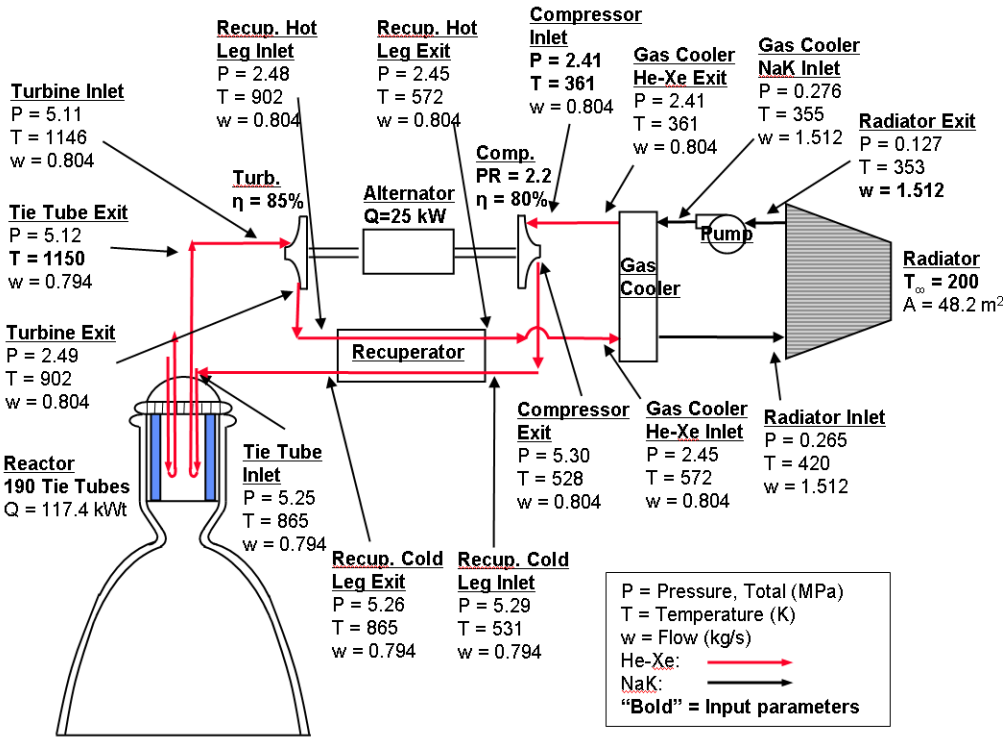

Figure 7.23: Detailed thermodynamic results for propulsion mode of BNTR baseline design point under engine-out conditions.

kWe, engine-out operation.

Figure 7.23 shows the Brayton cycle response to engine-out design point operation. The compressor inlet temperature and pressure are assumed to remain the same as the nominal case so the majority of the component parameters are unchanged. The main changes requires to run at an output power of 25 kWe are a He-Xe flow rate increase to approximately 0.80 kg/s, reactor power increase to 117.4 kWt, and a radiator area increase to 48.2 square meters. The reactor power increase also corresponds to a conversion efficiency decrease from 22.6% to 21.3%. As the reactor is rated to run at more than 300 MWt for propulsion, the primary concern of designing for engine out operation is the radiator size.

An examination of Fig. 7.24 shows that although the tie tube inlet and exit

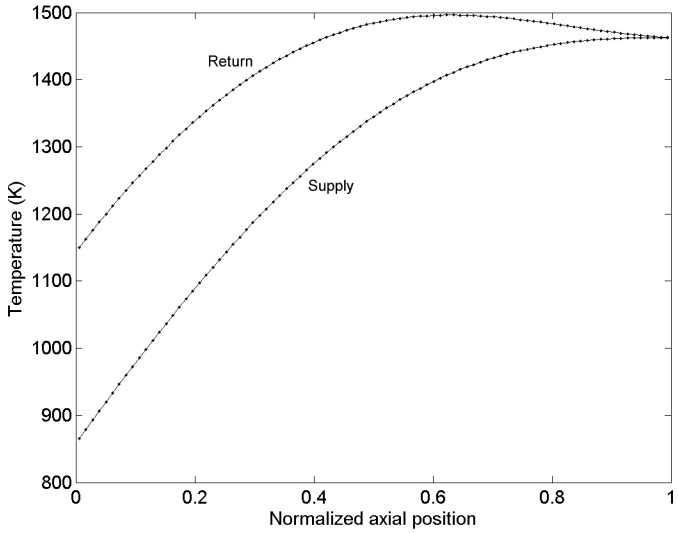

Figure 7.24: Tie tube coolant axial temperature distribution for baseline propulsion-mode with engine-out operation.

temperatures are nearly the same for nominal and engine out operation, the peak He-Xe temperature is almost 100 K cooler for the higher power engine-out case. This temperature decrease, although initially unintuitive, is due to the He-Xe flow rate increasing by nearly 80% in response to the reactor power increasing by 50%. As such, the additional He-Xe cools the reactor more effectively than was possible in the nominal design. Finally, Fig. 7.25 reinforces the point that the tie tube temperatures are lower during engine-out operation, showing a slightly lower peak material temperature of about 1500 K, as opposed to 1550 K before.

7.2 Trade Studies

As discussed previously, there is some variation in the assumed design parameters for BNTR engine systems. To investigate the impact of the parameters, a series

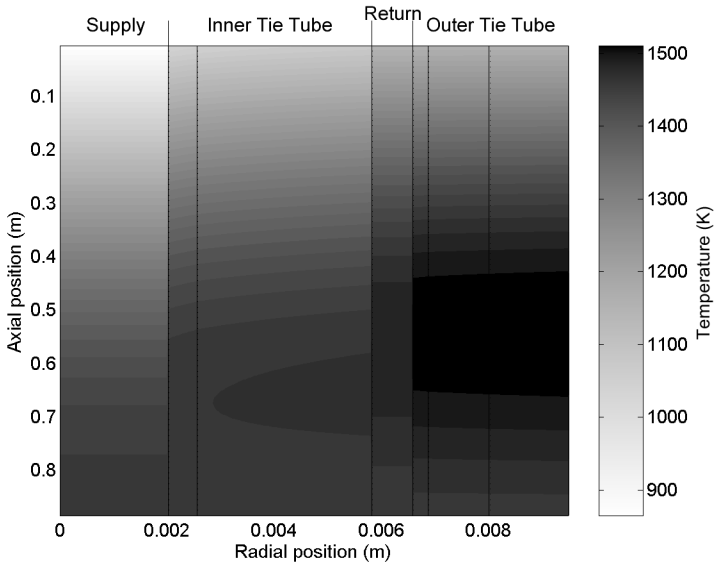

Figure 7.25: Tie tube wall axisymmetric temperature distribution for baseline propulsion-mode with engine-out operation.

of trade studies have been performed for both propulsion and power-generation operation.

7.2.1 Propulsion Trade Studies

7.2.1.1 Chamber Temperature and Pressure

The chamber pressures of the various BNTR studies vary from 3.45–13.8 MPa, while the reactor exit temperature can vary from 2300–3100 K, depending on the reactor material. As such, the effect of chamber temperature and pressure on engine performance has been examined. The propulsion results have been calculated for pressures varying from approximately 3.5–9.0 MPa and several fixed values of chamber temperature, ranging from 2300–3100 K by increments of 200 K. As chamber temperature decreases, the actual data lines on all of the following plots get shorter

because the lower temperature models could not converge at high pressures. Thus, even though DRM 4.0 assumes a chamber pressure of 13.8 MPa, the highest value possible with this model is 8.62 MPa from the 3100 K chamber temperature case.

Figure 7.26 shows the effect of chamber conditions on several engine-level parameters: reactor power, specific impulse, and throat area. The upper-left subplot shows that reactor power remains relatively constant with varying chamber pressure, but that each 200 K increase in chamber temperature requires the reactor power to increase by approximately 15 MWt in order to heat the coolant to that temperature.

The upper-right subplot shows nearly the same effect on specific impulse. Specific impulse drops off slightly with increasing chamber pressure, but increases greatly with chamber temperature. This follows ideal nozzle analysis presented earlier in Eq. 1.3. According to Fig. 7.26, specific impulse increases by even increments of approximately 40 s for each 200 K increase in chamber temperature.

The lower-left subplot of Fig. 7.26 shows that nozzle throat area is affected by chamber pressure only and is not dependent on chamber temperature. This makes sense, as the nozzle exit area must decrease to maintain constant pressure thrust with increasing chamber pressure. Although chamber temperature also affects the engine thrust, its impact is seen in the nozzle flow rate and momentum thrust, as will be discussed shortly.

Figure 7.27 shows the effect of chamber conditions on the mass flow-rate of hydrogen through the main coolant legs in the engine. The multiple lines in each subplot represent the different chamber temperature cases, as labeled on the plot. The four subplots show the response of flow rate leaving the tank, entering the

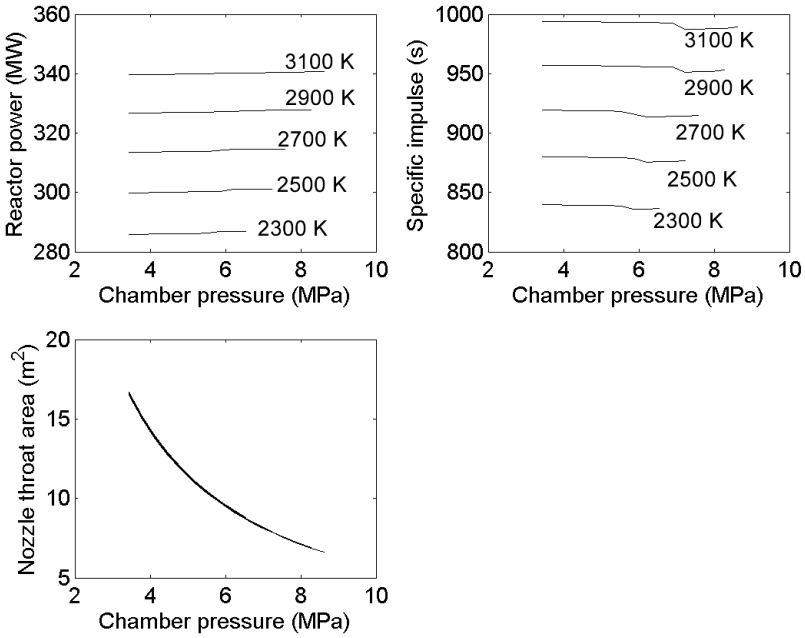

Figure 7.26: Sensitivity of engine-level parameters to chamber conditions.

nozzle cooling jacket, entering the tie tubes, and entering the reactor.

A comparison of the chamber temperature lines in each subplot shows that for all of the cases, higher chamber temperatures require lower flow rates throughout the engine. This occurs because lower chamber temperatures lead to lower exit velocity. Thus, for a given chamber pressure, the lower chamber temperature cases require a higher exit mass flow rate to produce the same thrust.

The upper-left and lower-right plots show that the total hydrogen leaving the tank, and that entering the reactor, are not impacted by changes in chamber pressure. The tie tube and nozzle cooling split, on the other hand, has a distinct response. As shown in the upper-right subplot of Fig. 7.27, the nozzle coolant decreases gradually with chamber pressures up to about 6 MPa, then suddenly drops by about 0.3 kg/s for each curve, then gradually increases again.

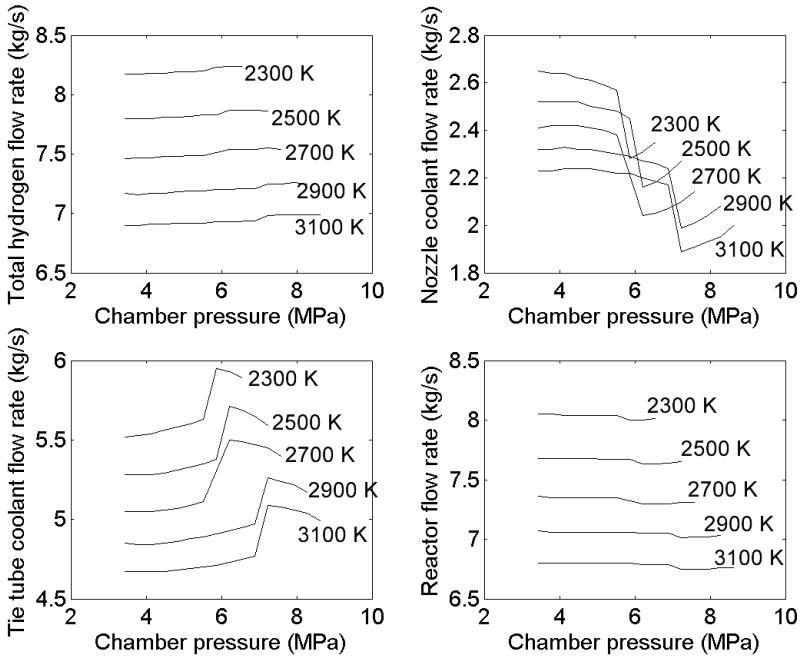

Figure 7.27: Sensitivity of engine flow rates to chamber conditions.

The tie tube coolant response (as shown in the lower-left subplot) indicates a complimentary response to that of the nozzle, discontinuously increasing the tie tube coolant to make up for the drop in nozzle coolant. The cause of this coupled response is that the tie tubes and nozzle cooling jacket represent two parallel flow paths within the engine, connecting the pump exit to the turbine inlet. As such, a relative increase in the flow resistance along one path increases the flow rate in the other leg to compensate. So, these results indicate that as chamber pressure increases, something happens to increase the flow resistance in the nozzle cooling jacket relative to that of the tie tubes, reducing the coolant flow rate in the nozzle and increasing it in the tie tubes.

The discontinuous nature of the response in Fig. 7.27 indicates that it is not the result of a natural phenomenon, but instead caused by some numerical aberration in

the solver. However, as the exact same trend occurs for all five chamber temperature values, this discontinuity is likely the result of a real response of the engine system, and not just solver error.

To examine the cause of the discontinuity, the 2700 K chamber temperature case has been examined in more detail, with the results plotted in Fig. 7.28. The upper-left subplot shows the pressures entering and leaving the pumps and turbines in the engine. It is clear that at the location of the discontinuity, the pump exit pressure and turbine inlet pressure both increase twofold. The pump inlet and turbine exit pressures, however, increase only gradually. This corresponds well with the previous results that the discontinuity occurs only in the interior components of the engine. In general, this plot indicates that, for chamber pressures below approximately 5.5 MPa, the engine can operate with a pump exit pressure double that of the chamber. For chambers pressures above 5.5 MPa, though, the turbopump can no longer balance at the lower pump exit pressures. The discontinuity is thusly caused by the solver jumping to a higher pump pressure design that can balance with the turbine while providing the required chamber pressure.

The other three subplots in Fig. 7.28 show the cascading results of jumping to the new pressure design. The upper-right shows that the temperature change across the turbine is now greater, so its mass flow is lower. As shown in the lower-right, in response to the lower turbine mass flow requirement, the turbine bypass valve flow increases substantially. And finally, to provide turbine inlet and exit temperatures that appropriately balance the turbine with the rest of the engine, the tie tube flow rate must increase while the control drum flow rate decreases. It is this final effect

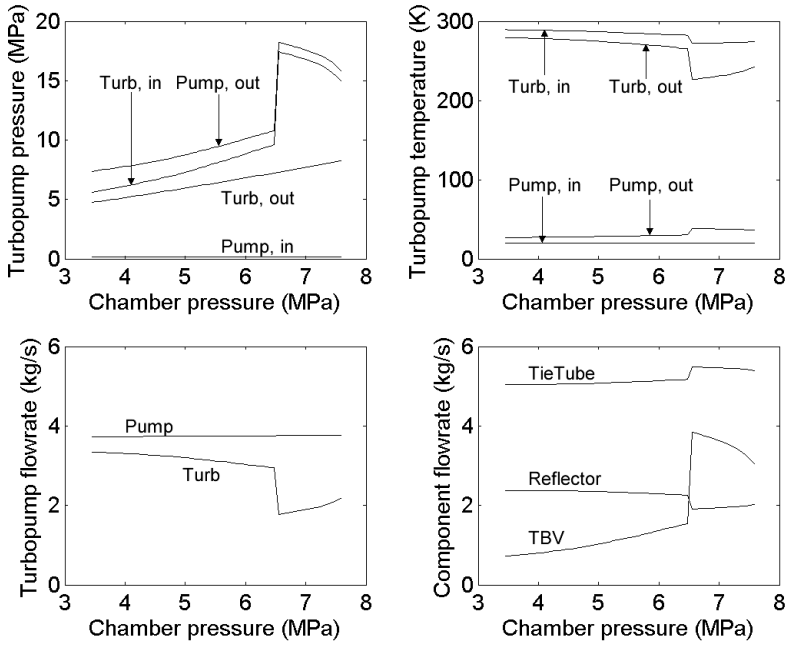

Figure 7.28: Turbopump operation for the 2700 K chamber temperature case.

that is evident in the nozzle and tie tube cooling split of Fig. 7.27.

Continuing the examination of the general impact of the chamber conditions, Fig. 7.29 shows the effect on the size of the reactor core, as illustrated by the number of fuel elements and tie tubes. The required number of fuel elements, as shown in the left-hand figure, remains relatively flat with varying chamber pressure but increases from about 450 to 550 when going from chamber temperatures of 2300 K to 3100 K. The increase in fuel elements is in direct response to the higher reactor power requirement, as shown in Fig. 7.26. The number of tie tubes, as shown to the right in Fig. 7.29, also must increase with chamber temperature in order to support the increased quantity of fuel elements.

The final grouping of NTR properties affected by chamber conditions are the peak fuel element and nozzle wall temperatures, as illustrated by Fig. 7.30. The left-

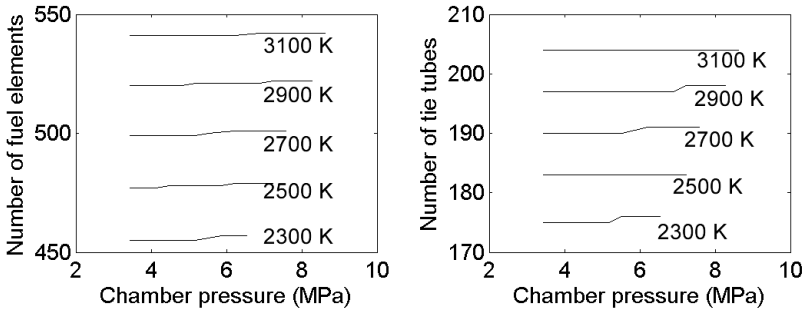

Figure 7.29: Sensitivity of number of reactor core elements to chamber conditions.

hand subplot shows that the peak reactor fuel element temperature does not vary with chamber pressure. As expected, the fuel element temperature increases with chamber temperature. This also shows that, regardless of chamber temperature, a NTR reactor should generally be designed to sustain approximately 100 K higher than the chamber temperature.

The peak nozzle wall temperature, as shown in the right-hand subplot of Fig. 7.30, does vary with both chamber temperature and pressure. Nozzle wall temperature appears to be less sensitive to chamber temperature than other engine parameters. For an 800 K increase in chamber temperature from 2300 K to 3100 K, the nozzle wall temperature only increases approximately 200 K (at a pressure of 4 MPa). Chamber pressure, on the other hand, causes the peak nozzle wall temperature to increase sharply (for a given chamber temperature). The type of response has not been seen anywhere else in this trade study, and is likely due to changing throat area shown in Fig. 7.26. As the nozzle throat are decreases with increasing chamber pressure, so does the area of the nozzle wall. With a smaller wall area, the fixed-diameter cooling jacket pipes cannot provide as much cooling. For pre-

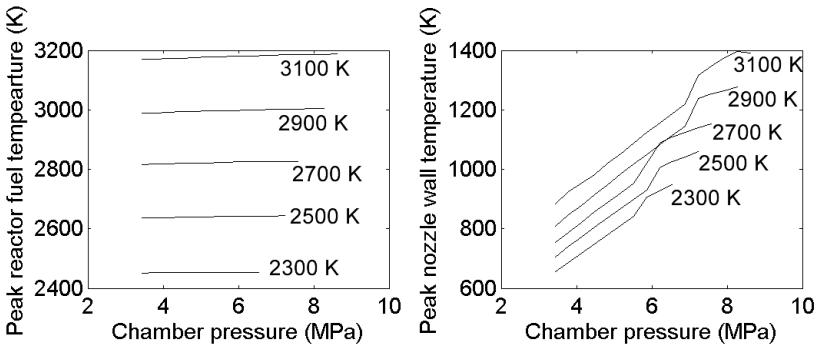

Figure 7.30: Sensitivity of engine material temperatures to chamber conditions.

liminary engine design, this problem could be solved with cooling jacket geometry optimization, but that was not considered here.

7.2.1.2 Reactor Length

The original NERVA engines were designed with a reactor length of 1.32 m. The SNRE and most recent studies assume a shorter length of 0.89m to correspond to the lower power level. To determine the system impact of varying reactor length, the baseline BNTR engine was modeled for lengths from 0.76–2.0 m. Figure 7.31 shows the effect of reactor length on various aspects of engine performance. The upper-left subplot shows the resulting pressure drop across the tie tubes and fuel elements and shows that increasing the reactor length will increase the pressure drop for both elements. This penalty is more severe across the tie tubes because the tie tube coolant sees the length increase twice: once in the supply channel, and a second time along the return.

The upper-right subplot of Fig. 7.31 shows the impact of reactor length on the total propellant flow rate, as well as coolant flow rate through the tie tubes

and nozzle cooling jacket. Following the relationship described earlier, the increased tie tube pressure loss leads to decreased tie tube flow rate, and a corresponding increase in nozzle cooling jacket flow rate. Thus, the flow rate changes shown here are second-order effects, caused by the change in tie tube flow resistance.

The impact of reactor length on the peak fuel element and nozzle wall temperatures is illustrated in the lower-left subplot of Fig. 7.31. The peak fuel temperature drops slightly, from 2875 K at 0.76 m to 2724 K at 2.0 m. This occurs because the magnitude of the reactor power must be higher to provide sufficient heating to the propellant in a shorter span for the shorter reactor lengths. As the reactor lengthens, the "sweet spot" in the middle of the reactor (where the power level peaks) is larger, requiring a lower power level, and thus lower fuel element temperature. The peak nozzle wall temperature drops off as a result of the increased cooling jacket flowrate, as described above. The change in nozzle wall temperature is even more significant, decreasing from 1170 K for a 0.76m reactor to 796 K for a 2.0 m reactor.

Finally, the lower-right subplot shows the impact of reactor length on the number of fuel elements and tie tubes. As observed in the previous trade study, the number of fuel elements and tie tubes will decrease directly with the reactor power. As such, the number of fuel elements drops from 506 to 461 when extending the reactor from 0.76 m to 2.0 m. The number of tie tubes similarly decreases from 192 to 177.

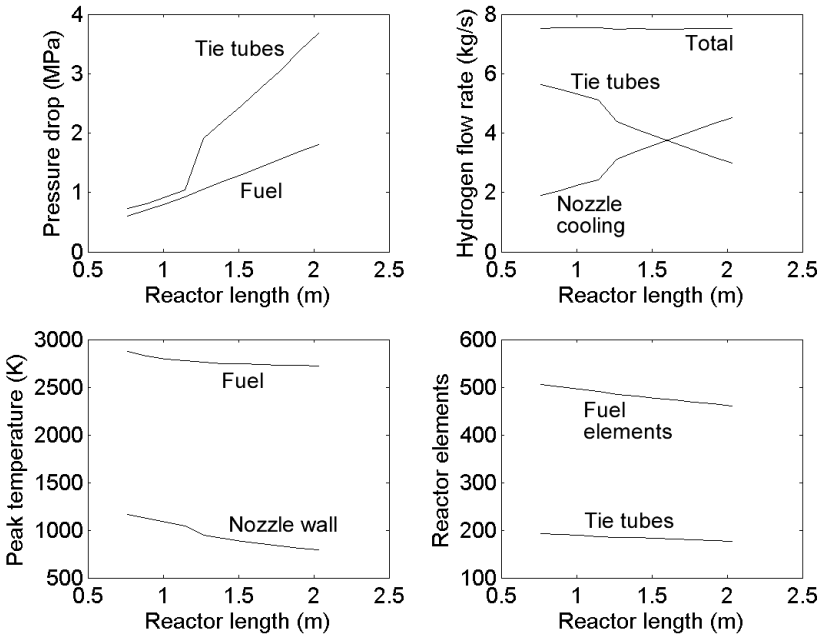

Figure 7.31: Sensitivity of engine performance to reactor length.

7.2.1.3 Reactor Peak-to-Average Factor

As explained earlier, the Peak-to-Average factor relates the average fuel element analyzed here to the one experiencing peak heating, and thus peak material temperatures. The NERVA engines are designed with flow orifices to match the channel coolant flow rate to the local power level. Therefore, the coolant inlet and exit temperatures will be the same regardless of peaking factor and the only impact will be on the peak internal fuel temperature. Figure 7.32 shows the effect of the peaking factor on peak internal fuel temperature. Logically, the results show that as the peaking factor increases, so does the peak fuel temperature. This makes sense, as the only impact of the peaking factor is on the amount of heat transferred through the fuel element, which directly corresponds to the peak material temper-

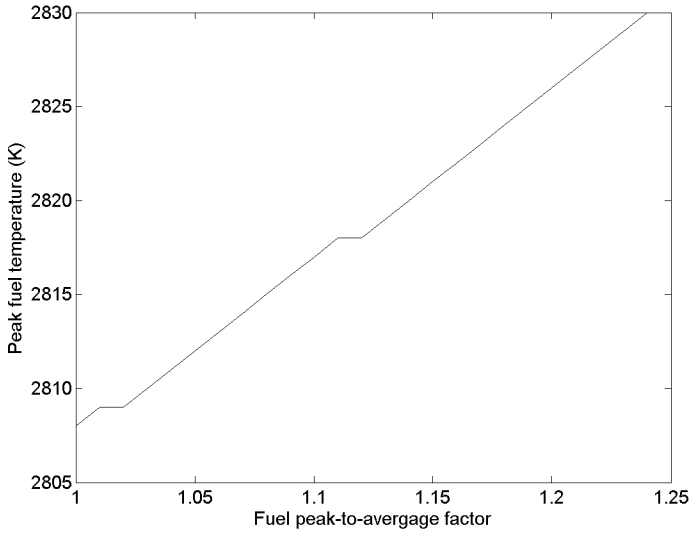

Figure 7.32: Sensitivity of engine performance to reactor length.

ature. Even so, an increase in peaking factor from 1.0 (a flat profile) to 1.25 only increases the fuel temperature by less than 1%.

7.2.2 Power Trade Studies

Several trade studies have been performed on the baseline BNTR in power-generation mode. Although 16.7 kWe is the nominal output power for this system, all of the following studies use the 25 kWe engine out design point, as it is the more demanding design, and will be a better indicator of required Brayton cycle performance.

7.2.2.1 Reactor Size

The only direct, steady-state impact that the propulsion mode has on the power mode for a BNTR engine is the reactor size, as represented by the number of

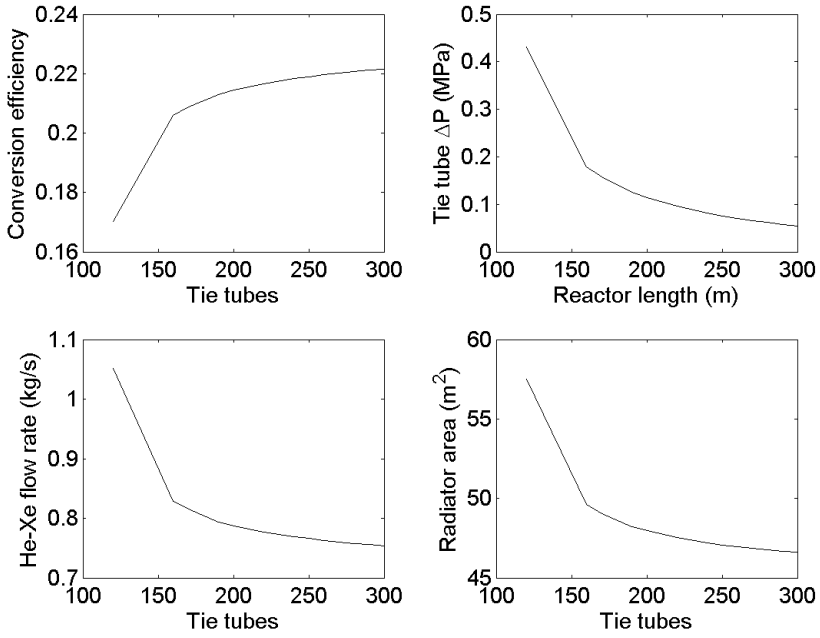

Figure 7.33: Brayton cycle performance in response to varying number of tie tubes.

tie tubes. In order to examine the effects of reactor size, the baseline design was run for reactor sizes varying between 120–300 tie tubes. The results of this study are plotted in Fig. 7.33. The results show that increasing the number of tie tubes (for a given alternator power) increases the cycle efficiency and decreases the tie tube pressure drop, He-Xe flow rate, and radiator area. Thus, as far as the power-mode is concerned, the more tie tubes the better. For an SNRE-based, NERVA-derived engine such as the one here, however, the number of tie tubes can only increase with the number of fuel elements and propulsion-mode reactor power, which would add weight to the engine system. The weight effect has not been examined in this study.

7.2.2.2 Reactor Length

As presented above, changes in reactor length also require changes in the number of tie tubes for the propulsion-mode design. So, to examine the impact of reactor length on the power-mode, a trade study was performed that varied the length *and* corresponding number of tie tubes, as given in Fig. 7.31. Although the propulsion mode was able to examine reactor lengths from 0.76–2.0 m, the power-mode model could only produce results up to a length of 1.27 m. The results of these changes on the Brayton cycle operation are presented in Fig. 7.34. Increasing reactor length causes the tie tube pressure loss to increase (as seen in propulsion mode), thus requiring a higher flow rate and leading to lower conversion efficiency and larger radiator area. So in this case, it is the increase in pressure loss from additional friction along the longer tie tube that hurts the power cycle performance.

7.2.2.3 Compressor Inlet Pressure and Pressure Ratio

The multi-step solver process required to converge the Brayton cycle model has highlighted an interesting feature in this system: the Brayton cycle system is highly sensitive to setting the proper combination of compressor inlet pressure and pressure ratio. To examine this connection, several power cycle designs were run with the same reactor size (185 tie tubes), compressor inlet pressures from 0.689–2.76 MPa, and compressor pressure ratios from 2.0–4.0. Figure 7.35 shows curves of power conversion efficiency versus compressor inlet pressure for various pressure ratios. In

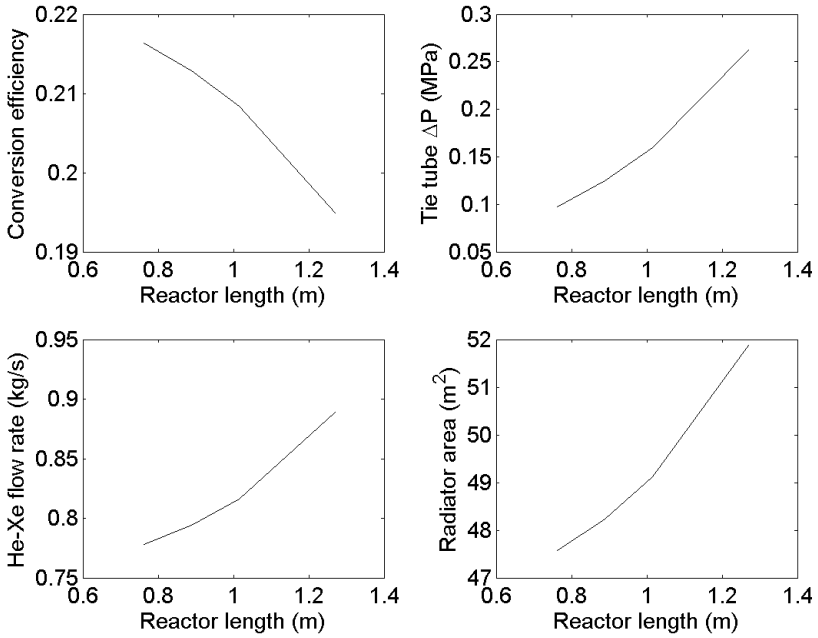

Figure 7.34: Impact of reactor length on Brayton cycle performance.

essence, this figure illustrates a form of manual optimization of the Brayton cycle design.

The optimum efficiency value for each pressure ratio curve is marked with a star. By following the position of the stars along the curves, it is clear that the compressor inlet pressure must increase to maintain optimum performance for lower pressure ratios. Similarly, from pressure ratios of 4.0 to 2.2, lower pressure ratios result in higher efficiency. This effect does seem to suffer from diminishing returns, as the 2.4, 2.2, and 2.0 cases require excessively high pressures to the point that the efficiency of the 2.0 pressure ratio case is actually lower than that of the 2.2 case.

As discussed in Section 3.2.2, the presence of an optimum pressure ratio seems counterintuitive to a traditional Brayton cycle analysis, but is the result of a combination of non-ideal effects in a recuperated Brayton cycle. In fact, the upper-left

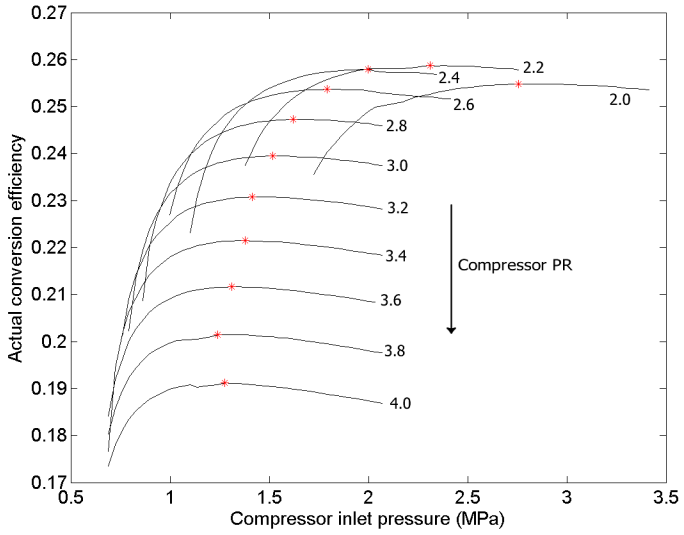

Figure 7.35: Sensitivity of cycle efficiecy to compressor inlet pressure and pressure ratio. The stars indicate the location of peak efficiency on each curve.

plot in Fig. 3.6 assumes the same parameters as the baseline cycle. For the baseline compressor and turbine inlet temperatures of 360 K and 1150 K, respectively, $\alpha = 3.2$ and the optimum pressure ratio should be slightly higher than 2.0. Thus the results here correspond favorably with the theory presented earlier.

The most likely cause of the requirement of higher inlet pressures with lower pressure ratios is the high pressure-drop across the tie tube components. At lower system pressures, the tie tube pressure loss accounts for a significant percentage of the overall pressure. In fact, it is so severe, that the cycle efficiency drops off sharply with decreasing inlet pressure for each curve in Fig. 7.35, and cannot produce results at lower values. At the high inlet pressure and pressure ratio values of this trade study, however, the tie tube pressure loss does not account for as large of a percentage, and incurs a smaller performance penalty.

7.2.2.4 Compressor Inlet Temperature

The compressor inlet temperature is also an input parameter for the Brayton cycle model. Its impact on system performance has been examined by running the baseline model for compressor inlet temperatures ranging from approximately 200–400 K, as opposed to the default value of 360 K. The relatively small range in temperatures is due to the fact that the Brayton model could not converge for temperatures higher or lower than those shown here. As such, these results represent the entire limits on compressor inlet temperature, for the given baseline parameters.

Figure 7.36 shows the engine response to these variations in compressor inlet temperature. In contrast to the other trade studies shown here, increasing the compressor inlet temperature causes both the conversion efficiency *and* radiator area to decrease. The radiator area decreases because a higher compressor inlet temperature corresponds to a higher radiator inlet temperature. As shown in Eq. 7.1, increasing radiator temperature for the same amount of heat rejection means a much smaller radiator is required. The decrease in efficiency with increasing inlet temperature is caused by the increase in tie tube pressure loss, as shown in the upper-right subplot. This also corresponds to a requirement of higher He-Xe flow rate. As such, the decrease in radiator area must be balanced against the decrease in conversion efficiency when selecting the optimal compressor inlet temperature.

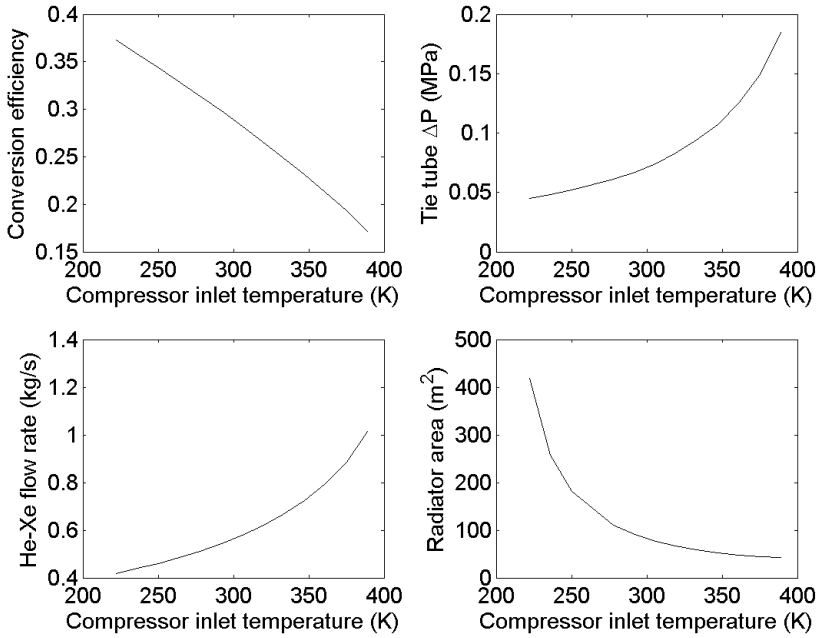

Figure 7.36: Brayton cycle performance in response to varying compressor inlet tempreature.

7.2.2.5 Turbine Inlet Temperature

As illustrated in the difference between Case Study 2 and the Baseline design alone, there is some discrepancy in the value of an appropriate turbine inlet temperature for the Brayton cycle. Current technology limits that value to 1150 K, but some studies claim that near-term materials can allow up to 1300 K without the addition of active cooling systems. To examine these effects, the baseline Brayton cycle model was run for turbine inlet temperature values ranging from 1150–1300 K. The results of this study are plotted in Fig. 7.37.

Figure 7.37 shows that increasing the turbine inlet temperature has a wholly positive impact on the engine performance. It increases the conversion efficiency by increasing the specific power output of the Brayton cycle. With a higher specific

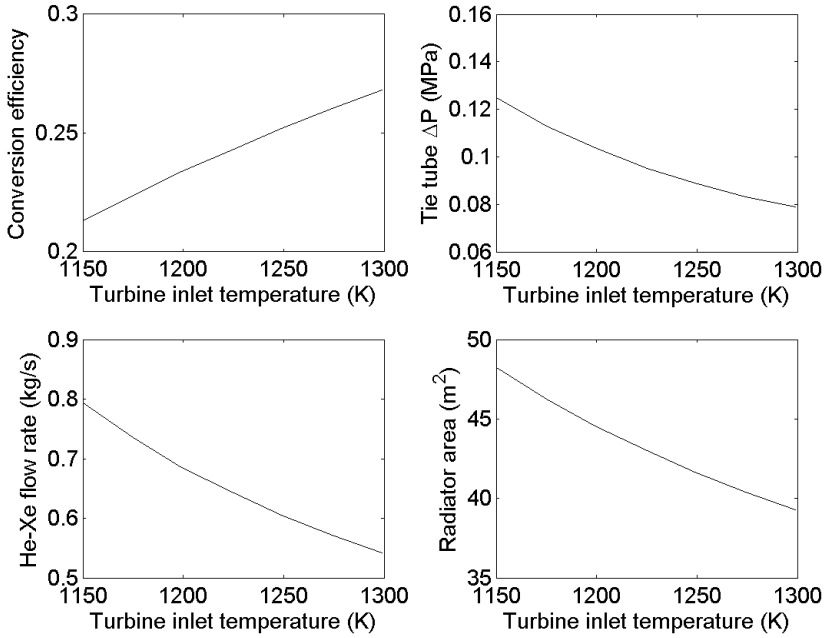

Figure 7.37: Brayton cycle performance in response to varying turbine inlet tempreature.

power output, the same alternator power can be produced at a lower He-Xe flow-rate, which in turn causes the tie tube pressure drop to decrease. Finally, with a higher turbine inlet temperature, the cycle is operating at a higher efficiency and the amount of waste heat to be rejected to the radiator is smaller, meaning a smaller radiator size is required. The main negative to increasing the turbine inlet temperature is that more advanced (and expensive) turbine blade materials are required.

7.2.2.6 Design Output Power

A final trade study examines the impact on system performance of varying the design output power of the Brayton cycle alternator. Fig, 7.38 shows the results of

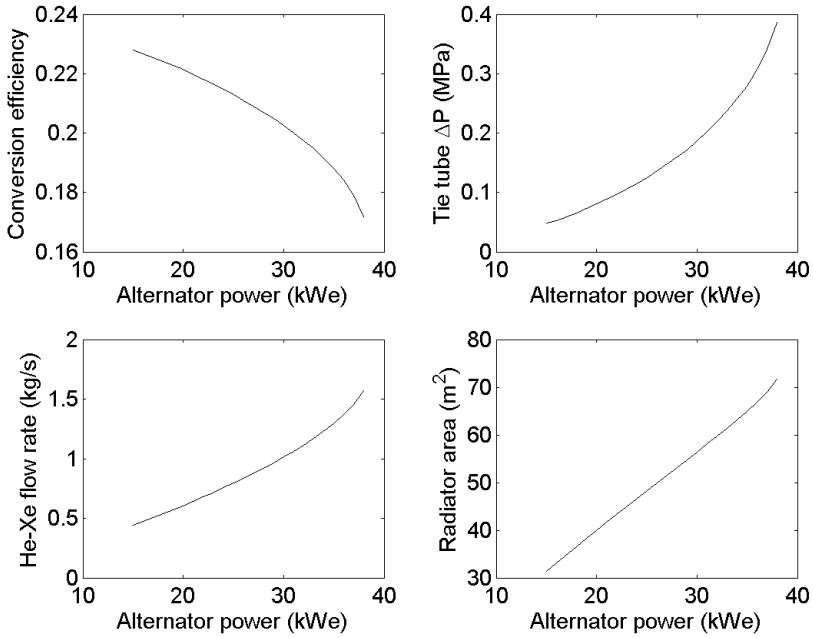

Figure 7.38: Brayton cycle performance in response to varying design output power.

varying the output power from 15–38 kWe. Higher power levels could not produce converged results with the baseline design. The results of this study show that, holding everything else the same, increasing the required output power of a Brayton cycle is bad for performance. To produce more power from the same number of tie tubes, the He-Xe flow rate must be increased. This leads to an increase in the tie tube pressure drop, and thus a decrease in the conversion efficiency. Finally, with a less efficient cycle producing a higher output power, the amount of heat to be rejected increases even more, requiring a larger radiator. Thus, the power-generation mode operates best at the lowest output power possible.

7.3 Technology Limitations

7.3.1 Tie Tube Layer Gaps

The current analysis assumes perfect thermal contact between the adjacent tie tube walls. In reality, there is a slight gap between these layers due to manufacturing tolerances. During power generation mode, the majority of the tie tube material is close to the peak temperature of 1500 K. During propulsion mode, however, the outer layer is at a temperature of 500 K while the inner tie tube layers are as cold as 50 K. As such, there will almost definitely be gaps between the inner and outer layers of the tie tubes, as the colder inner layer contract more than the warmer outer layers. These gaps will increase the thermal resistance of the interface between these layers, requiring a higher outer temperature to produce the same steady-state heat transfer.

In order to calculate the effects of these gaps, the gap spacing, position, and length within the tie tube components must be known. The tie tube heat transfer analysis would also have to be updated to include the thermal resistance of these gaps at the specific location where they occur. The gap size (both width and length) would also likely change with tie tube temperature, so some means for accounting for this change would be required. Very little of this information is currently available, so this analysis is not currently possible. It should be noted, however, that the heat transfer results from the present analysis should be considered best-case estimates, as the presence of tie tube gaps during propulsion mode will reduce the overall conduction between the layers.

7.3.2 Fuel Element Survivability

The tie tube heat material temperature distribution during power generation showed a typical outer temperature near 1500 K. Although the power analysis only considered the tie tube components, the adjacent fuel elements will be producing the required reactor power, without any hydrogen coolant passing through them. Considering that the material temperature of the fuel element is at least 1500 K at the outer edge, it will likely be much higher near the middle — possibly higher than the material limit.

The published fuel element temperature limits are also based on an assumption of running for several minutes at a time, not several months as would be the case of an electric power generation system. As such, problems such as thermal creep and fuel deterioration may become more of a concern than simply melting the fuel. These considerations will require more detailed heat transfer and stress analysis of the fuel elements than what is currently possible with the present model. As such, the results presented here do not represent what a NERVA-derived reactor will be able to sustain, but instead what will be *required* of the reactor, thermally, in order to produce the design electric power output.

7.3.3 Radiator Design

The radiator analysis in the current model is based on a flat, two-sided rectangular geometry. Typical radiators for BNTR-powered vehicles, however, tend to be designed as a truncated, corrugated cone that can be installed between the engines

and aft-most fuel tank. A comparison between radiator sizes of two different designs is still beneficial, but the actual radiator area will have to increase to account for the reduction of radiation heat transfer due to the partially obstructed view factor caused by adjacent panels in the corrugated radiator configuration.

Chapter 8

Conclusions

A new BNTR engine system model has been developed for use with NASA's NPSS code. The model automatically sizes a reactor for a user-specified propulsion design point and then uses that reactor design to calculate Brayton cycle power-generation performance. Physics-based component models have been developed for the reactor fuel elements and tie tubes. The component models calculate the 1-D coolant/propellant thermodynamics in the fuel elements and tie tubes, as well the radial heat conduction with heat generation within the tie tubes.

This model has been used to successfully represent several propulsion-only and bimodal NTR design points, demonstrating its utility for engine design and analysis. There is some discrepancy between the results of this model and other published results, but as this is the only known model capable of incorporating tie tube thermodynamics and heat transfer into the overall system design, validation is not possible.

8.1 Bimodal Feasibility

This study shows that, thermodynamically, bimodal operation is possible with a NERVA-derived engine. The tie tube components are able to drive a Brayton cycle power generator with over 20% conversion efficiency at a typical BNTR design point. The design of the power-generation cycle, however, is very strongly driven by the high pressure loss incurred in the tie tube heat source. The results also highlight several other tie tube limitations and overall design constraints that will be described shortly.

This study, however, does not judge the practicality of BNTR operation. Doing so will require a more detailed weight and cost analysis of a BNTR system in order to determine if bimodal operation provides a real mission-level benefit. The results presented here, though, allow for future NERVA-derived BNTR studies by proving that such operation is possible.

8.2 BNTR Design Constraints

8.2.1 Reactor Control

The results of this study have highlighted several design constraints that will impact any type of BNTR engine. The steady-state design point BNTR analysis shows that the sensitivity of the reactor control system will be a crucial factor in the design and construction of one of these engines. The control system must be able to modulate the reactor with sufficient precision below 80 kWt and well above 300

MWt. From a neutronics standpoint, this type of operation should be possible, but from a control standpoint, the combination of high-power and low-power resolution will require careful consideration.

8.2.2 Decay Heat

Another design constraint for any bimodal system will be the presence of decay heat during the transient period between propulsion and power generation modes. As discussed above, the power generation mode will require a small fraction of the reactor power produced at the beginning of mode transition. If the reactor decay heat is higher than the design power for the Brayton cycle for a significant amount of time, additional cooling capacity must be designed into the bimodal system. Early propulsion-only studies assumed that extra liquid hydrogen would be pulsed through the reactor, cooling it without providing enough flow to affect the vehicle trajectory. As an alternative, the Brayton cycle system could be used to actively cool the reactor during mode transition, but doing so would likely require a larger radiator and heat rejection system in order to dispose of the extra waste heat. A comparison between these two cooling methodologies could lead to an interesting trade between the weight added by extra coolant/propellant or a larger radiator. Finally, although it is unlikely that reactor power level produced by decay heat alone will be greater than the thermal power required by a Brayton cycle power system, such a situation is possible and should be considered, as it would immediately overwhelm a power conversion system sized for the vehicle requirements alone.

8.2.3 Power Generation Turbine Inlet Temperature

The final design parameter that should be carefully considered for any BNTR system is the Brayton cycle turbine inlet temperature. A comparison between the propulsion and power design point results shows a wide variation in temperature of the tie tube component. Although this component is specific to NERVA-derived engines, the reactor temperature in power generation mode is fixed by the typical design point of an 1150 K turbine inlet temperature. Traditional gas turbine experience leads one to design a system for the highest turbine inlet temperature possible in order to increase the cycle temperature ratio, and thus thermodynamic efficiency. Doing so in a nuclear-heated system, however, requires a similarly high reactor temperature. Over the duration of a Mars mission, that high temperature could lead to the degradation of the reactor materials. As such, the turbine inlet temperature for a BNTR should be designed to balance not only power conversion efficiency, but also reactor survivability.

8.3 Tie Tube Limitations

The above constraints will impact *any* BNTR system, but there are additional design limitations imposed by the use of tie tubes in a NERVA-derived reactor. These limitations stem primarily from the low heat transfer through the elements, which leads to higher pressure losses.

8.3.1 Poor Heat Transfer

The various propulsion-mode design point studies highlighted a limitation in the heat transfer capability of the tie tube elements during propulsion operation. Although many previous studies assume tie tube exit temperatures as high as 600 K, this study calculated that value to be closer to 200 K (for the same $\tilde{3}0$ K tie tube inlet temperature. This means that the heat transfer into the tie tube coolant is much less than that into the nozzle cooling jacket and control drum / reflector coolant. It is for this reason that the both cooling lines had to be directed back up to the turbines; the tie tube coolant could not provide sufficient energy to drive the turbopumps alone.

The likely cause of this problem is that the outer two layers of the tie tube are made of graphite (C) and ZrC, which are both insulators with low thermal conductivity. This is why the heat conducted from the fuel elements to the tie tubes remains in this outer layer and very little makes it to the tie tube coolant. This heat transfer limitation actually occurs by design. When the tie tube elements were first introduced as solid "tie rods" without coolant channels, insulating materials were specifically needed in order to reduce the peak temperature of the structural components. For modern bimodal designs, however, it is now desirable to have heat transfer through the tie tube walls and into the middle, where the solid rod has been replaced with Inconel tubes and coolant channels.

Heat transfer through the tie tube could be increased by replacing the outer material layers with a material with similar neutron absorption properties, but a

higher conductivity. Additionally, geometry optimization could produce designs with more effective heat transfer, but similar nuclear and structural properties.

8.3.2 Pressure Loss

The power-generation results of this study have shown that the tie tube components create a large pressure loss during Brayton cycle operation. This pressure loss occurs because the low tie tube temperature increase requires an increase coolant flow rate to deliver the required heat transfer rate. This increase in mass flow leads to a corresponding increase in pressure loss, which requires the compressor to operate at a significantly higher discharge pressure.

Although these effects were not considered in the present study, the compressor discharge pressure increase will require stronger ducts and heat exchangers, which will increase the overall power conversion system weight. Operating at a higher pressure ratio will also likely degrade the compressor efficiency, an effect which was not seen with the fixed efficiency compressor model of this study.

The tie tube pressure loss should be alleviated by correcting the heat transfer problem described above. Another solution could be to design the tie tube elements for power generation operation as well as propulsion. Incorporating both modes of operation into a design/optimization study should produce a more effective tie tube design that transfers heat more effectively with a lower pressure loss.

8.3.3 Layer Gaps

As mentioned at the end of the previous chapter, the combination of interference fit construction with large temperature variations during the two operating modes means that gaps will occur in between the tie tube layers during propulsion mode. These gaps could also be eliminated by redesigning the tie tube components to be constructed from as few layers of material as possible.

8.4 NPSS Solver Limitations

The propulsion-mode model is limited in its ability to model widely varying design points because of the NPSS solver. The purpose of the solver is to find the appropriate combination of independent variable values that satisfies all of the dependent conditions. In theory, it should be able to complete this task regardless of the initial values of the independents. At worst, is should take longer to find a converged solution when starting with poor initial conditions. However, the non-linear closed-loop form of the Brayton cycle model makes this process more difficult. Using the default initial conditions from CCSS, the solver cannot find the converged baseline solution. This is why a multi-step convergence process must be employed. The first pass finds a design based on a fixed reactor power, then the second pass is able to solve for system performance at the design alternator power. From there, running different design points often requires multiple intermediate solutions in order to work.

One example of this is the process required to run the 37 kWe DRM Case

Study 2 model. The power model was first run through its normal steps to find a converged solution at 25 kWe. The solver was then run several more times, increasing the alternator power gradually towards 37 kWe. This process was automated in the BNTR run file, so that the converged solution for one run became the initial conditions for the next.

The most likely reason for this problem is that the design space for the tie tube heated Brayton cycle is likely convoluted, with many infeasible designs. The NPSS Newton-Raphson solver would then have difficult time assessing the gradients and being able to follow the appropriate path through the design space to a converged solution. The NPSS solver does have several parameters which can alter the default step size, maximum number of iterations to perform, as well as dozens of other more complex solver functions. With the exception of iteration limit and default step-size, these parameters were untouched in this project. It is possible that these parameters could be tweaked to allow for better convergence of varying design points by moving through the design space in smaller increments, but with a likely penalty in run time.

Another possible solution for the solver design space limitation would be the addition of a probabilistic engine to the NPSS solver. Employing a genetic algorithm, for example, would permit the solver to find a solution in any design space, but at a high expense to computation time. The addition of such a method would also enable cycle optimization, which could be very beneficial for this study.

8.5 Contributions to the State-of-the-Art

8.5.1 The First Integrated BNTR System Model

The combined propulsion and power system model is the first known model to calculate the performance of both modes of operation for a NERVA-derived BNTR with a common reactor component model. It is the first known model to integrate a physics-based analysis of the reactor and tie tubes into both the propulsion and power generation system models. It is also the first model to size the reactor for propulsion mode *and* use that information to specify the number of tie tubes available for power-generation. As the model has been developed in NPSS, it is entirely portable and can be run on any computer that runs NPSS. As such, the model itself is being provided to NASA Glenn Research Center, in order to add capability and fidelity to their Mars vehicle architecture studies.

8.5.2 New Tie Tube Component Model

In order to perform the analysis described above, a new physics-based, computationally efficient tie tube component model was created. This model incorporates the coolant analysis used by the NESS code with the fundamental, closed form calculation of the tie tube wall heat conduction, including the effects of heat generation. The addition of this tie tube component model replaces previous empirical assumptions of tie tube performance and adds flexibility to the NTR engine designs that can be accurately represented by the BNTR model. This physics-based, analytical component model also permits a detailed, yet computationally efficient analysis of

the propulsion and power-generation performance.

8.5.3 Detailed Analysis of a DRM 4.0 Power System

In addition to the model itself, this project has presented the first known detailed analysis of the power generation mode of a DRM 4.0 engine. Although the Mars vehicles that have been proposed use three engines to produce 50 kWe power, the majority of the detailed Brayton cycle analyses in the literature focus on a single Brayton unit producing at least 50 kWe. This project, on the other hand, has directly modeled the performance of a BNTR propulsion and power-generation system designed for 66.7 kN of thrust operating at 16.7 kWe and 25 kWe of power.

8.6 Recommendations

8.6.1 Engine Weight Analysis

Both NESS and CCSS contain system weight models, but they were not used by the current study. The NESS model contained some errors in calculating the reactor size, and was based almost on entirely on empirical functions based on average reactor area, control drum size, etc. The heaviest component in a NTR is generally the radiation shield, and the NESS shield weight calculation is based on a circular disc used to shield from a single engine. A three-engine system, like that proposed in DRM 4.0, will require a single, larger shield that blocks covers more area than three single disks alone.

CCSS contains a similar weight analysis, but it is based on a 50 kWe JIMO mission engine and assumes the use of a large, flat, two-sided radiator. As shown in the previous work, the Mars Transfer Vehicle designs typically employ a one-side, truncated, corrugated cone-shaped radiator. As such, the weight of this radiator system will likely be much heavier than that calculated by NESS.

The engine weight is an incredibly important parameter; if the addition of a BNTR power system weighs more than a separate power system alone, then the use of bimodal power may not be the best choice. As such, future studies should incorporate and update the pre-existing weight models into the current code.

8.6.2 Reactor Material and Geometry Optimization

The purpose of the present study was to determine the feasibility of using the tie tube components of a NERVA-derived reactor for power generation in a BNTR engine. This work has highlighted several limitations of this type of system, many of which could be alleviated through the design and optimization of a new BNTR-designed reactor system. Pratt & Whitney's ESCORT engine (as described in Chap. 2) is one such engine currently under development, but further work could be possible with other fuel materials or geometries.

8.6.3 Transient Analysis

Now that the feasibility of a NERVA-derived BNTR system has been demonstrated, the transient capability of the system should be examined. As mentioned

briefly in the introduction, the reactor heating environment will be severe while transitioning from the high power propulsion mode to the power generation mode. Current designs assume that extra hydrogen will be pulsed through the reactor, drawing out heat without creating unwanted propulsion. As a means to save propellant mass, the power cycle could be used to remove this heat actively. This process would likely require a larger radiator, creating an interesting trade study between the additional hydrogen or radiator mass required for cooling during mode transition.

BIBLIOGRAPHY

[1] *The Vision for Space Exploration*, NASA, Washington, DC, February 2004.

[2] *A Journey to Inspire, Innovate, and Discover: Report of the President's Commission on Implementation of United States Space Exploration Policy*, NASA, Washington, DC, June 2004.

[3] *The Role of Nuclear Power and Nuclear Propulsion in the Peaceful Exploration of Space*, International Atomic Energy Agency, Vienna, Austria, 2005.

[4] Borowski, S. K., Dudzinski, L. A., and McGuire, M. L., "Vehicle and Mission Design Options for the Human Exploration of Mars/Phobos using Bimodal NTR and LANTR Propulsion," *34th Joint Propulsion Conference*, Cleveland, OH, July 1998, AIAA-1998-3883.

[5] Borowski, S. K., Dudzinski, L. A., and McGuire, M. L., "Artificial Gravity Vehicle Design Option for NASA's Human Mars Mission Using 'Bimodal' NTR Propulsion," *35th Joint Propulsion Conference*, Los Angeles, CA, June 1999, AIAA-1999-2545.

[6] Borowski, S. K., Dudzinski, L. A., and McGuire, M. L., "Artificial Gravity Human Exploration Missions to Mars and Near Earth Asteroids Using 'Bimodal' NTR Propulsion," *36th Joint Propulsion Conference*, Huntsville, AL, July 2000, AIAA-2000-3115.

[7] Borowski, S. K., Dudzinski, L. A., and McGuire, M. L., "Bimodal Nuclear Thermal Rocket (NTR) Propulsion for Power-Rich, Artificial Gravity Human Exploration Missions to Mars," *52nd International Astronautical Congress*, Toulouse, France, October 2001, IAA-01-IAA.13.3.05.

[8] Walberg, G. D., "How Shall We Go to Mars? A Review of Mission Scenarios," *Journal of Spacecraft and Rockets*, Vol. 30, No. 2, March-April 1993, pp. 129–139.

[9] Rauwolf, G. A., Pelaccio, D. G., Patel, S., and Sorenson, K., "Mission Performance of Emerging In-Space Propulsion COncepts for One-Year Crewed Mars Missions," *37th Joint Propulsion Conference*, Salt Lake City, UT, July 2001, AIAA-2001-3374.

[10] Donahue, B. B. and Cupples, M. L., "Comparative Analysis of Current NASA Human Mars Mission Architectures," *Journal of Spacecraft and Rockets*, Vol. 38, No. 5, September-October 2001, pp. 745–751.

[11] Cassenti, B. N., "Trajectory Options for Manned Mars Missions," *Journal of Spacecraft and Rockets*, Vol. 42, No. 5, September-October 2005, pp. 890–895.

[12] Griffin, B., Thomas, B., Vaughan, D., Drake, B., Johnson, L., and Woodcock, G., "A Comparison of Transportation Systems for Human Missions to Mars," *40th Joint Propulsion Conference*, Fort Lauderdale, FL, July 2004, AIAA-2004-3834.

[13] Koenig, D. R., "Experience Gained from the Space Nuclear Rocket Program (Rover)," Tech. Rep. LA-10062-H, Los Alamos National Laboratory, Los Alamos, NM, 1986.

[14] Bulman, M. J. and Neill, T. M., "Simulated LOX-Augmented Nuclear Thermal Rocket (LANTR) Testing," *36th Joint Propulsion Conference*, Huntsville, AL, July 2000, AIAA-2000-3897.

[15] Bulman, M. J., Messitt, D. G., Neill, T. M., and Borowski, S. K., "High Area Ratio LOX-Augmented Nuclear Thermal Rocket (LANTR) Testing," *37th Joint Propulsion Conference*, Salt Lake City, UT, July 2001, AIAA-2001-3369.

[16] Bulman, M. J., Messitt, D. G., Neill, T. M., and Borowski, S. K., "Continued LOX-Augmented Nuclear Thermal Rocket (LANTR) Testing," *38th Joint Propulsion Conference*, Indianapolis, IN, July 2002, AIAA-2002-3650.

[17] Bulman, M. J. and Borowski, S. K., "Deep Space Propulsion Requirements Development," *39th Joint Propulsion Conference*, Huntsville, AL, July 2003, AIAA-2003-5129.

[18] Bulman, M. J., Neill, T. M., and Borowski, S. K., "LANTR Engine System Integration," *40th Joint Propulsion Conference*, Fort Lauderdale, FL, July 2004, AIAA-2004-3864.

[19] Beveridge, J. H., "Feasibility of Using a Nuclear Rocket Engine for Electrical Power Generaiton," *AIAA/SAE 7th Propulsion Joint Specialists Conference*, Salt Lake Cite, UT, June 1971, AIAA-1971-639.

[20] Gunn, S. V., Hedstrom, J., and Hundal, R., "Power Generation Capabilities of Tie Tube Assemblies," *Proceedings of Space Technology and Applications International Forum (STAIF-1994)*, edited by M. S. El-Genk, Vol. 301 of *AIP Conference Proceedings*, Melville, NY, February 1994, pp. 659–664.

[21] Zweig, H. R. and Hundal, R., "NERVA-Derived Nuclear Thermal Propulsion Dual Mode Operation," *Proceedings of Space Technology and Applications International Forum (STAIF-1994)*, edited by M. S. El-Genk, Vol. 301 of *AIP Conference Proceedings*, Melville, NY, February 1994, pp. 1565–1572.

[22] Fusselman, S. P., Borowski, S. K., Frye, P. E., Gunn, S. V., and Morrison, C. Q., "NERVA-Derived Concept for a Bimodal Nuclear Thermal Rocket," *Proceedings of Space Technology and Applications International Forum (STAIF-2005)*, edited by M. S. El-Genk, Vol. 746 of *AIP Conference Proceedings*, Melville, NY, February 2005, pp. 512–519.

[23] Joyner, R. and Feller, G. J., "Manned Mars Mission Enhancement Using Pratt & Whitney ESCORT Combined Propulsion and Power System," *Proceedings of Space Technology and Applications International Forum (STAIF-1999)*, edited by M. S. El-Genk, Vol. 458 of *AIP Conference Proceedings*, Melville, NY, February 1999, pp. 1269–1274.

[24] Dudzinski, L. A. and Borowski, S. K., "Bimodal Nuclear Electric Propulsion," *38th Joint Propulsion Conference*, Indianapolis, IN, July 2002, AIAA-2002-3653.

[25] Borowski, S. K., McGuire, M. L., Mason, L. M., Gilland, J. H., and Packard, T. W., "Bimodal Nuclear Thermal Rocket (BNTR) Propulsion for an Artificial Gravity HOPE Mission to Callisto," *Proceedings of Space Technology and Applications International Forum (STAIF-2003)*, edited by M. S. El-Genk, Vol. 654 of *AIP Conference Proceedings*, Melville, NY, February 2003, pp. 829–836.

[26] McGuire, M. L., Borowski, S. K., Mason, L. M., and Gilland, J. H., "High Power MPD Nuclear Electric Propulsion (NEP) for Artificial Gravity HOPE Mission to Callisto," *Proceedings of Space Technology and Applications International Forum (STAIF-2003)*, edited by M. S. El-Genk, Vol. 654 of *AIP Conference Proceedings*, Melville, NY, February 2003, pp. 837–843.

[27] Falck, R. D. and Borowski, S. K., "High Power Nuclear Electric Propulsion (NEP) for Cargo and Propellant Transfer Missions to Cislunar Space," *Proceedings of Space Technology and Applications International Forum (STAIF-2003)*, edited by M. S. El-Genk, Vol. 654 of *AIP Conference Proceedings*, Melville, NY, February 2003, pp. 844–849.

[28] Bussard, R. W., "Nuclear Powered Rockets: A Historical Survey and Literature Summary," *The LASL Nuclear Rocket Propulsion Program*, edited by R. E. Schreiber, LAMS-2036, Los Alamos Scientific Laboratory, 1956, pp. 32–49.

[29] Dewar, J. A., *To the End of the Solar System: The Story of the Nuclear Rocket*, University Press of Kentucky, Lexington, KY, 2004.

[30] Walton, J. T., "Overview of Tested and Analyzed NTP Concepts," Tech. Rep. TM-105252, NASA Lewis Research Center, Cleveland, OH, 1991.

[31] Watson, C. W., "Nuclear Rockets: High-Performance Propulsion for Mars," Tech. Rep. LA-12784-MS, Los Alamos National Laboratory, Los Alamos, NM, 1994.

[32] Corrington, L. C., "The Nuclear Rocket Program — Its Status and Plans," *Journal of Spacecraft and Rockets*, Vol. 6, No. 4, April 1969, pp. 465–470.

[33] Ellerbrock, H. H., Livingood, J. N. B., and Straight, D. M., "Fluid-Flow and Heat-Transfer Problems in Nuclear Rockets," *Nuclear Rocket Propulsion*, SP-20, NASA, 1962, pp. 27–36.

[34] Bogart, D. and Lantz, E., "Nuclear Physics of Solid-Core Gas-Cooled Rocket Propulsion Reactors," *Nuclear Rocket Propulsion*, SP-20, NASA, 1962, pp. 17–25.

[35] Beckwith, W. C. and Johnson, H. L., "Advanced Space Mission Capabilities of Nuclear Rockets," *Journal of Spacecraft and Rockets*, Vol. 1, No. 4, July-August 1964, pp. 414–420.

[36] Altseimer, J. H., Mader, G. F., and Stewart, J. J., "Operating Characteristics and Requirements for the NERVA Flight Regime," *Journal of Spacecraft and Rockets*, Vol. 8, No. 7, July 1971, pp. 766–773.

[37] Durham, F. P., "Nuclear Engine Definition Study Preliminary Report, Volume 1 - Engine Description," Tech. Rep. LA-5044-MS, Vol. 1, Los Alamos Scientific Laboratory, Los Alamos, NM, 1972.

[38] Durham, F. P., "Nuclear Engine Definition Study Preliminary Report, Volume 2 - Supporting Studies," Tech. Rep. LA-5044-MS, Vol. 2, Los Alamos Scientific Laboratory, Los Alamos, NM, 1972.

[39] Durham, F. P., "Nuclear Engine Definition Study Preliminary Report, Volume 3 - Preliminary Program Plan," Tech. Rep. LA-5044-MS, Vol. 3, Los Alamos Scientific Laboratory, Los Alamos, NM, 1972.

[40] "Report of the 90–Day Study on Human Exploration of the Moon and Mars," Tech. Rep. TM-102999, NASA, November 1989.

[41] Stafford, T. P., *America at the Threshold: Report of the Synthesis Group on America's Space Exploration Initiative*, US Government Printing Office, Washington, DC, 1991.

[42] Scheil, C. M., Pelaccio, D. G., and Petrosky, L. J., "Nuclear Engine System Simulation (NESS) Program Update," *Proceedings of Space Technology and Applications International Forum (STAIF-1993)*, edited by M. S. El-Genk, Vol. 271 of *AIP Conference Proceedings*, Melville, NY, February 1993, pp. 1523–1528.

[43] Pelaccio, D. G., Scheil, C. M., and Petrosky, L. J., "Nuclear Engine System Simulation (NESS): Version 2.0, Program User's Guide," Tech. Rep. CR-191081, NASA, 1993.

[44] Petrosky, L., "Scaling Laws of Prismatic Solid Fuel Nuclear Rocket Engines," *27th Joint Propulsion Conference*, Sacramento, CA, June 1991, AIAA-1991-2337.

[45] Fittje, J. E. and Buehrle, R. J., "Conceptual Engine System Design for NERVA Derived 66.8KN and 111.2KN Thrust Nuclear Thermal Rockets," *Proceedings of Space Technology and Applications International Forum (STAIF-2006)*, edited

by M. S. El-Genk, Vol. 813 of *AIP Conference Proceedings*, Melville, NY, February 2006, pp. 502–513.

[46] Parsley, R. C., "Advanced Propulsion Engine Assessment Based on a CERMET Reactor," *Nuclear Propulsion Technical Interchange*, Vol. 10116 of *NASA Conference Publication*, Sandusky, OH, October 1992, pp. 150–216.

[47] Feller, G. J. and Joyner, R., "ESCORT: A Pratt & Whitney Nuclear Thermal Propulsion and Power System for Manned Mars Missions," *Proceedings of Space Technology and Applications International Forum (STAIF-1999)*, edited by M. S. El-Genk, Vol. 458 of *AIP Conference Proceedings*, Melville, NY, February 1999, pp. 1495–1500.

[48] Feller, G. J. and Joyner, R., "Pratt & Whitney ESCORT Derivative for Mars Surface Power," *Proceedings of Space Technology and Applications International Forum (STAIF-1999)*, edited by M. S. El-Genk, Vol. 458 of *AIP Conference Proceedings*, Melville, NY, February 1999, pp. 1205–1210.

[49] Joyner, C. R., Fowler, B., and Matthews, J., "A Closed Brayton Power Conversion Unit Concept for Nuclear Electric Propulsion for Deep Space Missions," *Proceedings of Space Technology and Applications International Forum (STAIF-2003)*, edited by M. S. El-Genk, Vol. 654 of *AIP Conference Proceedings*, Melville, NY, February 2003, pp. 677–684.

[50] Joyner, C. R., Phillips, J. E., Fowler, B. B., and Borowski, S. K., "TRITON: A TRImodal Capable, Thrust Optimized, Nuclear Propulsion and Power System for Advanced Space Missions," *40th Joint Propulsion Conference*, Fort Lauderdale, FL, July 2004, AIAA-2004-3863.

[51] Ludewig, H., Todosow, P., Montanez, P., and Belzer, P., "Preliminary Study of Impact of Fuel Options on Performance of Nuclear Thermal Propulsion (NTP) Concepts," *Proceedings of Space Technology and Applications International Forum (STAIF-2002)*, edited by M. S. El-Genk, Vol. 608 of *AIP Conference Proceedings*, Melville, NY, February 2002, pp. 1084–1095.

[52] Halfinger, J., Husser, D., and Kerr, J., "Candidate Near-Term Fuel Options for Conventional and Bimodal NTR Engines," *41st Joint Propulsion Conference*, Tucson, AZ, July 2005, AIAA-2005-3960.

[53] Joyner, R., Lentati, A., and Cichon, J., "Multidisciplinary Analysis of Nuclear Thermal Propulsion Design Options for Human Exploration Missions," *42nd Joint Propulsion Conference*, Sacramento, CA, July 2006, AIAA-2006-4554.

[54] Joyner, R., Lentati, A., and Cichon, J., "Mars Mission Analysis Trades Based on Legacy and Future Nuclear Propulsion Options," *Proceedings of Space Technology and Applications International Forum (STAIF-2007)*, edited by M. S. El-Genk, Vol. 880 of *AIP Conference Proceedings*, Melville, NY, February 2007, pp. 289–296.

[55] Borowski, S. K., Corban, R. R., Culver, D. W., Mulman, M. J., and McIlwain, M. C., "A Revolutionary Lunar Space Transportation System Architecture Using Extraterrestrial LOX-Augmented NTR Propulsion," *30th Joint Propulsion Conference*, Indianapolis, IN, June 1994, AIAA-1994-3343.

[56] Borowski, S. K. and Dudzinski, L. A., "High Leverage Space Transportation System Technologies for Human Exploration Missions to the Moon and Beyond," *32nd Joint Propulsion Conference*, Lake Buena Vista, FL, July 1996, AIAA-1996-2810.

[57] Borowski, S. K. and Dudzinski, L. A., "2001: A Space Odyssey Revisited - The Feasibility of 24 Hour Commuter Flights to the Moon Using NTR Propulsion with LUNOX Afterburners," *33rd Joint Propulsion Conference*, Seattle, WA, July 1997, AIAA-1997-2956.

[58] Stancati, M. L., Jacobs, M. K., and Rauwolf, G. A., "LANTR/ISPP-Based Space Transportation for Moon/Mars Missions: Part 1 – Analysis," *36th Joint Propulsion Conference*, Huntsville, AL, July 2000, AIAA-2000-3111.

[59] Stancati, M. L., Jacobs, M. K., and Rauwolf, G. A., "LANTR/ISPP-Based Space Transportation for Moon/Mars Missions: Part 2 – Results," *36th Joint Propulsion Conference*, Huntsville, AL, July 2000, AIAA-2000-3112.

[60] Glenn, D. E. and Bulman, M. J., "CFD Analysis of the LOX-Augmented Nuclear Thermal Rocket (LANTR)," *35th Joint Propulsion Conference*, Los Angeles, CA, June 1999, AIAA-1999-2546.

[61] Kirk, W. L., Hedstrom, J. C., Moore, S. W., McFarland, R. D., Merrigan, M. A., Buksa, J. J., Cappiello, M. W., Hanson, D. L., and Woloshun, K. A., "An Investigation of Dual-Mode Operation of a Nuclear-Thermal Rocket Engine," Tech. Rep. LA-12102, Los Alamos National Laboratory, Los Alamos, NM, 1991.

[62] Buden, D., Kennedy, F., and Jacox, M., "Bimodal Nuclear Power and Propulsion: Scoping the Design Approaches," *AIAA 1995 Space Programs and Technologies Conference*, Huntsville, AL, September 1995, AIAA-1995-3836.

[63] Buksa, J. J., DeMuth, S., and Huber, T., "Assessment of an SP-100 Bi-Modal Propulsion and Power System," *Proceedings of Space Technology and Applications International Forum (STAIF-1994)*, edited by M. S. El-Genk, Vol. 301 of *AIP Conference Proceedings*, Melville, NY, February 1994, pp. 1391–1400.

[64] Culver, D. W. and Bulman, M. J., "Multimodal Space Nuclear Thermal Propulsion and Power System for Space Industrialization," *Proceedings of Space Technology and Applications International Forum (STAIF-1995)*, edited by M. S. El-Genk, Vol. 324 of *AIP Conference Proceedings*, Melville, NY, February 1995, pp. 747–754.

[65] Polansky, G. F., Rochow, R. F., Gunther, N. A., and Bixler, C. H., "A Bimodal Power and Propulsion System Based on Cermet Fuel and Heat Pipe Energy Transport," Tech. Rep. SAND95-0903C, Sandia National Laboratories, Albuquerque, NM, 1995.

[66] Weitzberg, A. and Warren, J. W., "Pin and CERMET Hybrid Bimodal Reactor," *Proceedings of Space Technology and Applications International Forum (STAIF-1995)*, edited by M. S. El-Genk, Vol. 324 of *AIP Conference Proceedings*, Melville, NY, February 1995, pp. 741–746.

[67] "Reference Mission Version 3.0 Addendum to the Human Exploration of Mars: The Reference Mission of the NASA Mars Exploration Study Team," Tech. Rep. NASA/SP-6107-ADD, NASA, June 1998.

[68] Dissel, A. F., *Departure Phase Aborts for Manned Mars Missions*, Ph.D. thesis, University of Maryland, College Park, MD, 2007.

[69] Marcus, L., Way, D., Medlin, M., Sakai, T., McIntire, J., and Olds, J. R., "Technology Assessment for Manned Mars Exploration Using a ROSETTA Model of a Bimodal Nuclear Thermal Rocket (BNTR)," *AIAA Space 2001 Conference and Exposition*, Albuquerque, NM, August 2001, AIAA-2001-4623.

[70] Christie, R. J. and Plachta, D. W., "Zero Boil-Off System Design and Thermal Analysis of the Bimodal Thermal Nuclear Rocket," *Proceedings of Space Technology and Applications International Forum (STAIF-2006)*, edited by M. S. El-Genk, Vol. 813 of *AIP Conference Proceedings*, Melville, NY, February 2006, pp. 494–501.

[71] McCurdy, D. R., Krivanek, T. M., Roche, J. M., and Zinolabedini, R., "Bimodal Nuclear Thermal Rocket Sizing and Trade Matrix for Lunar, Near Earth Asteroid and Mars Missions," *Proceedings of Space Technology and Applications International Forum (STAIF-2006)*, edited by M. S. El-Genk, Vol. 813 of *AIP Conference Proceedings*, Melville, NY, February 2006, pp. 827–836.

[72] Boman, L. H. and Gallagher, J. G., "NERVA Technology Reactor Integrated with NASA Lewis Brayton Cycle Space Power Systems," *Journal of Spacecraft and Rockets*, Vol. 8, No. 5, May 1971, pp. 500–505.

[73] Gavert, R. B., "Market Driven Space Exploration," *Proceedings of Space Technology and Applications International Forum (STAIF-2004)*, edited by M. S. El-Genk, Vol. 699 of *AIP Conference Proceedings*, Melville, NY, February 2004, pp. 183–188.

[74] Taylor, R., "Prometheus Project Final Report," Tech. Rep. 982-R120461, NASA Jet Propulsion Laboratory, Pasadena, CA, October 2005.

[75] Ashcroft, J. and Eshelman, C., "Summary of NR Program Prometheus Efforts," *Proceedings of Space Technology and Applications International Forum*

(STAIF-2007), edited by M. S. El-Genk, Vol. 880 of *AIP Conference Proceedings*, Melville, NY, February 2007, pp. 497–521.

[76] Wright, S. A., "Preliminary Results of a Dynamic System Model for a Closed-Loop Brayton Cycle Coupled to a Nuclear Reactor," *1st International Energy Conversion Engineering Conference and Exhibit (IECEC)*, Portsmouth, VA, August 2003, AIAA-2003-6008.

[77] Wright, S. A. and Sanchez, T., "Dynamic Modeling and Control of Nuclear Reactors Coupled to Closed-Loop Brayton Cycle Systems using SIMULINK," *Proceedings of Space Technology and Applications International Forum (STAIF-2005)*, edited by M. S. El-Genk, Vol. 746 of *AIP Conference Proceedings*, Melville, NY, February 2005, pp. 991–1004.

[78] Wright, S. A., Fuller, R., Lipinski, R. J., Nichols, K., and Brown, N., "Operational Results of a Closed Brayton Cycle Test-Loop," *Proceedings of Space Technology and Applications International Forum (STAIF-2005)*, edited by M. S. El-Genk, Vol. 746 of *AIP Conference Proceedings*, Melville, NY, February 2005, pp. 699–710.

[79] Lipinski, R. J., Wright, S. A., Dorsey, D. J., Peters, C. D., Brown, N., Williamson, J., and Jablonski, J., "Operational Results of a Closed Brayton Cycle Test-Loop," *Proceedings of Space Technology and Applications International Forum (STAIF-2005)*, edited by M. S. El-Genk, Vol. 746 of *AIP Conference Proceedings*, Melville, NY, February 2005, pp. 437–448.

[80] Mason, L. S., "A Power Conversion Concept for the Jupiter Icy Moons Orbiter," *Journal of Propulsion and Power*, Vol. 20, No. 5, September–October 2004, pp. 902–910.

[81] Barrett, M. J. and Reid, B. M., "System Mass Variation and Entropy Generation in 100-kWe Closed-Brayton-Cycle Space Power Systems," *Proceedings of Space Technology and Applications International Forum (STAIF-2004)*, edited by M. S. El-Genk, Vol. 699 of *AIP Conference Proceedings*, Melville, NY, February 2004, pp. 445–452.

[82] Johnson, P. K. and Mason, L. S., "Design and Off-Design Performance of 100 kWe-Class Brayton Power Conversion Systems," *Proceedings of Space Technology and Applications International Forum (STAIF-2005)*, edited by M. S. El-Genk, Vol. 746 of *AIP Conference Proceedings*, Melville, NY, February 2005, pp. 711–718.

[83] Lavelle, T. M., Khandelwal, S., and Owen, A. K., "Intermediate Fidelity Closed Brayton Cycle Power Conversion Model," Tech. Rep. TM-2006-213993, NASA Glenn Research Center, Cleveland, OH, 2006.

[84] Johnson, P. K. and Hervol, D. S., "Experimental Validation of a Closed Brayton Cycle System Transient Simulation," *Proceedings of Space Technology and*

Applications International Forum (STAIF-2006), edited by M. S. El-Genk, Vol. 813 of *AIP Conference Proceedings*, Melville, NY, February 2006, pp. 673–681.

[85] Johnson, P. K. and Mason, L. S., "Performance and Operational Characteristics for a Dual Brayton Space Power System with Common Gas Inventory," *4th International Energy Conversion Engineering Conference and Exhibit (IECEC)*, San Diego, CA, June 2006, AIAA-2006-4167.

[86] Wark, K., J. and Richards, D. E., *Thermodynamics*, WCB/McGraw-Hill, Boston, 6th ed., 1999.

[87] Zucrow, M. J., *Aircraft and Missile Propulsion*, Vol. II, John Wiley and Sons, New York, 1958.

[88] *NPSS User Guide, Release NPSS_1.6.3C*, 2005.

[89] Lytle, J. K., "High-Fidelity Full System Simulations," Tech. Rep. TM-2004-213309, NASA, October 2004.

[90] Binder, M., Tomsik, T., and Veres, J. P., "RL10A-3-3A Rocket Engine Modeling Project," Tech. Rep. TM-107318, NASA, 1997.

[91] Klann, J. L., *Closed Cycle Engine Program (CCEP) Operational Manual*, Cleveland, OH, 1991.

[92] Kays, W. M. and London, A. L., *Compact Heat Exchangers*, McGraw-Hill, New York, 3rd ed., 1984.

[93] Shapiro, A. H., *The Dynamics and Thermodynamics of Compressible Fluid Flow*, Vol. I, The Ronald Press Company, New York, 1953.

[94] Schnitzler, B., personal communication, NASA Glenn Research Center, Cleveland, OH, March 2007.

[95] Taylor, M. F., "Correlation of Friction Coefficients for Laminar and Turbulent Flow with Ratios of Surface to Bulk Temperature from 0.35 to 7.35," Tech. Rep. TR R-267, NASA Lewis Research Center, Cleveland, OH, September 1967.

[96] McCarthy, J. R. and Wolf, H., "Forced Convection Heat Transfer to Gaseous Hydrogen at High Heat Flux and High Pressure in a Smooth, Round, Electrically Heated Tube," *American Rocket Society Journal*, Vol. 30, 1960, pp. 423–425.

[97] Howe, S. D., Travis, B., and Zerkle, D. K., "Safe Testing of Nuclear Rockets," *Journal of Propulsion and Power*, Vol. 17, No. 3, May–June 2001, pp. 534–539.

[98] Culver, D. W., Koganov, V., and Rochow, R., "Low Thrust, Deep Throttling, US / CIS Integrated NTRE," *Proceedings of 11th Symposium on Space Nuclear Power and Propulsion*, edited by M. S. El-Genk, Vol. 301 of *AIP Conference Proceedings*, Melville, NY, February 1994, pp. ???–???